Constitutive and Fracture Characterization and Modelling of Monolithic and Tailor-Welded Blanks of Press-Hardening Steels

by

Pedram Samadian

A thesis

presented to the University of Waterloo

in fulfillment of the

thesis requirement for the degree of

Doctor of Philosophy

in

Mechanical and Mechatronics Engineering

Waterloo, Ontario, Canada, 2021

Examining Committee Membership

The following served on the Examining Committee for this thesis. The decision of the Examining Committee is by majority vote.

Supervisor	Michael J. Worswick, Ph.D. Professor, University of Waterloo
Co-Supervisor	Clifford Butcher, Ph.D. Assistant Professor, University of Waterloo
External Examiner	Yuanli Bai, Ph.D. Associate Professor, University of Central Florida
Internal Member	Elliot Biro, Ph.D. Assistant Professor, University of Waterloo
Internal Member	Etienne Martin, Ph.D. Assistant Professor, University of Waterloo
Internal-external Member	Dipanjan Basu, Ph.D. Associate Professor, University of Waterloo

Author's Declaration

This thesis consists of material all of which I authored or co-authored (see Statement of Contributions included in the thesis). This is a true copy of the thesis, including any required final revisions, as accepted by my examiners. I understand that my thesis may be made electronically available to the public.

Statement of Contributions

The following co-authors have contributed to the current work:

Professor Michael J. Worswick and Professor Clifford Butcher supervised this Ph.D. thesis. Mr. Lukas ten Kortenaar and Dr. Kaab Omer conducted the constitutive (flow) and fracture characterization of the 1.2-mm-thick Usibor® 1500-AS sheet in various as-quenched conditions. Mr. Cameron O'Keeffe and Prof. Butcher developed the user-defined material (UMAT) subroutine used to assign the material properties of different regions of tailor-welded blank (TWB) models in finite-element (FE) simulations. The balance of the research is my own work.

Abstract

This study investigates the constitutive (flow) and fracture response of two automotive-grade press-hardening steels, Usibor® 1500-AS and Ductibor® 500-AS, as well as their tailor-welded blanks (TWBs), for a range of as-quenched microstructures. Three different microstructures of each steel grade were developed through various quench-hardening heat treatments, comprising austenitization followed by air, die, oil, and/or water cooling. Mono- and multi-gauge laser-welded blanks of Usibor® 1500-AS and Ductibor® 500-AS, with three distinct combinations of 1.2-mm and 1.6-mm thicknesses, were also produced in the die-quenched condition.

For the as-quenched Usibor® 1500-AS and Ductibor® 500-AS monolithic blanks, characterization campaigns were conducted by means of mechanical tests, including shear, hole expansion, uniaxial tension, V-bend, and plane-strain and equibiaxial tension Nakazima domes. Both steel grades exhibited a high degree of sensitivity to cooling rate in terms of mechanical properties. For Usibor® 1500-AS, the fully-martensitic (oil-cooled) and fully-bainitic (air-cooled) microstructures had the highest strength and ductility, respectively, while the bainitic-martensitic (forced air-cooled) microstructure exhibited intermediate mechanical properties. For Ductibor® 500-AS, the mostly-martensitic (water-cooled) microstructure showed the highest strength and lowest ductility, followed by the intermediate ferritic-martensitic plus tempered martensite/bainite (die-cooled) and mostly-ferritic (air-cooled) microstructures, respectively.

The mechanical response of the as-quenched microstructures of Usibor® 1500-AS and Ductibor® 500-AS was modelled using a novel, coupled micromechanical-phenomenological strategy. In this approach, the constitutive behavior of the multi-phase steels was predicted using new mean-field homogenization (MFH) techniques, denoted the Samadian-Butcher-Worswick (SBW) formulations, with or without considering carbon-partitioning effects. The fracture response was estimated by tracking damage accumulation within each constituent phase using the phenomenological Generalized Incremental Stress-State-dependent damage MOdel (GISSMO) based on the micro-scale stress and strain states calculated by the MFH models. The proposed modelling strategy was shown to accurately predict the flow curves, fracture strains, and fracture *loci* of the bainitic-martensitic Usibor® 1500-AS and ferritic-martensitic Ductibor® 500-AS for the range of micro-constituent volume fractions considered.

The hot-stamped TWBs were subjected to tensile, equibiaxial tension Nakazima dome, and V-bend experiments with various weld orientations relative to the major principal stress direction. In the majority of the mechanical tests, fracture was initiated in one of the parent metals. Fracture initiation occurred in the Ductibor® 500-AS parent metal during the transverse tensile and equibiaxial tension Nakazima dome tests, whereas the Usibor® 1500-AS parent metal fractured in the longitudinal tensile and 45° and 90° V-bend tests. The only exception to the parent-metal failure was observed during the V-bend tests with the weld line lying on the punch-tip edge, for which fracture was initiated within the weld.

Finite-element models of the TWB experiments were developed within the LS-DYNA software using either the measured or predicted constitutive properties and fracture *loci* of the parent metals. A mapping scheme was created to assign the mechanical properties of each region of the TWBs to the corresponding elements based upon the measured local hardness. Two scenarios were examined for the TWB models: (i) including and (ii) excluding the detailed variation of mechanical properties within the weld region. The predictions revealed that the inclusion of the narrow weld region of the laser-welded blanks within the hardness-mapped TWB models resulted in an improvement of the predictions in terms of the load-displacement response and fracture locations, as compared to the "without weld" scenario.

A key outcome of this research was the quantification of the strong quench-rate sensitivity of the mechanical properties of Usibor® 1500-AS and Ductibor® 500-AS, which will affect their in-service (crash) performance after hot stamping. The developed modelling frameworks have direct application to predict the mechanical response of these steels and their TWBs subjected to hot-stamping processes in which quench rate: (i) is intentionally varied, such as within the tailored in-die heating technique; or (ii) naturally changes, for example, through fluctuations associated with the tooling temperature and contact pressure over time as well as transients during the startup and shutdown of production lines.

Acknowledgments

Twenty-six years ago in 1995, I officially started my academic education in an elementary school with the hope of becoming a doctor someday, and now in 2021, this long journey has reached its endpoint with lots of priceless experiences and lessons. It is now time to acknowledge those who accompanied and supported me during this adventure.

First of all, I am very thankful to God for all moments of my life. I have always felt him in the nick of time. The second will be my parents, Ali Samadian and Zahra Sanaei, who have been always with me in every step of this tortuous road and are the greatest supporters of mine. I owe everything in my life to them and will always do my best to make them pleased.

Next, I would like to express my gratitude towards my Ph.D. supervisor, Prof. Michael J. Worswick, who gave me the opportunity of working on such an interesting project in his research group. For me, aside from his exemplary genius, his charisma and leadership power, together with his restless, collaborative, and cheerful spirit have made him different from others. I have been very lucky for the opportunity of working with him and will be always honored for this collaboration in the future.

I would also like to appreciate my co-supervisor, Prof. Clifford Butcher, for all of his precious guides, support, and encouragement during my Ph.D. research. He never withheld his extraordinary knowledge and experience, and I learned numerous elusive experimental and numerical expertise in the areas of sheet metal forming and fracture as well as advanced computational methods from him. He is undoubtedly an excellent teacher and a smart researcher, and I am very glad for researching under his supervision.

Furthermore, I would also like to thank Prof. Mary A. Wells for giving me the chance of joining a Ph.D. program at the University of Waterloo. Although it was for a short period, I enjoyed working with her and will never forget her nice and welcoming attitude. Moreover, I would wish to express my sincere acknowledgment to Dr. Armin Abedini whose valuable advice and sympathy were always encouraging during the ups and downs of my Ph.D. research. I learned a lot from him.

The demanding experimental phase of this research would be impossible without the great help of research associates, research engineers, and technicians of our research group, especially Eckhard Budziarek, Andy Barber, Tom Gawel, Ryan George, Jose Imbert-Boyd, Amir Zhumagulov, and Jeff Wemp. I would be also thankful to all of the Engineering Student Machine Shop staff for their assistance with the experimental work.

I would also want to appreciate financial support from Honda R&D Americas, Promatek Research Centre (Cosma International), ArcelorMittal, Automotive Partnerships Canada, the Natural Sciences and Engineering Research Council, the Ontario Research Fund, the Ontario Centres of Excellence, the Ontario Advanced Manufacturing Consortium, and the Canada Research Chairs Secretariat during this research. Moreover, I would like to acknowledge Laurie Wilfong and Meghan Schmuck for their kind administrative support.

Last but not least, I would desire to express my special thanks to my sister, Parya Samadian, and my cousin and her son, Sahar Maftoon and Ryan Safdari, as well as every single friend of mine from the bottom of my heart for all of their support, company, laughs, and love during my Ph.D. life in the University of Waterloo: Armin Abedini, Taamjeed Rahmaan, Sante DiCecco, Kaab Omer, Nikky Pathak, Ping Zhou, Massimo Di Ciano, Zohreh Asaee, Farinaz Jeyranpourkhameneh, Farzad Sharifpour, Aram Bahmani, Alireza Mohammadizadeh, Negar Baghban, Chi-Hsiang Liao, Amir Zhumagulov, Cameron O'Keeffe, Jacqueline Noder, Kyu Bin Han, Samuel Kim, Cameron Jeffrey Tolton, Cale Peister, Matt Tummers, Suh Ho (Steven) Lee, Hossein Pishyar, Raphael Boulis, Abdelbaset Midawi, Hadi Razmpoosh, Adel Ghanbari, Mohammad Soltani, Hadi Hosseinzadeh Khaligh, Yahya Mahmoodkhani, Amir Hadadzadeh, Reza Esmaeilizadeh, Mehdi Ghazimoradi, Ali Zardoshtian, Reza Tangestani, Ali Khajezade, and Elham Naghavi.

I love you all and will never forget you.

Pedram Samadian

April 2021

TO MY PARENTS:

ALI SAMADIAN

&

ZAHRA SANAEI

Table of Contents

List of Figures

List of Tables

Chapter 1: Introduction

1.1. Background

Car manufacturers are actively pursuing different strategies to improve the fuel efficiency of automobiles while increasing vehicle safety in crash events [1–4]. One of the effective solutions to achieve these goals has been the incorporation of advanced high strength steels (AHSSs) into the vehicle architecture. Press-hardening steels are grades of AHSSs that normally possess low formability at ambient temperatures, and therefore, it is difficult to form them into complex shapes [5–8]. In 1974, the hot-stamping process was introduced to address this problem [1]. In this process, steel sheets are heated to austenitization temperatures and then simultaneously deformed and quenched within a die. This process benefits from the increased ductility of steels at elevated temperatures and leads to their significant strengthening due to the martensitic transformation they undergo during quenching [9–17].

However, hot-stamped parts usually exhibit relatively-low ductility in the as-quenched condition. For example, Usibor® 1500-AS is one of the most common automotive, hot-stamping steel grades with tensile strength of around 1500 MPa and elongation of less than 10% in the hot-stamped condition [18]. For this reason, the die-quenched Usibor® 1500-AS is often unsuitable for application in energy-absorbing components, which require high levels of deformation, and is normally used in structural applications that require high strength but only limited ductility, *e.g.* side-impact anti-intrusion components [4]. To resolve this issue, the tailored hot-stamping process has been introduced in which components with regionally-different properties are manufactured. Tailor-hot-stamped parts provide ultra-high strength in one region and high ductility in another region and correspondingly offer a high energy-absorption potential [19]. There are several methods for manufacturing hot-stamped parts with graded properties such as the partial austenitization or post tempering of blanks; use of hybrid dies with distinct thermal conductivity in different zones; partial heating of the die (in-die heating technique); and application of tailor-rolled blanks (TRBs) in hot stamping [16,20]. The hot stamping of tailor-welded blanks (TWBs) is a recently-developed tailored hot-stamping process in which sheets that differ in geometry, chemical composition, and/or coating are welded together to fabricate a component with different properties in various regions after hot stamping [21–26]. ArcelorMittal has produced new hot-

stamping steel grades of Ductibor® 500-AS and Ductibor® 1000-AS, which still have high ductility after die quenching, to join Usibor® 1500-AS in the forms of laser-welded blanks that can be hot-stamped for crash-safety applications. Such TWBs incorporate a high-strength region in the Usibor® 1500-AS side and a high-ductility (energy-absorbing) region in the Ductibor® 500-AS/1000-AS side and can be used in B-pillars and axial crush rails of vehicles to improve their fracture response in lateral, frontal, and rear impacts [27].

The goal of the current thesis is to characterize and model the constitutive (flow) and fracture behavior of the various microstructures of Ductibor® 500-AS and Usibor® 1500-AS as well as hot-stamped TWBs comprising combinations of these steels for use in crash-safety components. The outcomes of this research will contribute to a greater understanding of the in-service performance of these hot-stamping steels and their TWBs, thereby supporting vehicle weight reduction while enhancing vehicle safety.

1.2. Thesis Organization

The present thesis has been written in a manuscript-based format. The synopsis of this dissertation consists of a comprehensive review of the literature concerning the characterization and modelling of the mechanical behavior of advanced high-strength steels, followed by an outline of research objectives and scope, a summary of results, conclusions, and recommendations for future work. The rest of the thesis is comprised of five appendices, each of which incorporates either published or submitted peer-reviewed papers that detail the accomplished work and results of this research.

Chapter 2: Literature Review

2.1. Advanced High-Strength Steels (AHSSs)

In 1909, Henry Souther wrote an article, "American Automobile Steel", in the *New York Times* and stated that car manufacturers now know "to put the right steel in the right place" [28]. Souther's article originated from the fact that in those years, automakers had attached importance to the beauty and formability of their raw materials and adjusted the rigidity required for their products *via* producing thicker components. After that period, different factors such as safety, fuel efficiency, environmental emissions, weight reduction, manufacturability, durability, quality, and the cost of automobiles were also considered, and consequently, the need for materials with unique properties increased [29]. From the late twentieth century up to now, many steel grades have been employed in the creation of car structures, which compose around 60% of the weight of vehicles, to meet the distinct standards required for cars [29–31]. Figure 1 shows the different automotive steel types with their ultimate tensile strength (UTS), total elongation, and stress-strain curves [32]. In 1994, a group of 35 steelmakers started to develop a new class of automotive steels that can help with the fulfillment of fuel-efficiency and safety requirements [29,33]. In the early 2000s, they eventually introduced advanced high-strength steels (AHSSs). Compared to conventional steels, the chemical composition of AHSSs was designed so that their mechanical properties are enhanced after thermomechanical processing due to different final microstructures [34].

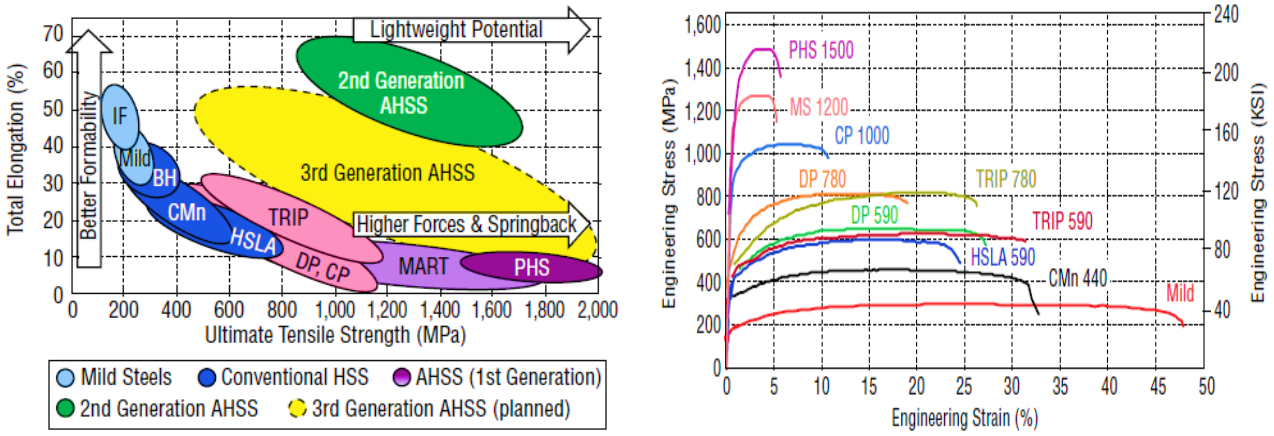

Figure 1: The mechanical behavior of different automotive steels [32].

Press-hardening steels, also known as hot-stamping and sometimes boron steels, are a group of AHSSs that contain lower amounts of carbon than martensitic steels and include a small amount

of elemental boron, which gives them high hardenability. The hot-stamping process, which will be discussed in detail in the next section, is typically used for the production of components from such steels. These steel grades generally acquire an extremely-high strength at the end of this process due to an austenite-to-martensite transformation and are typically used in parts of automobiles that require high intrusion-resistance and limited deformation, *e.g.* bumper reinforcements, door intrusion beams, A- and B-pillar reinforcements, and side-wall members. To improve the low ductility of press-hardened (or hot-stamped) steels, they can be post-tempered, but this occurs at the expense of their strength [29]. Other strategies exist to impart greater ductility to press-hardened steels, which will be described later.

2.2. Hot Stamping

In 1974, hot stamping was first developed by Norrbottens Järnverk AB (NJA), a Swedish steelmaker. NJA was later merged with Swedish Steel AB (SSAB) to fabricate tools with superior strength and wear resistance, such as stone-cutting disks, saw blades, lawnmowers, and shovels, using the hot-stamping process. In 1975, the Luleå University of Technology, NJA, and Volvo Truck started a common project to investigate the commercialization of hot stamping for the automotive industry. In 1984, the first hot-stamped component (an anti-intrusion door beam) was used in a car by Saab Automobile AB. Since then, the number of hot-stamped parts applied to vehicles has been dramatically increasing due to their impressive benefits in the weight reduction and crashworthiness of automobiles [9,20,35]. Figure 2 shows examples of hot-stamped components that have been used in a typical car [36,37].

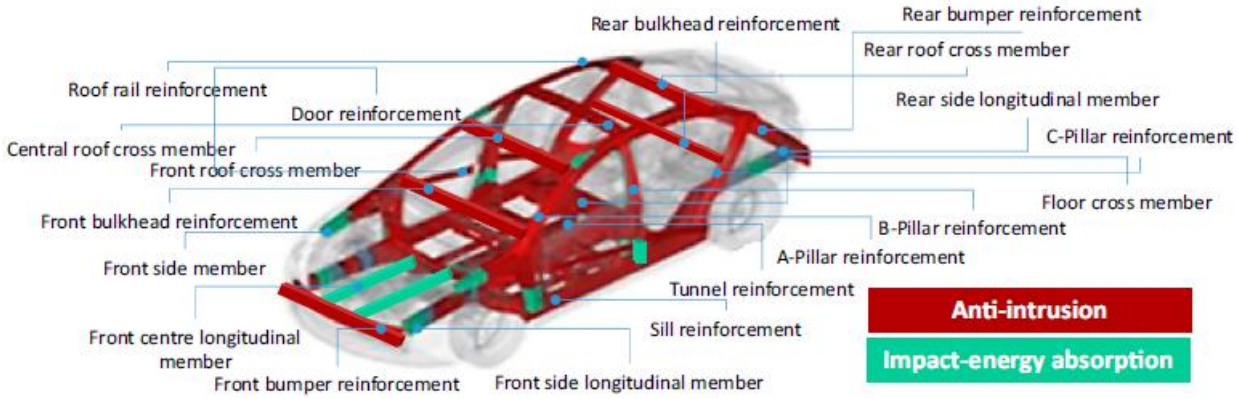

Figure 2: The hot-stamped components present in a typical car [36,37].

The conventional hot-stamping process can be performed in direct and indirect methods (Figure 3) [9]. In direct hot stamping, steel sheets with low ductility at room temperature are first austenitized and then simultaneously deformed and quenched in a cooled die. In indirect hot stamping, the steel blanks are initially cold-stamped up to 90%-95% of their final shape and subsequently hot-stamped to achieve the final shape and properties. The indirect method allows a higher extent of deformation for making complex-shaped components and decreases the die wear caused by uncoated steel sheets [5], [8], [8], [42].

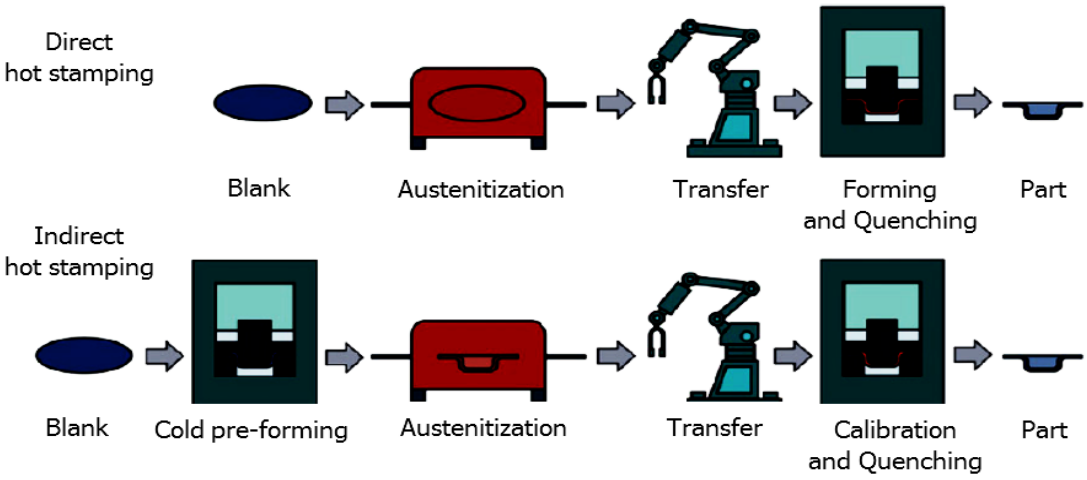

Figure 3: The schematics of the direct and indirect hot stamping [9].

The martensitic microstructure that results from the die quenching of steels in the hot-stamping process imparts a very high level of strength (850 MPa-2000 MPa) such that they can be categorized as ultra-high-strength steels (UHSSs). This strength range allows automakers to enhance the required robustness of their products with thinner parts, which results in both mass and cost reductions while improving the overall integrity and safety of car structures [5], [8], [28], [32], [42], [45]. However, one of the essential limitations of this process is that hot-stamped components, despite their high intrusion resistance, exhibit relatively-low energy-absorption capacity due to their limited ductility [8,20].

2.3. Tailored Hot Stamping

The fabrication of hot-stamped components with graded properties is achieved by a range of innovative hot-stamping processes, collectively termed “tailored hot stamping”. These tailoring processes include:

i. *Partial austenitization of blanks:* With this method, blanks are heated in a furnace with thermally-distinct zones and austenitized in different sections at various levels based on the temperature of each zone. Stoehr *et al.* [39] and Wilsius *et al.* [40] studied the changes in the mechanical properties of boron steels during this process and showed that the regions heated to lower temperatures exhibit superior ductility with lower strength and hardness;

ii. *Partial post tempering of hot-stamped parts:* With this method, parts are locally tempered after hot stamping at prescribed temperatures for a specific time to generate tempered martensite, which has more ductility than martensite. Studies on this process have shown that as the tempering temperature increases, there is a higher decrease in the hardness of hot-stamped components [41];

iii. *Regionally-different cooling of heated blanks:* With this method, the different regions of austenitized blanks are cooled with distinct cooling rates through the use of:

   a. Partially-heated dies (in-die heating technique) [42,43]; George [7] produced a tailor-hot-stamped lab-scale B-pillar using a die at various temperatures in different regions and showed that the hardness decreases from the section in contact with the cold die to that in contact with the heated die. Omer [15] studied the crash response of several tailor-hot-stamped axial crush rails and showed that the local soft regions result in a more stable crush response with almost no cracking;

   b. Hybrid dies with different thermal conductivity in different regions [44];

   c. Dies with various surface conditions [45,46]; or

   d. Locally-disparate die pressures [47]; Studies show that the die regions with lower thermal conductivity result in a lower cooling rate of the heated blanks and lower resultant hardness values, and higher die pressures, which lead to higher heat transfer between the heated workpiece and room-temperature die, create parts with superior strength [46,47];

iv. *Hot stamping of tailor-rolled blanks (TRBs):* With this method, blanks with regionally-different thicknesses, produced by a tailored rolling process, are hot-stamped and finally,

due to experiencing distinct cooling rates in various regions, form components with high intrusion-resistance and energy-absorption capacity in disparate zones. Since 2006, hot-stamped TRBs have been used for the fabrication of various automobile parts, such as B-pillars and rear bumpers [16,20,48]; and

v. *Hot stamping of tailor-welded blanks (TWBs):* With this method, blanks with different thicknesses, chemical compositions, and/or surface coatings are welded together and then hot-stamped. The use of TWBs contributes to reducing the weight of vehicles and assembly requirements due to the avoidance of strengthening patches, *e.g.* patchwork blanks made by welding small patches on the main blank with the aim of local strengthening. However, the main benefit of TWBs is related to their role in improving the crash performance of vehicles [16,20,26]. TWBs are generally comprised of hardenable and non-hardenable (or less-hardenable) steel sheets that achieve high-strength and -ductility regions after hot stamping, respectively. Therefore, the resultant hot-stamped components can be used in structural members that require such a variety of mechanical properties, *e.g.* B-pillars and axial crush rails [16,20].

Usibor® 1500-AS and Ductibor® 500-AS are two steels that are currently welded together to produce TWB components with tailored properties after hot stamping. In such hot-stamped TWBs, the tensile strength and elongation of the Usibor® 1500-AS region normally become around 1500 MPa and 6%, whilst those of the Ductibor® 500-AS region reach about 550 MPa and 20%, respectively. Hence, the hot-stamped Ductibor® 500-AS has superior toughness but lower strength, and the hot-stamped Usibor® 1500-AS has higher strength but lower toughness [18,27]. Such a discrepancy in mechanical properties is correlated to the different resultant microstructures of these steels after the hot-stamping process. The microstructure of the hot-stamped Usibor® 1500-AS is fully martensitic, while that of the hot-stamped Ductibor® 500-AS is ferritic-martensitic [49]. However, dependent on the hot-stamping conditions, the final microstructure, volume fractions of the constituent phases, and the resulting mechanical properties vary. Naderi [13] investigated the mechanical behavior of Usibor® 1500-AS after different die-quenching conditions. Hagenah *et al.* [50] studied the effects of deformation and quenching speed during the hot-stamping process of this steel using the Gleeble thermomechanical machine. Bardelcik *et al.* [2] examined the strain rate sensitivity of the different microstructures of Usibor® 1500-AS. Eller *et al.* [51], ten Kortenaar

et al. [52], and Golling *et al.* [53,54] characterized the fracture limits of the tailored Usibor® 1500-AS in several stress states. Omer *et al.* [42] modelled the dynamic axial crush testing of tailor-hot-stamped axial rails *via* mapping the interpolated flow curves and fracture *loci* of the several microstructures of Usibor® 1500-AS in terms of hardness. However, contrary to Usibor® 1500-AS, there have been relatively-few studies conducted on the mechanical response of Ductibor® 500-AS in different material conditions and the hot-stamped TWBs of these two steels. Mishra [55] investigated the effects of the austenitization time and temperature as well as strain rate on the strength and ductility of the hot-stamped Ductibor® 500-AS. Múnera *et al.* [56] characterized the quasi-static and dynamic properties of the hot-stamped TWBs of Usibor® 1500-AS and Ductibor® 500-AS. Kang and Kim [24] examined the effects of the Al-Si coating on the microstructures and mechanical properties of the hot-stamped TWBs of Ductibor® 500-AS and Usibor® 1500-AS at low-to-high strain rates. Peister *et al.* [57,58] studied the crash performance of axial crush rails from these TWBs in dynamic sled testing. No comprehensive work to-date has studied the flow and fracture response of Ductibor® 500-AS and the hot-stamped TWBs of this steel and Usibor® 1500-AS as a function of microstructure. This is a considerable gap in the literature given the important crash-safety applications of these materials.

2.4. Fabrication of Tailor-Welded Blanks (TWBs): Laser Welding

Laser welding is one of the common joining processes used for producing TWBs since it creates thin weld seams and small heat-affected zones (HAZs). Additionally, it normally uses a butt joint without any material overlap, resulting in lower material usage and lighter components [26,59]. One challenge with the conventional laser welding of hot-stamping steels like Ductibor® 500-AS and Usibor® 1500-AS is their Al/Si coating, which serves to prevent decarburization and oxidization during the austenitization step of the hot-stamping process. This coating leads to the creation of intermetallics of Al and Fe after welding, which promote ferrite formation in the weld zone after hot stamping, to the detriment of strength and crash performance [24]. To solve this problem, the laser-ablation method has been developed, in which the coating is locally removed from joined sections of the base metals prior to welding [60].

2.5. Deformation Behavior of Tailor-Welded Blanks (TWBs)

The mechanical properties of TWBs are usually investigated by uniaxial tensile tests. For this purpose, different sample geometries are used depending on whether the focus is on the weldment (weld and parent metals together) or just the weld zone. For the weldment, the samples need to be large enough to include the base metals and weld zone in the gauge area, and the weld line can have different angles with respect to the loading direction. For the weld zone, only longitudinally-oriented samples can be tested in either of two following approaches. One is to use sub-sized or mini samples so that the gauge area is comprised of only the weld zone of TWBs [59], [61]. The other approach is to use large standard specimens and then calculate the flow curve of the weld zone by means of the rule of mixtures, given the stress-strain curves of the base metals and uniform distribution of axial strain across the samples [59]. Different numerical methods were also conducted to obtain the flow curves of different regions of the weld zone. Reis *et al.* [62] estimated the flow curves of various areas of the weld zone of laser-welded FeP06 steel by considering the direct proportionality of the flow-stress ratio and hardness ratio of the base metal and weld zone. Cheng *et al.* [61] calculated the hardening behavior of HAZs within laser-welded blanks of AISI 304 stainless steel by averaging that of the base metal and fusion zone. Ramazani *et al.* [63] characterized the flow curves of the HAZ and fusion zone of TWBs of gas-metal-arc-welded DP600 steel *via* multi-scale computational homogenization modelling.

Relying on the material type, the strength of TWBs can be lower than, equal to, or higher than that of the base metals. Panda *et al.* [21], Chan *et al.* [64], and Miles *et al.* [65] reported higher, similar, and lower strength levels for TWBs of IF steel, SPCC steel, and 6022-T4 aluminum alloy, respectively, as compared to the strength of their base metals. TWBs generally have lower ductility than their base metals regardless of the material type, welding method, weld-line orientation, and thickness ratio [21,59,65–67]. The strength, formability, and ductility of TWBs are dependent on the weld-line orientation. Kim *et al.* [68] and Panda *et al.* [21] showed that longitudinally-welded TWBs have higher strength than transversely-welded TWBs in the case of SPC1 and IF steel alloys. Cheng *et al.* [66] reported higher formability and ductility for transversely-welded TWBs in comparison with longitudinally-welded TWBs of 5754-O aluminum alloy. Buste *et al.* [69] examined multi-gauge aluminum laser-welded blanks in limiting dome height (LDH) tests and reported that for transverse and 45° weld orientations, fracture is initiated

in the thinner parent metal, while for longitudinal welds, fracture initiation occurs in the weld. The thickness ratio of the base metals affects the formability and ductility of their TWBs. Studies by Chan *et al.* [25,64] and Friedman and Kridli *et al.* [67] on steel and aluminum alloys revealed that as the thickness ratio approaches unity, formability and ductility are promoted. As discussed by Shakeri *et al.* [70], Meinders *et al.* [71], and Abbasi *et al.* [72], fracture in TWBs is initiated in either the least ductile (usually the weld [66]) or weakest (either of the HAZ [73] or base metal [74]) regions if force is applied along or across the weld seam, respectively.

Most of the numerical studies in the literature dealing with the failure of TWBs mainly focus on the instant of strain localization during the forming processes. These studies generally predict localized necking (formability) in as-welded blanks of cold-stamped or heat-treated alloys by either employing various formability theories [75–77] or implementing empirically- or semi-empirically-determined FLDs in finite-element method software [78–83]. However, for crash-safety applications, fracture initiation is of main concern in TWB components, which are mostly in the hot-stamped condition with all regions homogenized during the austenitization stage of the hot-stamping process. There are a few studies in the literature on the modelling of fracture in such TWBs. These studies mostly use the fracture response of the parent metals and neglect the weld region within TWB models [84–86]. Therefore, the literature lacks numerical investigations into the fracture response of TWBs that take the weld region into account.

2.6. Numerical Modelling of Deformation Behavior

As discussed in the previous sections, the use of press-hardening steels and their TWBs within car bodies is currently one of the effective solutions for the automotive industry to improve the crashworthiness of automobiles while reducing their weight. To support the design of automotive structures from these steels, crash-safety simulations can be helpful in minimizing the need for time-consuming and expensive experiments [34]. Since the plasticity and fracture models of hot-stamped monolithic and tailor-welded blanks are vital ingredients of such numerical simulations, the solid knowledge of the modelling concepts of these phenomena is necessary to accurately predict the crash performance of vehicle structures. For this purpose, first, the plasticity and fracture of the materials should be characterized under various loading conditions, such as simple shear, pure tension, drawing, and stretching, using coupon-level tests, *e.g.* shear, uniaxial

tension, and Nakazima dome experiments. Next, numerical models based on the empirical results should be validated *via* finite-element (FE) simulations of such tests. After that, the predictive ability of the developed FE models should be evaluated by conducting various component-level tests, *e.g.* three-point bending and axial crush testing. Finally, the crash behavior of components in a car body should be verified by simulating a crash test of a full vehicle [8,16,87–89]. As this research deals with the first two steps of crashworthiness simulations (*i.e.* material characterization and modelling), different approaches to the plasticity and fracture modelling of materials based on the experimental data are reviewed next.

2.6.1. Plasticity Modelling

To theorize the plastic behavior of materials, a proper yield function is first used to determine the boundary of elastic and plastic responses under different loading conditions. Yield functions can be categorized as either physically-based or phenomenological models. Physical models presume that the plastic deformation of materials is initiated once a physical variable reaches its threshold. In contrast, phenomenological yielding models are formulated to approximate the results of either experiments or physics-based models [90]. For example, the von Mises criterion [91] is a physical model for isotropic materials since it assumes that material yielding starts when the elastic distortion energy or shear stress on the octahedral plane attains its threshold. However, the non-quadratic model proposed by Barlat *et al.* in 2003 [92], which is a plane-stress yield function for anisotropic materials, is phenomenological since it has anisotropy parameters that need to be calibrated by the experimental data. The second step in the modelling of the plastic deformation of materials is to determine how the subsequent yield surface changes due to hardening/softening. The yield surfaces of sheet metals tend to expand (isotropic hardening), translate (kinematic hardening), or distort (distortional hardening) and sometimes experience a combination of these effects. The next step is to formulate the constitutive equation between stress and strain, either incrementally or in a rate form (due to the path-dependent essence of plastic deformation), by using flow rules. The last step is to define a loading-unloading criterion to show the differences between plastic loading, elastic loading, and elastic unloading [90].

2.6.1.1. Micromechanics-Based Modelling: Mean-Field Homogenization

Micromechanics is referred to as the study of the mechanical behavior of heterogeneous materials on the scale of their constituent phases. Micromechanical models are widely-used multi-scale schemes which can cover length scales down to the order of 1 μm. In most micromechanical models, the variations of stress and strain fields at a larger scale are affected by the volume average of those at a smaller scale. Moreover, since the stress and strain fields and compositions tend to locally change at the microscale, contrary to those at a macroscale, the microscopic stress and strain fields can be calculated in terms of uniform applied or far-field (macroscopic) stress and strain. One of the main applications of micromechanical models is in the constitutive modelling of the elastoplastic deformation behavior of heterogeneous materials based on the mechanical response, geometry, and phase arrangement (matrix-inclusion, interpenetrating, and granular) of their individual phases. For this purpose, it is crucial to select a material scale of proper length such that it can be a good indicator of the properties of the whole material [93]. The scale needs to be large enough to contain all of the microstructural features of the whole material so that the calculated average properties (effective properties) and fields approximate the real material properties and fields. On the other hand, the scale must be small enough to be able to neglect the macroscopic gradients of stress, strain, and compositions from the analysis viewpoint. The volume element of a multi-phase material that has these characteristics is called the representative volume element (RVE).

One of the micromechanics-based modelling methods is mean-field homogenization (MFH) in which the mechanical properties and response of composite materials are determined by the statistical averaging of those of the existing phases in the RVE, given the interactions of individual phases in terms of uniform micro stress and strain fields. The averaged properties obtained by this method are called effective or homogenized properties [34,93,94]. In MFH schemes, a composite material corresponds to a so-called comparison or equilibrium homogenized material (EHM) with the same boundary condition but uniform properties that includes a constant equivalent eigenstrain/stress representing the misfits from embedding inclusions in the matrix (Figure 4). Eigenstrain/stress fields are created without applying external force/displacement and can be obtained by equating the micro strain/stress fields of the constituents in the real and comparison materials in terms of their elastic/compliance tensors and the Eshelby tensor. The Eshelby tensor

relates the disturbed strain field, which is derived from embedding the inclusion in the matrix, to the eigenstrain and is a function of Poisson's ratio of the EHM and the aspect ratio of inclusions. Assuming different properties for the EHM and relationships between the micro strain fields of the inclusions and matrix, various MFH models have been developed so far, the most well-known ones of which will be introduced in the following. Since the present work will aim to take advantage of MFH schemes to predict stress/strain partitioning between constituent phases of two-phase steels, envisaged as composites with adopted matrix-inclusion phase arrangements, under deformation, all of the formulations of MFH models will be presented for two-phase composites.

MFH models are generally applied in displacement boundary conditions and denote the strain partitioning between the existing phases in RVEs by the use of strain concentration tensors (A). Strain concentration or influence tensors linearly relate the average micro strain fields ($\langle\varepsilon\rangle^{(phase)}$) to the applied far-field strain ($\langle\varepsilon\rangle$) [95–97].

$$\langle\varepsilon\rangle^{(phase)} = \mathrm{A}^{(phase)} : \langle\varepsilon\rangle \tag{1}$$

Voigt [98] and Reuss [99] developed the first MFH models by assuming that either the strain or stress applied to a composite material is uniformly distributed within the material, respectively. These models are very simple and violate either local compatibility or equilibrium in the heterogeneous material. In addition, they do not consider the interaction of phases and the shape, orientation, and distribution of inclusions. In 1957, Eshelby [100] derived the first closed-form solution for satisfying compatibility and equilibrium conditions *via* introducing the concept of equivalent homogenous materials (EHMs), comprising ellipsoidal inclusions dispersed in an infinite homogeneous matrix (Figure 4).

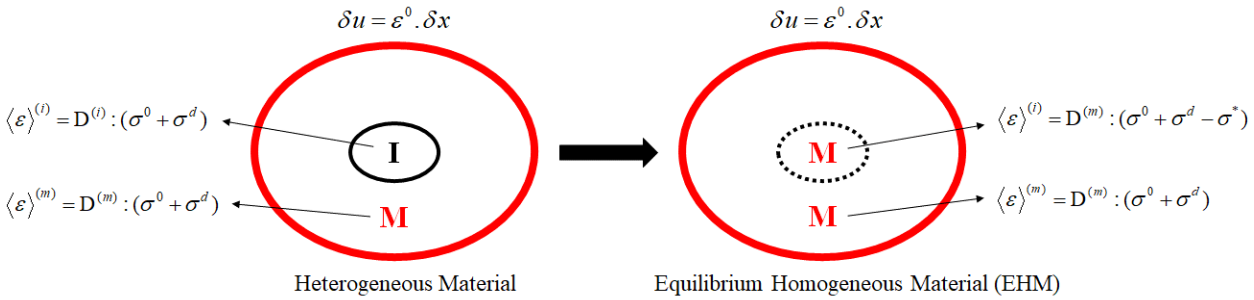

Figure 4: Eshelby's solution; M and I stand for the matrix and inclusion, respectively [101].

To account for the self-interactions of inclusions at higher volume fractions, the self-consistent (SC) [102,103] and Mori and Tanaka (MT) [104] models were proposed. Hori and Nemat-Naser [105] defined particular microstructures for the SC and MT models by proposing a *double inclusion* microstructural model. This microstructure comprises two concentric, co-axial ellipsoidal domains with the same aspect ratios embedded in an infinite homogenous material with the elastic properties of the whole composite. They further generalized it by considering multi-layers around the inner ellipsoid (the *multi-inclusion* model [105]). To improve MFH models in terms of the consideration of varying shape, orientations, and the distribution of inclusions in a matrix, Ponte Castaneda and Willis (PCW) [106] proposed a fourth-order tensor (S^d) to define the distribution of inclusions. To address the issues associated with the intermediate volume fractions of inclusions, interpolative models were suggested. Lielens *et al.* [107] proposed an interpolative model based on the definitions of the Mori-Tanaka (MT) and inverse Mori-Tanaka (IMT) models. Perdahcıoglu and Geijselaers [108] proposed another interpolative model with the lower and upper bounds of the Reuss and Voigt models, respectively.

MFH models were originally developed for linear elastic materials and can be expanded to plastic deformation using linearization techniques [109,110]. First-order secant-based [111] and tangent-based approaches [112] are the most commonly-used linearization methods. The former approach, in which total stress and strain are correlated *via* the secant modulus [113], is only valid for proportionally-monotonic loading conditions [93]. However, the latter approach, in which stress and strain are incrementally related using the tangent modulus [114], is applicable to general loading conditions [115]. Wu *et al.* [116] proposed incremental secant-based linearization methods that can be used in general loading states. Ponte Castaneda [117] and Bornert *et al.* [118] proposed the so-called Spectral-Decomposition and General-Isotropization (SDI and GI) methods, respectively, to deal with the anisotropy of tangent moduli. Anisotropic tangent moduli normally result in more expensive computations and overly-stiff estimations of the composite stress response [119]. The SDI method might not have acceptable predictions for non-proportional loading [119], though it has good predictions in uniaxial tension and cyclic loading [115]. However, the GI method is applicable to general loading conditions. Suquet [120], Ponte Castaneda [117], Doghri *et al.* [121], and Wu *et al.* [109] developed the second-order linearization

methods by applying the “second statistical moments” of micro stress and strain fields to obtain less stiff predictions.

Different studies show that the accuracy of the predictions through the aforementioned MFH models and linearization schemes varies depending on the material and loading conditions [109,115,119]. For example, Kluseman *et al.* [122] applied the MFH technique to a matrix with spherical voids (zero elastic properties) and obtained better estimations for Young’s modulus using the Voigt model compared to the more advanced SC, MT, and Lielens models. They also reported the superior performance of the SC model in predicting Young’s modulus of a particulate composite compared to the MT model. However, Hessman *et al.* [123] showed the higher accuracy of the MT model for predicting Young’s modulus of a fibrous composite compared to the SC model. Doghri *et al.* [124] showed the comparable predictions of the MT model using the first- and second-order tangent-based linearization approaches for the flow curve of a ferritic-martensitic steel in a direct-loading condition with respect to FE results. However, both frameworks were not able to accurately estimate the flow response in the reverse-loading condition. Golling *et al.* [53] reported the underestimation or overestimation of the hardening behavior of the different microstructures of 22MnB5 steel using the Lielens model through the first-order tangent-based linearization approach. In a study on the flow curve of a ferritic-austenitic steel, Wu *et al.* [109] found that the second-order approaches do not necessarily yield appropriate predictions with respect to the first-order schemes. Furthermore, Doghri *et al.* [124] showed that for composites with a large difference between the stiffness of the constituents, inclusion aspect ratios of higher than one, and a low hardening rate for the matrix, the secant-order formulation provides much better predictions. However, for other conditions, the discrepancy in the performance of the first- and second-order linearization approaches is not significant.

2.6.1.2. Microstructure-Based Modelling of Multi-Phase Steels

The hardening behavior of multi-phase steels depends on the characteristics of their constituent phases such as the volume fraction, morphology, distribution, grain size, chemical composition, and dislocation density. These parameters are usually interconnected, and the determination of their individual roles in macro and micromechanical response needs careful examination [125,126]. The microstructure-based modelling of the constitutive response of mixed-

phase steels is usually conducted through FE micromechanical modelling or MFH techniques using the hardening response of their constituent phases [93,95]. Such modelling approaches are inherently able to take the effects of the geometrical features of micro-constituents, *e.g.* shape, size, quantity, and/or distribution, into account. However, the influences of other features like the chemistry and dislocation population of constituent phases must be accounted for within the constitutive models of the micro-constituents in these numerical solution schemes. For this purpose, there is first a need for the understanding of the roles of these parameters in material hardening.

Plastic deformation in materials is generally accompanied by the motion of dislocations on slip planes. The movement of dislocations is normally hindered by the arrangements of atoms within the crystal lattice (Peierls effect or lattice friction) as well as alloying elements in the solid solution, which results in the hardening of materials during the plastic deformation. The self-interactions of dislocations can also lead to material hardening. Dislocations generally pile up at obstacles such as dislocation entanglements (dislocation forests) and impurities on active slip planes and, as a result, back stresses are created that act in a direction opposite to the loading direction. Therefore, dislocations require higher stresses along slip directions to overcome such barriers and restart slip. If the loading direction is reversed, the existing back stresses, together with the decrease in the traffic of dislocations due to the annihilation of some primary dislocations by newly-formed opposite-sign dislocations, assist the slip of the entangled dislocations in the opposite direction. Thus, the material exhibits a softer response in the reverse direction (Bauschinger's effect) [127].

For steels, particulary those with ferritic-martensitic microstructures, carbon partitioning and geometrically-necessary dislocations (GNDs) play important roles in the hardening response of the micro-constituents. In ferritic-martensitic steels, due to the limitation of carbon solubility within ferrite, the carbon concentration of martensite significantly varies with its volume fraction. Studies by Ramazani *et al.*[128], Pierman *et al.* [129], and Ebrahimian and Banadkouki [126] show that the higher the martensite volume fraction, the lower the martensite carbon content and strength. The strength of ferrite is mostly affected by geometrically-necessary dislocations (GNDs). GNDs are dislocations produced at the interfaces of different phases to preserve the continuity of the crystal structure due to volume changes accompanied by variations in crystal

structures during microstructural transformations (especially austenite to martensite) [126]. GNDs contribute to both isotropic and kinematic hardening *via* the intersection of dislocation forests and creating substantial back stresses at phase boundaries, respectively [125,130,131]. Ebrahimian and Banadkouki [126] reported that as the martensite volume fraction increases, ferrite is strengthened due to the higher transformation-induced shape deformation (higher GNDs and resultant back stresses) within the ferritic grains around ferrite-martensite interfaces.

Rodriguez and Gutierrez [132] developed a dislocation-based hardening law for the constituent phases of steels based on the classical relation between flow stress and the density of dislocations. This model considers the effects of the lattice friction and alloying elements, carbon partitioning between phases, and dislocation generation and annihilation during plastic deformation. Ramazani *et al.* [63,128,133,134], and Srithananan *et al.* [135] utilized this hardening law to calculate the hardening behavior of the micro-constituents of dual-phase (DP) and Usibor® 1500-AS steels, respectively. Sodjit and Uthaisangsuk [130,131] applied the net polarized stress resulting from the GND back stresses, modelled by Delince´ *et al.* [136], with Rodriguez and Gutierrez's hardening law to estimate the hardening behavior of ferrite in ferritic-martensitic DP steels.

2.6.2. Fracture Modelling

Metals generally fracture in either a brittle or ductile manner. As this research concerns the fracture characterization of relatively-ductile steels [27], this section will mainly deal with ductile fracture. From a macroscopic viewpoint, ductile metals experience a large amount of plastic deformation before fracture in contrast to brittle materials [137]. From a microscopic perspective, ductile fracture is referred to as the type of fracture that occurs through void nucleation, growth, and coalescence. Based on these two aspects, the modelling of ductile fracture can be categorized into two main groups: physical and phenomenological approaches. The former approach follows the microstructural phenomena that happen in metals and lead to fracture. Micromechanical damage models fall into this category. However, in the latter approach, the general behavior of metals before rupture is examined. Continuum damage mechanics (CDM) and conventional continuum mechanics (CCM) models are two of the well-known approaches for the phenomenological prediction of the ductile fracture [34,87].

2.6.2.1. Micromechanical Damage Models

The microstructures of metallic alloys commonly contain particles as impurities or secondary phases, which are preferred locations for stress localization during plastic deformation. High stresses at such sites result in particle debonding from the matrix or local rupture, and both can lead to the formation of microvoids. This event corresponds to the first step of the ductile fracture process, known as void nucleation. Most engineering alloys already have some level of pre-existing voids, which are generated during manufacturing processes. As deformation progresses, the voids start growing (the second step of the ductile fracture) until neighboring voids are linked up, known as void coalescence (the third step of the ductile fracture), and macro cracks are formed. Finally, the material fractures. Since the empirical investigation of the individual stages of the ductile fracture is complicated, expensive, and time-consuming, there exists a need for constitutive models for the prediction of this type of fracture. Micromechanical damage models consider an appropriate RVE of the microstructure of a material and predict void evolution through nucleation, growth, and coalescence.

The modelling of void nucleation is a complex task because it necessitates the modelling of interfaces, and it is difficult experimentally to measure their properties [138]. Such models are typically based on the fact that void nucleation occurs when the strain energy in the particle exceeds either the interface energy of particles and matrix or the surface energy of a crack that is formed because of the particle fracture [139–142]. Void nucleation mechanisms are described as either stress-controlled or strain-controlled, based on the overall particle size. In stress-controlled models, the void volume-fraction growth rate ($\dot{f}$) is obtained in terms of the equivalent stress rate ($\dot{f}_{nucleation} = M_1 \dot{\bar{\sigma}}$), while in strain-controlled models, the rate is achieved in terms of equivalent plastic strain rate ($\dot{f}_{nucleation} = F \dot{\bar{\varepsilon}}^{p}$) [142]. Argon *et al.* [140,143,144] and Brown and Stobbs [145] defined critical interface stresses for void nucleation in terms of flow and hydrostatic stresses as well as dislocation density, respectively. Beremin [146] proposed a stress-based nucleation model using a homogenization method for calculating partitioned stresses into inclusions. Needleman [147] modified Argon's model to consider the partitioning hydrostatic stress at matrix-particle interfaces. Among strain-based nucleation models, the model developed by Chu and Needleman [142] in terms of equivalent plastic strain and instantaneous volume fraction of nucleated voids is

most commonly used. To model void growth, it is assumed that the material is comprised of several ellipsoidal or spheroidal voids that are each located in a cubic or hexagonal cell. Void growth is analyzed in one of the cells by the use of existing models that consider the effects of stress triaxiality (hydrostatic stress state) and plastic strain [148,149]. McClintock [148] defined void growth as a function of macroscopic strain. Rice and Tracy [150] showed the exponential dependency of void growth on stress triaxiality. Huang [151] modified Rice and Tracy's model to improve estimations for void growth at low stress triaxialities. Liu *et al.* [152] added the void size effect on void growth within the Rice and Tracy model using a dislocation model. Ragab [149] developed a void-growth model considering the effects of void shape and stress states. In the modelling of void coalescence, it is typically assumed that a geometrical parameter, *e.g.* the void radius and spacing, reaches its critical value [138] as void coalescence starts. Tvergaard and Needleman [153] introduced a critical porosity for the onset of void coalescence. Thomason [154] proposed a plastic-limit load model in which void coalescence is defined as homogenous and localized deformation modes become equivalent. Zhang *et al.* [155] and Ragab [149] extended Thomason' model to take the effects of the work-hardening exponent and strain hardening of void ligaments into account, respectively.

Micromechanical damage models mainly couple pressure-dependent yield functions that consider the void effect on strength of materials with void-evolution models. The Gurson model [141] was the first yield criterion proposed for porous ductile materials with spherical or cylindrical voids. Tvergaard [156] modified this model to achieve more compatible results with those of numerical simulations. To consider the coalescence effect, Tvergaard and Needleman modified the Gurson-Tvergaard (GT) model and proposed the so-called Gurson-Tvergaard-Needleman (GTN) model [153]. To consider the evolution of the void shape, Ragab [149] defined the calibration parameters of the GT model as functions of stress triaxiality, the work-hardening exponent, and the instantaneous void shape. The Gologanu-Leblond-Devaux (GLD) model [157] is another Gurson-based model that includes the void-shape evolution. Studies show that Gurson-based models do not have a suitable performance under prominently-shearing loading conditions since they predict pronounced void growth in such stress states in contrast to reality [158]. Gurson-based models generally consider the occurrence of fracture when the void volume fraction reaches its critical value [159]. The major deficiency of micromechanical damage models lies in a large

number of material parameters that need to be calibrated by experiments. This requirement has noticeably limited the industrial applications of such models [160].

2.6.2.2. Continuum Damage Mechanics (CDM) Models

The emergence of the concept of continuum damage mechanics (CDM) models dates back to 1958 when Kachanov defined an "equivalent stress" for damaged materials [161]. CDM models are less complicated than micromechanical damage models since they do not deal with the microstructural details of void evolution and, instead, examine material degradation *via* an internal damage variable (D). The damage variable in any plane of an RVE is defined as the ratio of the damage surface area to the total surface area of the plane. As D reaches its critical value (obtained by calibration), material fracture is predicted to occur.

Based on thermodynamical constitutive equations, it was shown that damage evolution can be related to a damage dissipation potential *via* an expression that is similar to one obtained by von Mises in 1926 for relating plastic strain rate to a plastic potential function. CDM models usually differ from each other in terms of the adopted definitions for the damage dissipation potential and, as a result, create distinct expressions for the damage variable [162], [163]. These models are normally coupled with plasticity constitutive models. Lemaitre [164], Wang [165], Bonora [166], and Dhar *et al.* [167] proposed various relationships for the rate of the changes in the damage variable that can be applied to discrete plasticity models to capture the material softening that stems from progressive damage. However, such an approach makes the calibration of the material parameters for the plasticity and damage models difficult. Although often requiring a smaller number of material parameters, CDM models are fundamentally weak in the prediction of fracture initiation, as compared to micromechanical damage models.

2.6.2.3. Conventional Continuum Mechanics (CCM) Models

Conventional continuum mechanics (CCM) models, like CDM models, consider the macroscopic response of materials and include the global effects of existing phases and defects. The difference comes from the fact that damage indicators (if applicable) in such models are not usually coupled with the plasticity model of materials. As a result, these models are easier to use, and industry is more interested in deploying them [87]. Fracture initiation in these models is

usually defined to occur when a damage parameter reaches its threshold. The evolution of damage is generally modelled by integrating a weighting function in terms of stress-state variables over the history of equivalent plastic strain ($\bar{\varepsilon}^p$) [34]:

$$D = \int_{\bar{\varepsilon}^p} f(\sigma_{ij}) d\bar{\varepsilon}^p \tag{2}$$

Up to now, several weighting functions ($f(\sigma_{ij})$) have been proposed. Cockcroft and Latham [168] and Oh *et al.* [169] presented weighting functions that are based on assumptions regarding the effect of maximum principal stress on fracture. Clift *et al.* [170] integrated plastic work during deformation (equivalent stress over the plastic strain path). Noris *et al.* [171] and Oyane *et al.* [172] developed hydrostatic-stress-dependent weighting functions. The critical damage value is usually considered to be a calibration constant, but if a normalized definition is used for this value, fracture will occur once the damage parameter reaches unity. The self-similarity postulate suggests a normalized definition for damage evolution as a function of the ratio of current and fracture plastic strains under any proportional loading condition [173]:

$$\dot{D} = f(\frac{\bar{\varepsilon}^p}{\bar{\varepsilon}^f}) \tag{3}$$

The simple form of this expression can be obtained by considering a linear relationship between the damage parameter and equivalent plastic strain:

$$D = \int_{\bar{\varepsilon}^p} \frac{d\bar{\varepsilon}^p}{\bar{\varepsilon}^f} \tag{4}$$

Given Equation (2), the weighting function here is the inverse form of fracture plastic strain. Johnson and Cook [174] used this damage model by considering a stress triaxiality-temperature-strain rate-dependent function for fracture strain. However, it was experimentally demonstrated that damage sometimes evolves non-linearly with plastic deformation. For this reason, Xue [173] developed a power-law function for damage (Equation (5)) based on the Manson-Coffin fatigue model [175,176] assuming low-cycle behavior:

$$D = \int dD = \int d[(\frac{\bar{\varepsilon}^p}{\bar{\varepsilon}^f})^n] = \int_{\bar{\varepsilon}^p} n(\frac{\bar{\varepsilon}^p}{\bar{\varepsilon}^f})^{n-1} \frac{d\bar{\varepsilon}^p}{\bar{\varepsilon}^f} \tag{5}$$

In Equation (5), n is the damage exponent and needs to be determined by the calibration of the model on the basis of empirical results. Neukamm *et al.* [177] later called this model the Generalized Incremental Stress-State-dependent damage MOdel (GISSMO).

Based on the dependency of material ductility on deviatoric and hydrostatic stresses, several expressions have been suggested for fracture strain as a function of representatives of these stress states, *i.e.* the Lode parameter (ξ) and stress triaxiality (η) that are defined in Equations (6) and (7) [178]:

$$\xi = \frac{27 J_3}{2\bar{\sigma}^3} \tag{6}$$

$$\eta = \frac{\sigma_m}{\bar{\sigma}} \tag{7}$$

where J_3, $\bar{\sigma}$, and σ_m are the third invariant of the deviatoric stress tensor, equivalent stress, and hydrostatic stress, respectively. Wilkins *et al.* [178] first developed a fracture-strain function by assuming the individual effects of η and ξ and symmetry of fracture strains around the Lode parameter of zero for distinct stress triaxiality. Wierzbicki and Xue [179] proposed a symmetric but coupled (in terms of η and ξ effects) fracture-strain function. Bai and Wierzbicki [180] developed an asymmetric coupled fracture-strain function by discussing the non-symmetry of the fracture surface with respect to the Lode parameter and invoking Bao's work [160].

An alternate form of the CCM models is a fracture function in the stress space in the same manner as a yield criterion (Equation (8)):

$$F(\sigma_{ij}) = 0 \tag{8}$$

In such models, material fracture is defined as the moment at which the fracture function becomes zero for the existing stress state. The maximum shear stress (Tresca) [181], Mohr-Coulomb (MC) [182,183], pressure-modified maximum shear stress [184], Hosford-Coulomb (HC) [185], and Khan-Liu (Magnitude of the Stress Vector (MSV)) [186] models are examples of known fracture criteria in stress space. Two approaches are employed for the use of such criteria in cases in which the stress state varies during plastic deformation (non-proportional loading). The first is to

exclusively apply the fracture criterion, even if the stress state changes [186,187]. Such approaches assume that strain to fracture does not rely on the stress-state history. The second is to link the damage-indicator expressions, *e.g.* Equation (5), with the fracture models. For this purpose, the fracture criterion will generally need to be transferred to the mixed stress-strain or strain space (fracture strain as a function of stress state or strain ratio, respectively) by using a suitable hardening law [34]. Bai and Wierzbicki [188] and Mohr and Marcadet [185] transferred the MC and HC fracture models to the mixed stress-strain space using the Bai-Wierzbicki [180] and combined Voce [189]-Swift [190] hardening laws, respectively. Jia and Bai [191] transferred the resulting modified MC (MMC) model to the strain space given the relationships between the stress triaxiality and strain ratio as well as Lode parameter under the plane-stress condition.

Combining the MFH technique with a CCM model, a multi-functional predictive strategy for multi-phase steels has recently been developed in which the flow behavior of the material is approximated *via* micromechanical modelling, and its fracture response is simultaneously estimated using a distinct fracture criterion in each constituent phase. Pierman *et al.* [129] estimated the fracture strength of various ferritic-martensitic DP steels during their MFH modelling by defining a critical stress (1300 MPa) for the maximum principal stress in martensite. Srithananan *et al.* [135] predicted the fracture strain limits of a bainitic-martensitic Usibor® 1500-AS steel through FE micromechanical modelling by tracking the damage evolution within each constituent phase using a linear GISSMO damage model. Östlund *et al.* [192] and Golling *et al.* [53] predicted the fracture strains of grooved tensile samples comprised of various microstructures of heat-treated Al-Si-coated 22MnB5 using an MFH approach by considering the stress-based MSV damage model [186] for each constituent phase. Furthermore, Östlund *et al.* [192] calculated the fracture *loci* of bainitic-martensitic microstructures based on the same method; however, the predictions (Figure 5) do not show the typical shape of fracture *loci* of ductile metals, *i.e.* with two valleys in the mixed-shear-tension and drawing-stretching zones.

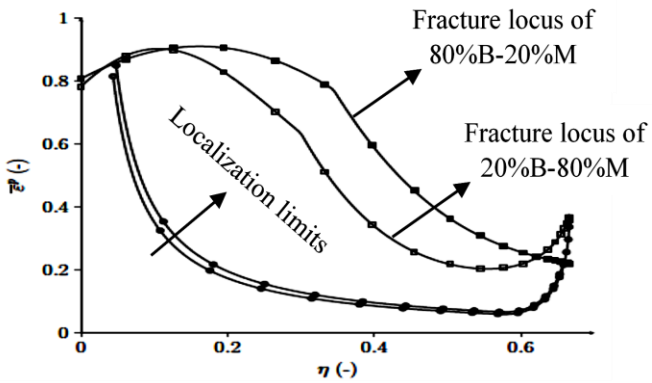

Figure 5: The predicted fracture *loci* of bainitic-martensitic Al-Si-coated 22MnB5 based on the damage-predictive framework employed by Östlund *et al.* [192].

The main drawback of conventional continuum mechanics fracture models is that they do not provide insight into the physical processes leading to material fracture; however, due to their simplicity, they are the most widely-used models in industry [160,163]. A comparative study of several ductile-fracture models, introduced in this section, can be found in the work by Cao *et al.* [193].

2.7. Summary

The previous sections served to establish: (i) the important role and potential of press-hardening steels and their TWBs in the hot-stamped condition to improve the crashworthiness of cars; and (ii) the different modelling approaches that can be employed for the prediction of the constitutive (flow) and fracture behavior of such materials. As mentioned before, Usibor® 1500-AS and Ductibor® 500-AS, in the forms of hot-stamped laser-welded blanks, can be used to fabricate components with high strength and ductility in different regions, suitable for energy-absorbing structures of automobiles. It is evident, however, that no comprehensive study to-date has been carried out on the flow and fracture characterization and modelling of Ductibor® 500-AS, as one of the parent materials of such TWBs, as well as the TWBs themselves as a function of microstructure. Given the fact that various cooling rates are experienced during the conventional and tailored hot-stamping processes, due to variations in the working conditions such as the local temperature and die pressure, the resultant microstructures and mechanical properties of hot-stamped components are susceptible to change. Thus, the sensitivity of the mechanical properties of steel blanks to the as-quenched microstructure (quench rate) plays a significant role in the mechanical response of the final products. Accordingly, there exists a need to investigate the flow

and fracture response of Ductibor® 500-AS and the hot-stamped laser-welded blanks of this steel and Usibor® 1500-AS such that the influences of variations in their microstructures under different working condition are incorporated. Moreover, a predictive tool is required to be able to estimate the flow and fracture behavior of the hot-stamped Usibor® 1500-AS and Ductibor® 500-AS and their TWBs in terms of microstructure to support the design of relevant structural components. This research aims to address these gaps in the published literature and provide insight into the interaction of the microstructure and mechanical response of such materials.

Chapter 3: Research Objectives and Scope

3.1. Research Objectives

The overall goal of this research is to support the introduction of hot-stamping steels and their TWBs within automotive structures, thereby advancing automotive weight reduction and enhanced safety. This research project will contribute to the understanding of the relationship between the microstructure with the constitutive (flow) and fracture behavior of hot-stamped monolithic and tailor-welded blanks. The primary focus will be on the 1.2-mm and 1.6-mm hot-stamped Usibor® 1500-AS and Ductibor® 500-AS sheets as well as their laser-welded combinations within TWBs. The specific objectives of this research are outlined as follows:

1- Experimental characterization of constitutive and fracture response of Usibor® 1500-AS and Ductibor® 500-AS parent metals for a wide range of as-quenched microstructures and stress states;

2- Experimental characterization of constitutive and fracture response of hot-stamped TWBs of Usibor® 1500-AS and Ductibor® 500-AS for various weld orientations and loading conditions;

3- Microstructure-based modelling of constitutive and fracture response of parent metals; and

4- Numerical modelling of constitutive and fracture response of hot-stamped TWBs.

3.2. Research Scope

To fulfill the objectives of this research project outlined in Section 3.1, four primary tasks were defined, which are detailed in the following:

3.2.1. Task 1: Experimental work for Characterizing Constitutive and Fracture Response of Parent Metals for a Wide Range of As-Quenched Microstructures and Stress States

A wide range of the as-quenched microstructures of the parent metals was produced by the quench-hardening heat treatment of the blanks at various cooling rates, and the resultant

microstructures and hardness were subsequently investigated. The constitutive (flow) behavior was characterized using uniaxial tension tests, considering the 0°, 45°, and/or 90° directions with respect to the rolling direction. The fracture response was examined through a set of mechanical tests under various loading conditions ranging from simple shear to biaxial tension with a focus on the weaker material direction (transverse). The characterization experiments were mainly focused on the 1.2-mm-thick sheets.

It is noted that for Usibor® 1500-AS, the cooling-rate range of 14-50 ºC/s was employed that encompasses the range normally utilized in the in-die heating tailored hot-stamping process for producing graded properties within a single blank [2,42]. The characterization work for this material was conducted by ten Kortenaar [89] and Omer [194]. However, for Ductibor® 500-AS, since the quench-rate sensitivity had not been studied previously, a much wider range of cooling rates (*i.e.* 5-1890 ºC/s) was considered to discover how its microstructure and mechanical properties vary. This material was characterized as part of the present research.

3.2.2. Task 2: Experimental work for Characterizing Constitutive and Fracture Response of Hot-Stamped TWBs for Various Weld Orientations and Loading Conditions

Microstructural and hardness investigations were first performed across the weld zone and within the parent metals of both as-received and hot-stamped TWBs. The constitutive (flow) and fracture behavior of the hot-stamped TWBs were then examined *via* several mechanical experiments considering different weld orientations and loading conditions. The characterization campaigns were conducted on mono- and multi-gauge TWBs with 1.2- and 1.6-mm-thick thickness combinations of the parent metals.

3.2.3. Task 3: Numerical Strategies for Microstructure-Based Modelling of Constitutive and Fracture Response of Parent Metals

To model the constitutive (flow) and fracture behavior of the parent metals for a range of microstructures, a coupled micromechanical-phenomenological strategy was proposed. In this approach, the flow response of the parent metals, together with stress/strain partitioning between their constituent phases, was calculated using mean-field homogenization techniques. Simultaneously, damage accumulation within the constituent phases was computed using the

GISSMO damage indicator [177] defined in each micro-constituent, linked to their fracture *loci*. Fracture in the parent metals was predicted as the GISSMO damage parameter reached unity in any of the phases. The predicted flow and fracture response from this task were finally assessed against the measured data from Task 1.

3.2.4. Task 4: Numerical Strategies for Finite-Element (FE) Modelling of Constitutive and Fracture Response of Hot-Stamped TWBs

To model the mechanical behavior of the hot-stamped TWBs, FE simulations of various fracture tests were conducted within the LS-DYNA software. For this purpose, the hardness-mapped models of the TWB specimens were developed using a user-defined material (UMAT) subroutine given the hardness measurements from Task 2. Then the mechanical properties corresponding to the hardness of each region of the TWB models were assigned to the respective elements using the measured or calculated material data from Task 1 or 3. In order to assess the significance of the modelling of the weld zone within the TWBs, simulations were also conducted with the neglect of the weld region. Then both TWB models ("with weld" and "without weld") were evaluated by comparisons of the simulation results with the measured data from Task 2.

Chapter 4: Research Results

The current research concentrated on the 1.2-mm-thick Usibor® 1500-AS and Ductibor® 500-AS sheets as the primary materials of interest. The chemical compositions of these two alloys are presented in Table 1. Mono- and multi-gauge laser-welded blanks of these two steels, with the thickness combinations given in Table 2, were also considered. It is noted that the parent-metal sheets and their TWBs were all provided by ArcelorMittal.

Table 1: The chemical compositions of the 1.2-mm-thick parent materials (wt.%)

Material	C	Mn	Ti	Nb	Al	Si	P	N	S	B
Usibor® 1500-AS	0.23	1.21	0.03	0.002	0.051	0.25	0.016	0.005	0.001	0.003
Ductibor® 500-AS	0.060	1.545	0.069	0.047	0.035	0.032	0.016	0.0067	0.002	0.001

Table 2: The TWBs with various thickness combinations considered in this research

TWB	Designation
1.2-mm-thick Ductibor® 500-AS—1.2-mm-thick Usibor® 1500-AS	1.2D-1.2U
1.2-mm-thick Ductibor® 500-AS—1.6-mm-thick Usibor® 1500-AS	1.2D-1.6U
1.6-mm-thick Ductibor® 500-AS—1.6-mm-thick Usibor® 1500-AS	1.6D-1.6U

This chapter summarizes the results of the experimental and numerical investigations of the studied materials in different as-quenched conditions, performed to address the research objectives defined in Chapter 3. It opens the experimental characterization results for the various as-quenched microstructures of the parent metals (Task 1) and their hot-stamped TWBs (Task 2). Its balance is comprised of the predictions of the constitutive (flow) and fracture behavior for the as-quenched parent metals (Task 3) and their TWBs (Task 4). It is noted that a more detailed presentation of the results can be found in Appendices A-E, each of which includes a published or submitted peer-reviewed paper:

Appendix A P. Samadian, L. ten Kortenaar, K. Omer, C. Butcher, M. J. Worswick, Fracture Characterization of Tailored Usibor® 1500-AS and Damage Modelling Based on a Coupled-Micromechanical-Phenomenological Strategy, *Engineering Fracture Mechanics*, vol. 223, p. 1-20, 2020.

Appendix B P. Samadian, C. Butcher, M. J. Worswick, Microstructures and Flow Behavior of Ductibor® 500-AS Steel for a Range of As-Quenched Conditions, *Journal of Materials Engineering and Performance*, vol. 29 (11), p. 7153–7169, 2020.

Appendix C P. Samadian, C. Butcher, M. J. Worswick**,** A Mean-Field Homogenization Approach to Predict Fracture in As-Quenched Microstructures of Ductibor® 500-AS Steel: Characterization and Modelling, under review for publication in *International Journal of Solids and Structures*, 2020.

Appendix D P. Samadian, C. O'Keeffe, C. Butcher, M. J. Worswick, Fracture Response in Hot-Stamped Tailor-Welded Blanks of Ductibor® 500-AS and Usibor® 1500-AS: Experiments and Modelling, under review for publication in *Engineering Fracture Mechanics*, 2020.

Appendix E P. Samadian, C. Butcher, M. J. Worswick, New Mean-Field Homogenization Schemes for the Constitutive Modelling of the Elastic and Elastoplastic Deformation Behavior of Multi-Phase Materials, *Materials Today Communications*, vol. 24, p. 1-13, 2020.

4.1. Task 1: Characterization of Parent Metals

This section presents the characterization studies performed on the as-quenched Ductibor® 500-AS sheet for a range of cooling rates. It is noted that the detailed characterization of the as-quenched microstructures of the Usibor® 1500-AS sheet was not performed as part of this research since it was already conducted by ten Kortenaar [89] and Omer [194] in a related study using the same material lot. Nonetheless, a summary of their experimentation and obtained results that were used in the current research can be found in Appendix A, which contains an article about the fracture characterization and modelling of a range of the as-quenched microstructures of Usibor® 1500-AS.

4.1.1. Microstructure and Hardness

To determine the role of quench rate during hot stamping on the resulting microstructure of Ductibor® 500-AS, the 1.2-mm-thick sheets of this steel were subjected to various heat treatments. The 203.2 mm × 203.2 mm blanks were initially austenitized at 930 °C for 6.5 minutes in a Deltech furnace with an air atmosphere and then cooled to room temperature in either air (≈ 5 °C/s), between chilled flat dies with a 7 °C temperature under a contact pressure of 15 MPa for 15 s (≈ 365 °C/s), or in water (≈ 1890 °C/s). To investigate the final microstructures of the different

material conditions using light optical and scanning electron microscopy (LOM and SEM, respectively), small specimens from the as-quenched blanks were cut and mounted in resin-epoxy pucks for metallurgical examination. The through-thickness surfaces were ground and polished using the 300-to-2400 grit size SiC sandpaper and 1-to-1/4 μm diamond paste, respectively, and subsequently etched using a 5% Nital solution. The hardness of the samples was also measured using a microhardness tester by means of a Vickers indenter with a 1 kgf load applied for 15 s. Figure 6 shows LOM and SEM images of the as-quenched microstructures, and Table 3 presents the results of phase quantity analyses based on the systematic manual point-count method [195] as well as measured hardness values of the different as-quenched samples. As can be seen, the air-cooled condition has a mostly-ferritic microstructure and the lowest hardness value (167 HVN). The die- and water-cooled conditions, due to the higher cooling rates, have lower ferrite contents (57.4% and 10.1%), higher amounts of the harder phases of martensite and tempered martensite/bainite (42.6% and 89.9% in total), and, as a result, higher hardness values (248 HVN and 341 HVN), respectively. More details about the heat treatments, as-quenched microstructures, and phase quantity analyses can be found in Appendix B.

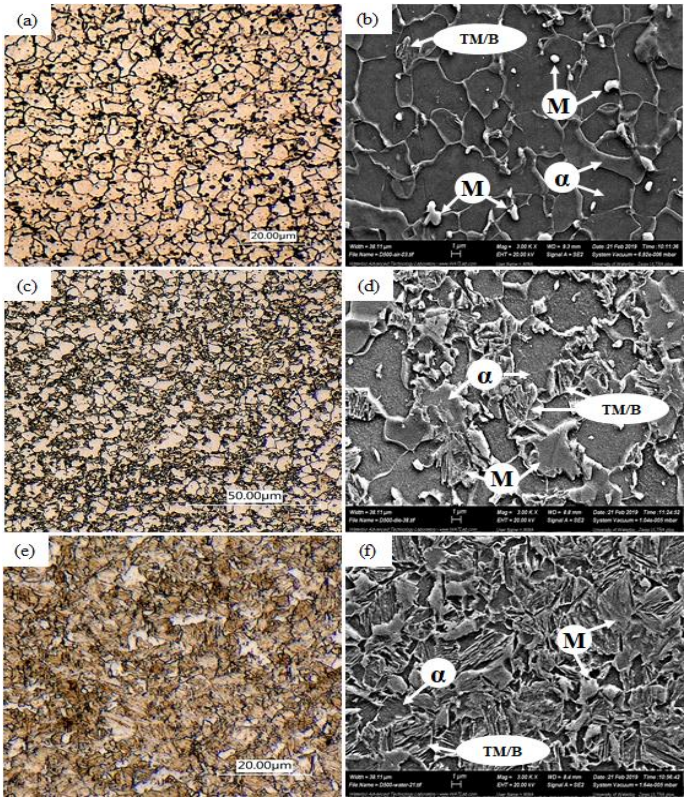

Figure 6: LOM and SEM images of the as-quenched microstructures of Ductibor® 500-AS; (a),(b) air-, (c),(d) die-, and (e),(f) water-cooled (α: ferrite, M: martensite, and TM/B: tempered martensite/bainite).

Table 3: The results of the phase quantity analyses and measured hardness for the as-quenched microstructures of Ductibor® 500-AS
(Note: the indicated variations represent the standard deviations of the measured data.)

Material Condition	F (%v)	M (%v)	TM/B (%v)	Measured hardness (HVN)
Air-cooled	95.7 ± 2.0	4.3 ± 2.0	trace	167 ± 3
Die-cooled	57.4 ± 6.5	30.7 ± 3.8	11.9 ± 3.1	248 ± 3
Water-cooled	10.1 ± 2.3	77.8 ± 3.8	12.1 ± 1.5	341 ± 6

4.1.2. Constitutive Behavior

To characterize the constitutive (flow) response of the different material conditions of Ductibor® 500-AS, Standard JIS Z2201 No. 5 uniaxial tension samples (Figure 7) [196] were cut from the various as-quenched blanks along the transverse direction (TD). Anisotropy analysis was conducted only on the die-cooled Ductibor® 500-AS, so tensile specimens along the rolling and diagonal directions (RD and DD, respectively) were also prepared for this material condition. A 100-kN MTS Criterion 45 servo-electric tensile frame was used to carry out the tests at a strain rate of 0.01 s^{-1}. At least 5 repeat tests were conducted for each material condition. Stereoscopic digital imaging correlation (DIC) techniques by means of Point Grey Research GRAS-50S5M-C cameras and the Vic3D Correlated Solutions DIC software were utilized to acquire strain distributions over the areas of interest. The samples were sandblasted before testing to remove the Al-Si coating, thereby avoiding the decohesion of the painted DIC speckle pattern during testing. A virtual strain gauge length (VSGL) [197] of 0.3 mm using step and filter sizes of 1 pixel and 5, respectively, was employed for the DIC analyses. The engineering-strain values were measured using three 50-mm virtual extensometers in the Vic-3D software. The material separation was considered to correspond to the onset of fracture.

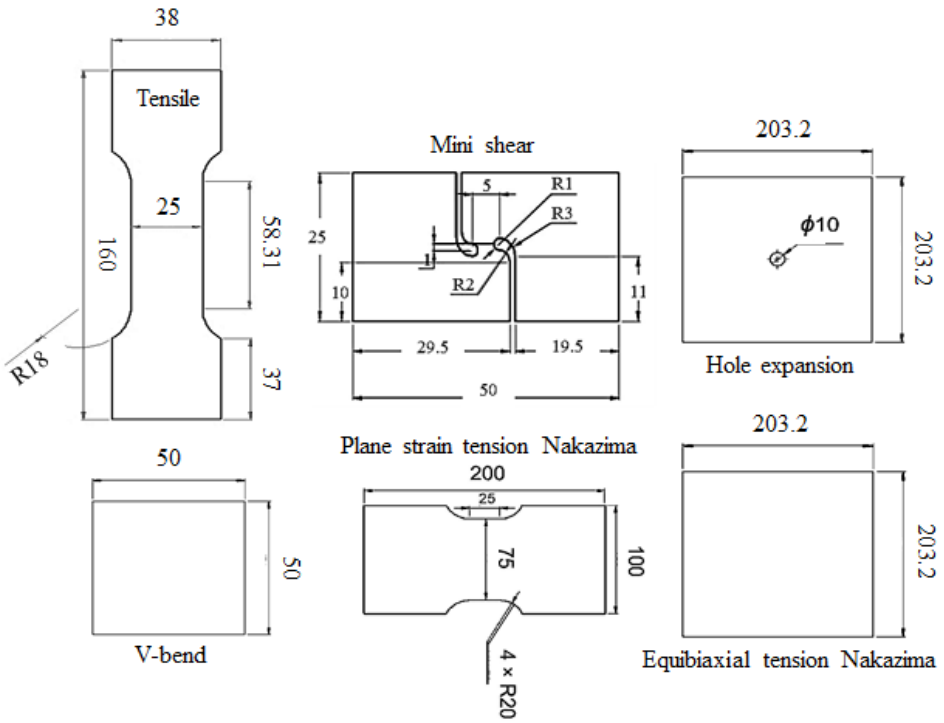

Figure 7: The geometries of testing specimens (unit: millimeter) [89], [196].

Figure 8 illustrates the engineering stress-strain curves of the different as-quenched conditions of Ductibor® 500-AS, and Tables 4 and 5 present summaries of the measured mechanical properties and anisotropy analysis, respectively. It is evident that the water-cooled condition has the highest strength level and lowest elongation to fracture, which is due to its higher amount of the harder martensitic phase (Table 3). With the decrease in the martensite content and increase in the amount of the softer ferritic phase in the die- and air-cooled conditions, the strength decreased, while elongation to fracture increased. Interestingly, the stress-strain curve of the air-cooled condition displays a yield-point phenomenon, which is a result of the formation of Lüders bands along the gauge length of the specimens due to the pinning of dislocations by the interstitial alloying elements of carbon and nitrogen (Table 1) [127]. Table 4 reveals that the level of anisotropy in terms of the measured stress ratios is relatively moderate in the die-cooled condition, with less than 5% variation with material direction. However, there is significant plastic anisotropy in terms of the Lankford coefficients (R-values), which range from 0.58 to 1.39 depending upon the material direction. Tensile tests were not conducted along the RD and DD for the air- and water-cooled conditions; however, the R-values of the air- and water-cooled conditions acquired along the transverse direction were 0.82 ± 0.06 and 0.80 ± 0.08, respectively, which are very close to the transverse direction R-value for the die-cooled condition (0.82 ± 0.06). More details about

the constitutive and anisotropy analyses, including the flow response in simple shear loading and yield surface of the die-cooled condition, can be found in Appendix B.

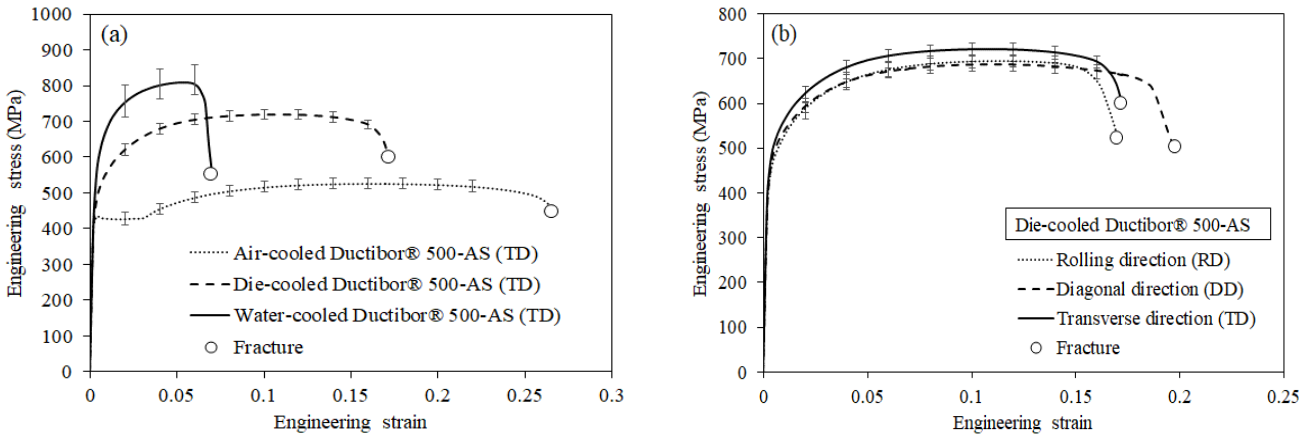

Figure 8: The engineering stress-strain curves of the different as-quenched conditions of Ductibor® 500-AS along the various material directions.

Table 4: A summary of the mechanical properties of the different as-quenched conditions of Ductibor® 500-AS
(Note: the indicated variations represent the standard deviations of the measured data.)

Material condition	UTS (MPa)	Elongation to fracture (ef %)
Air-cooled	525 ± 11	27.1 ± 0.4
Die-cooled	721 ± 11	17.6 ± 0.5
Water-cooled	810 ± 29	7.3 ± 0.8

Table 5: A summary of the anisotropy analysis on the die-cooled Ductibor® 500-AS

Orientation	R-value[a]	Stress ratio[b]
RD	0.58 ± 0.01[c]	1 ± 0.02
DD	1.39 ± 0.04	0.99 ± 0.01
TD	0.82 ± 0.06	1.03 ± 0.02

Notes:
a: R-values were calculated over the range corresponding to 1% elongation to the maximum uniform elongation (at the UTS point);
b: stress ratios were obtained with respect to the stress along the RD for the same level of plastic work (68.3 MJ/m^3) corresponding to the weakest direction (DD) at the UTS point; and
c: the indicated variations correspond to the standard deviations of the measured data.

4.1.3. Fracture Response

To acquire the fracture *loci* of the different as-quenched conditions of Ductibor® 500-AS, mini shear, hole-expansion, and plane-strain tension and equibiaxial tension Nakazima dome tests were carried out for each material condition. The sample geometries are shown in Figure 7. Mini shear tests were conducted by means of a 100-kN MTS hydraulic tensile frame at a strain rate of

0.01 s^{-1}. The hole-expansion and Nakazima dome tests were performed using an MTS dome tester apparatus with conical (60° angle) and hemispherical punches, respectively. A punch speed of 0.25 mm/s and binder force of 660 kN were applied. The binder and die were equipped with male and female lock beads, respectively. To decrease friction with the punch and obtain a fracture closer to the top of the dome, three sheets of Teflon coated with petroleum jelly were used between the punch and samples. Stereoscopic DIC techniques, with the conditions described in Section 4.1.2, were utilized. The principal strain values of the mini shear and Nakazima dome tests were extracted from 0.25 mm × 0.4 mm rectangular- and 0.5-mm-radius circular-shaped sampling areas of interest, respectively. The fracture strains of the hole-expansion samples were calculated based on the measurement of the initial and final outer diameters of the hole from the corresponding images, assuming a uniaxial tension loading state at the hole edges. Since the determination of the onset of fracture in the mini shear tests was visually difficult, the instant of maximum load was taken as corresponding to the onset of fracture. This approach is expected to provide conservative estimates for the shear fracture strains [197]. However, for the hole-expansion and Nakazima dome tests, fracture initiation was taken as the occurance of the first visible crack. Through-thickness localized necking generally precedes fracture during Nakazima dome tests, and thus, DIC surface measurements cannot resolve actual fracture strains. Therefore, the DIC fracture strains of the plane-strain and equibiaxial tension Nakazima dome specimens were corrected by post-mortem thickness measurements at the fracture points based on a plane-strain assumption [198]. The number of repeat experiments for each condition was at least 4.

Figure 9 shows the surface strain paths experienced during the various fracture tests as well as the fracture points for each as-quenched condition of Ductibor® 500-AS, and Figure 10 presents the corresponding von Mises fracture strains. It can be seen that the measured strain paths are very similar for all of the material conditions in the different fracture tests except in the case of the equibiaxial tension Nakazima dome testing for the water-cooled condition. Such a difference is attributed to the occurrence of off-center fractures in the water-cooled samples, stemming from warpage that occurred during water quenching. The plane strain and equibiaxial tension Nakazima dome tests exhibited partially non-linear strain paths due to the initial out-of-plane biaxial bending induced by the hemispherical punch and through-thickness localization necking, respectively. It is also evident that all of the material conditions underwent less deformation under the stretching strain states (plane strain and biaxial tension) compared to the uniaxial tension and simple shear

loading states. The air-cooled condition experienced the highest strains before fracture (the highest ductility) in all of the loading conditions, followed by the die- and water-cooled conditions, respectively. These results are consistent with the microstructural and hardness measurements, presented in Section 4.1.1, that showed that the air-cooled microstructure with a mostly-ferritic microstructure had the lowest hardness, while the die- and water-cooled microstructures with higher amounts of total harder phases had the higher hardness, respectively. Comparing the DIC- and thickness measurement-based fracture strains from the Nakazima dome tests indicates that a noticeable increase in major principal (and equivalent) strain occurred between the onset of necking and fracture in all of the material conditions, specifically during the plane-strain tension Nakazima dome tests. As discussed earlier, such a difference is attributed to the limitation of the DIC measurements to the specimen surface, whilst fracture normally initiates within the necked region through the sample thickness during the Nakazima dome tests.

More details about the experimentation and measured fracture data, including strain distributions and stress states, can be found in Appendix C.

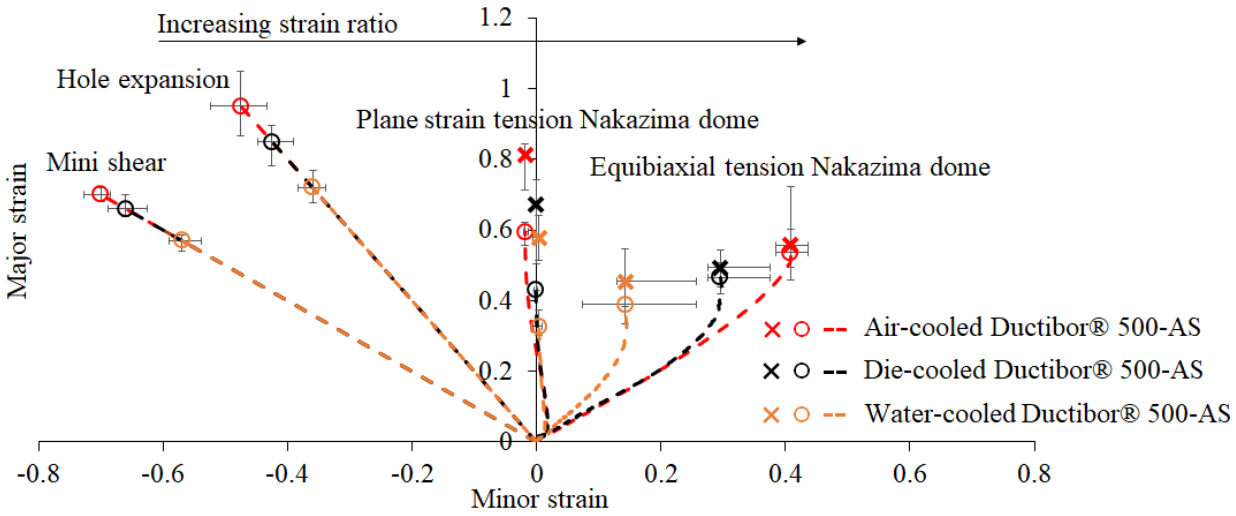

Figure 9: The surface strain paths of the different as-quenched conditions of Ductibor® 500-AS in the various fracture tests. Note that the "o" and "×" symbols represent the fracture points based on the DIC techniques and thickness measurements, respectively, and the error bars indicate the measured data variations.

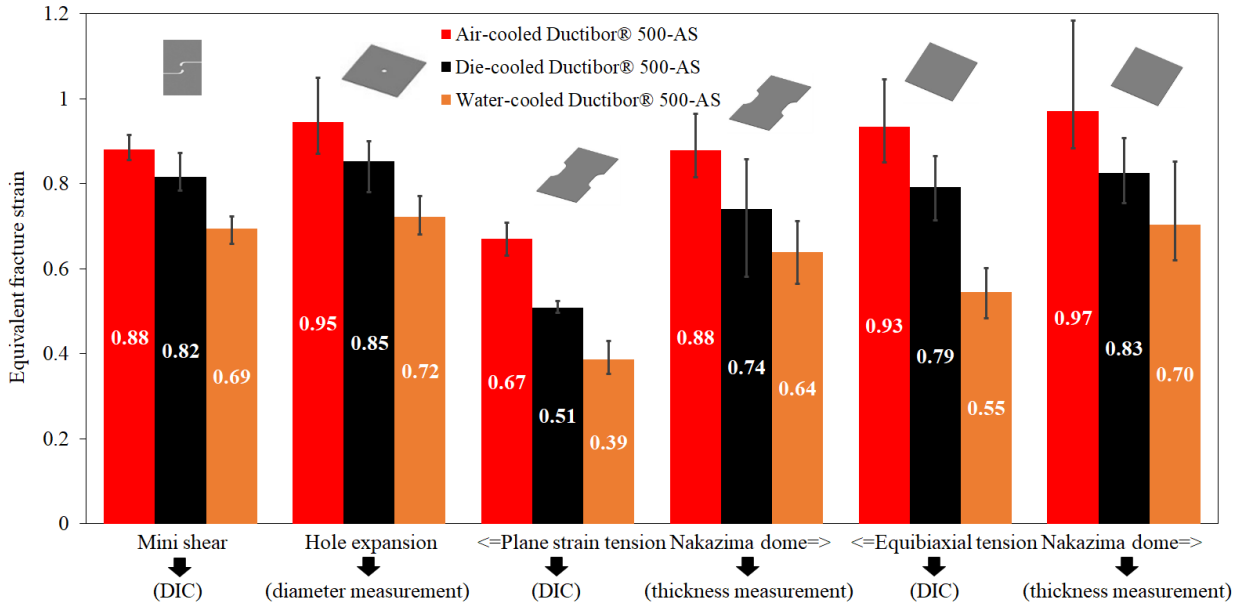

Figure 10: The equivalent fracture strains of the different as-quenched conditions of Ductibor® 500-AS in the various mechanical tests. Note that the error bars represent the measured data variations.

4.2. Task 2: Characterization of Hot-Stamped TWBs

This section incorporates a summary of the characterization work performed on the hot-stamped mono- and multi-gauge TWBs of Usibor® 1500-AS and Ductibor® 500-AS.

4.2.1. Microstructure and Hardness

The hot-stamping (die-quenching) process and the microstructure and hardness investigations of the TWBs were carried out in the same manner as those explained in Section 4.1.1 for the monolithic Ductibor® 500-AS blanks. Figures 11 and 12 illustrate the microstructure and hardness variations across the weld of the as-received and hot-stamped TWBs, respectively. In the as-received condition, the microstructure of Usibor® 1500-AS was comprised of ferrite and pearlite with alloy carbides dispersed mostly within the ferritic grains. Martensite was also found locally on the ferritic grain boundaries. The fusion zone was composed of a completely-martensitic microstructure. The microstructure within the Ductibor® 500-AS side of the TWBs was constituted of a continuous ferritic matrix with a small amount of martensite, either trapped inside the ferritic grains or on the ferritic grain boundaries. The microhardness results are consistent with the microstructural observations such that the average hardness was high in the fusion zone (452-531 HVN) and dropped to that of the soft parent metals on either side of the weld, *i.e.* 199-204 HVN

for Ductibor® 500-AS and 180-201 HVN for Usibor® 1500-AS. In the hot-stamped condition, the Usibor® 1500-AS region, with an average hardness within the range of 480-495 HVN, exhibited a fully-martensitic microstructure. Ductibor® 500-AS in the hot-stamped mono-gauge TWBs exhibited a microstructure composed of approximately 57% ferrite, 31% martensite, and 12% tempered martensite/bainite (Figure 6 and Table 3), with average hardness of approximately 248 HVN, which is consistent with that of the die-cooled monolithic Ductibor® 500-AS sheet. However, the Ductibor® 500-AS sheet within the multi-gauge TWB exhibited a microstructure constituted of 73% ferrite and 27% martensite (Figure 12), with a lower hardness value of 218 HVN. The softer condition of Ductibor® 500-AS in the multi-gauge TWB suggests a lower cooling rate, possibly due to the use of a stepped die to account for the different thicknesses of the two parent sheets.

It is interesting to note that the hardness in the weld zone of the thermally-processed TWBs varied almost monotonically across the 1.6-mm width of the weld line between the hardness levels of the parent metals. The center of the weld exhibited a mostly-martensitic microstructure with some ferrite and tempered martensite/bainite. Moving from the weld center, the martensite content increased towards the Usibor® 1500-AS side and decreased towards the Ductibor® 500-AS side. This phenomenon is attributed to the variation of material hardenability across the weld. Such a gradient in hardenability stems from the mixing of the two alloys during welding and carbon migration from the higher carbon-concentration Usibor® 1500-AS sheet towards the lower carbon-concentration Ductibor® 500-AS sheet (See Table 1) during the austenitization stage of hot stamping. Details about the microstructural variations within the HAZs of the as-received and hot-stamped TWBs can be found in Appendix D.

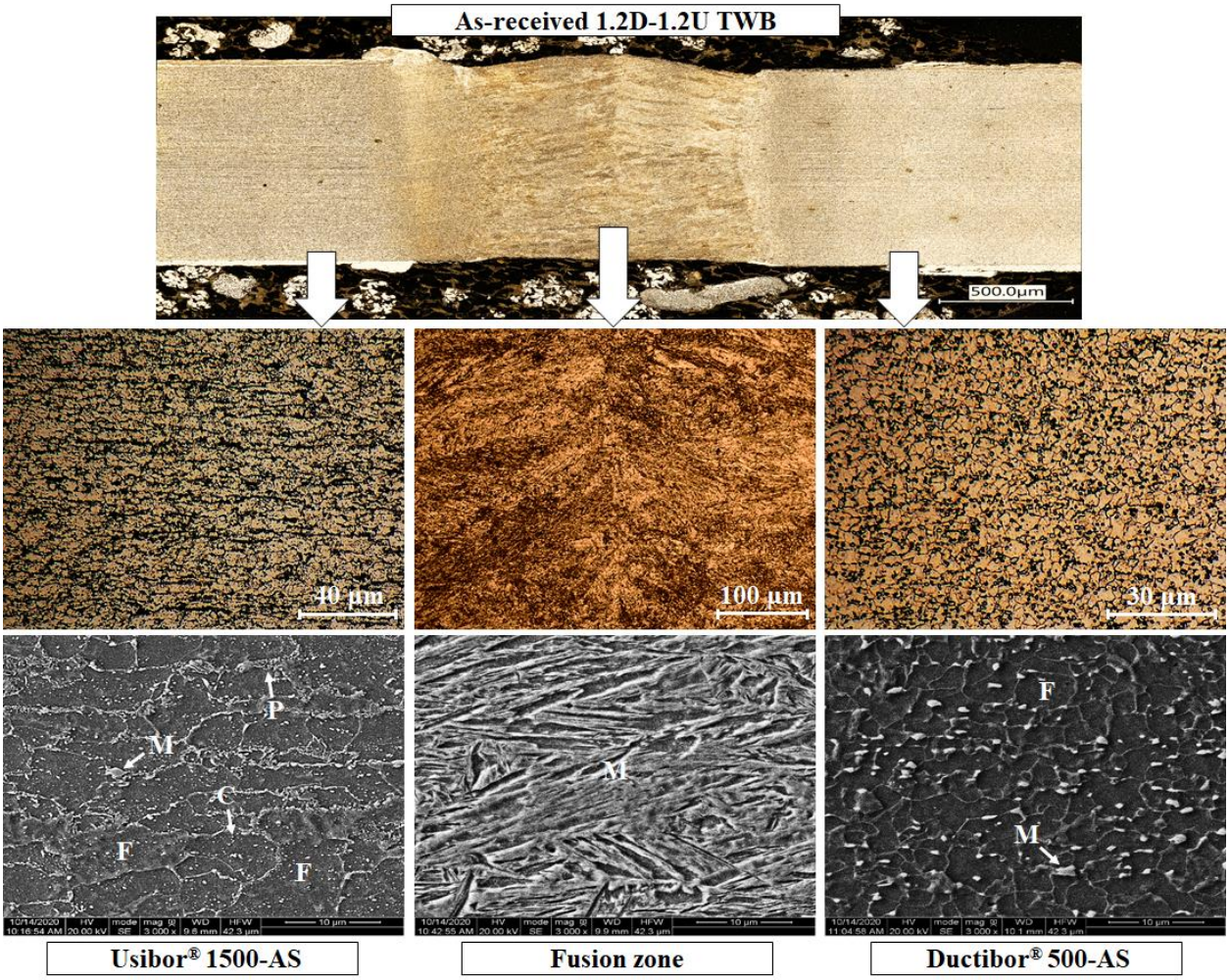

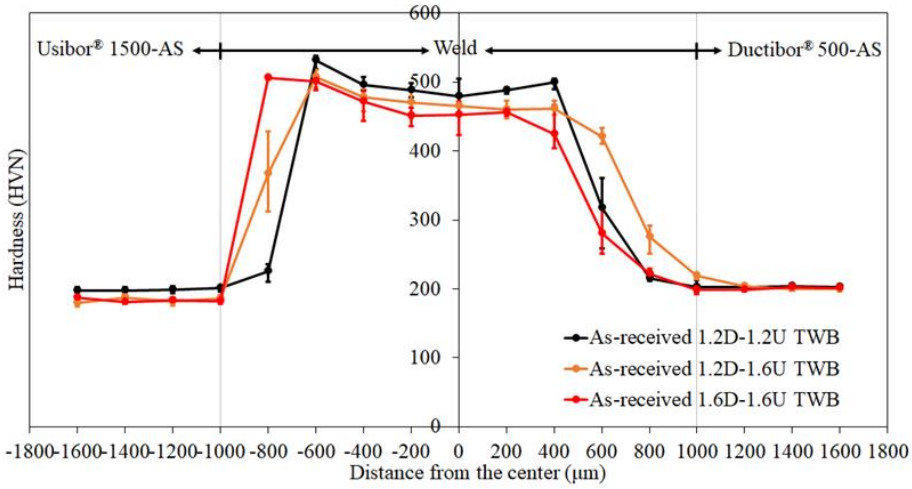

Figure 11: The microstructure and hardness variations of the as-received TWBs across the weld.

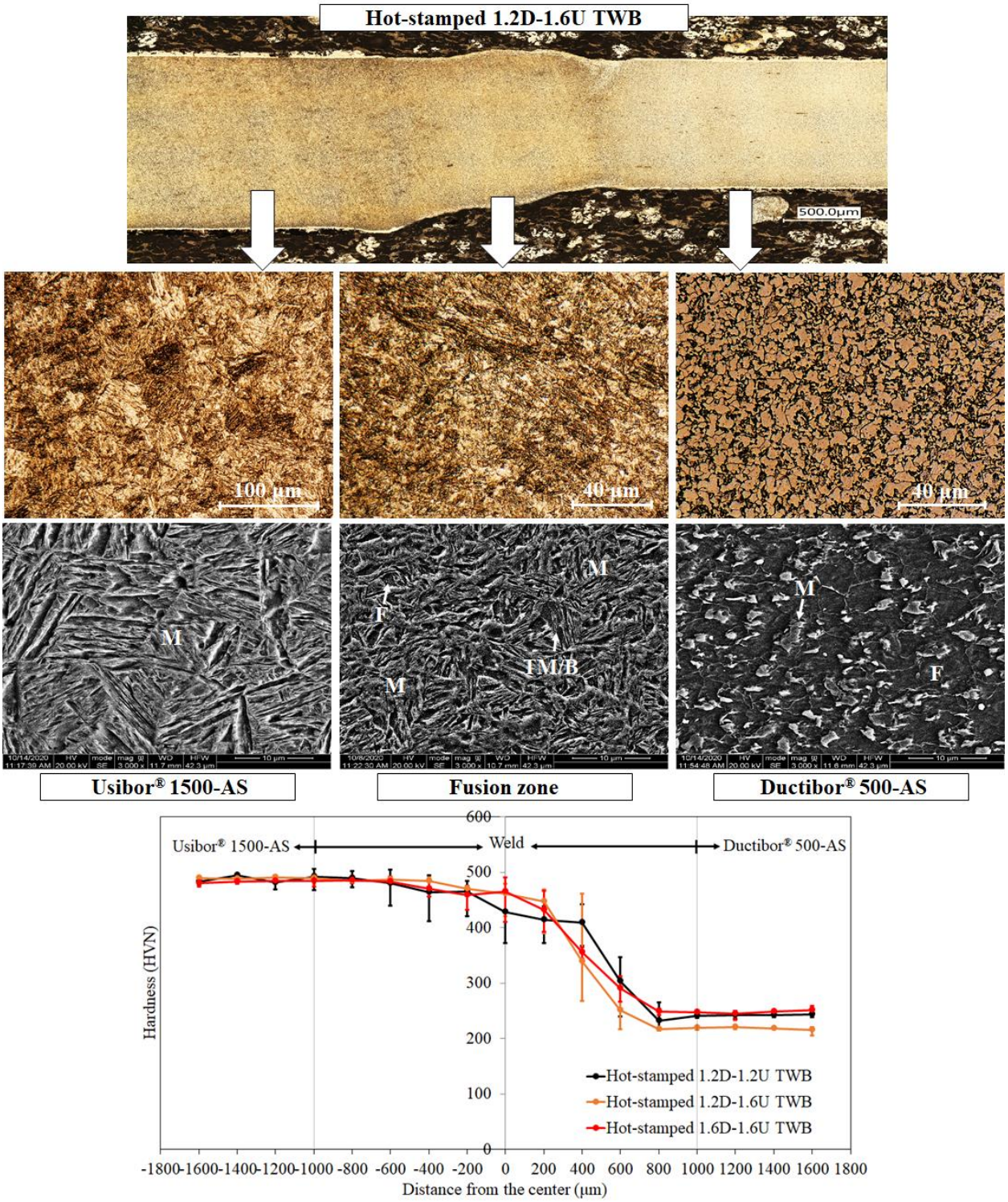

Figure 12: The microstructure and hardness variations of the hot-stamped TWBs across the weld.

4.2.2. Constitutive and Fracture Response

To examine the constitutive (flow) and fracture behavior of the hot-stamped TWBs, various mechanical tests, including uniaxial tension, equibiaxial tension Nakazima dome, and V-bend, were conducted with the sample geometries shown in Figure 7. The tensile specimens were cut from the hot-stamped blanks with a centrally-located weld line with either longitudinal or transverse orientations with respect to the loading direction. The Nakazima dome samples were prepared with the weld line in the middle of the specimens. The testing conditions for the tensile and Nakazima dome tests were similar to those described in Sections 4.1.2 and 4.1.3. It should be noted that the Nakazima dome samples were located in the tooling such that their centers were aligned with the axis of the punch. For the V-bend testing, samples with three different orientations (0°, 45°, and 90°) of the weld line with respect to the bending axis were prepared and tested by means of an inverted V-bend device [199] with a punch tip radius of 0.4 mm and a punch speed of 20 mm/min based on the VDA 238-100 specification [200].

Stereoscopic DIC techniques, with the same settings noted in Sections 4.1.2 and 4.1.3, were deployed for the strain-distribution measurements during all of the mechanical tests. The strain distributions across the weld line of the uniaxial tension and Nakazima dome specimens were obtained by exporting the strain data along line slices perpendicular to the weld line at the fracture-initiation locations. In the tensile tests, the engineering strains were measured using 50-mm virtual extensometers in the gauge sections of the specimens plotted in Vic-3D, and the onset of fracture was determined to be the moment of material separation. In the Nakazima dome tests, the local von Mises equivalent fracture strains were calculated based on the incremental integration of the principal strains extracted from 0.5-mm-radius circle inspector tools in Vic-3D positioned at the locations of the first visible cracks. To obtain the von Mises equivalent fracture strains of the V-bend samples, the strain paths at the points with maximum major strain, taken from five line slices perpendicular to the bend lines of the specimens in Vic-3D, were averaged. For these samples, fracture was defined based on the VDA standard, *i.e.* a 30 N load drop from maximum load for materials thinner than 2 mm [199]. It is mentioned that a minimum of 4 repeat tests was considered for each testing type. Moreover, the results of the fracture tests on the TWBs were compared with those of the 1.2- or 1.6-mm-thick parent metals, which were either reported in previous studies or obtained as part of the current study using the same mechanical testing procedures.

4.2.2.1. Tensile Test Results

Figures 13 and 14 show the engineering stress-strain curves of the longitudinal and transverse TWB tensile samples compared to those of the base metals, respectively. Moreover, a comparison of the UTS, elongation to maximum load, and elongation to fracture of the TWBs and parent metals is presented in Figure 15.

In the case of the longitudinal TWBs, the 1.6D-1.6U TWBs with 8.5% elongation to fracture exhibited the highest ductility, but the 1.2D-1.2U and 1.2D-1.6U TWBs underwent similar elongation to fracture (7.3-7.5%). The multi-gauge TWB exhibited around 4-5% higher strength since the thicker, higher-strength Usibor® 1500-AS was more engaged in the grips than the thinner, weaker Ductibor® 500-AS and, as a result, carried a higher fraction of total load compared to that in the case of the mono-gauge TWBs with the Usibor® 1500-AS and Ductibor® 500-AS sections equally engaged in the grips. The strength levels of the longitudinal TWBs (~ 1.15 GPa) lay between those of the parent metals (~ 0.7 GPa-1.6 GPa). However, their total elongation was lower than that of the parent metals but closer to that of the hot-stamped Usibor® 1500-AS, primarily since fracture initiation occurred within the Usibor® 1500-AS side of the specimen (Figure 16). These observations indicate that the fracture response of such longitudinally-oriented TWBs is largely controlled by the region with the lowest ductility.

The results of the mono- and multi-gauge transverse TWBs show that the 1.2D-1.6U TWBs had about 10%-15% lower strength but almost similar elongation (~ 10%) to fracture in comparison with the 1.2D-1.2U TWBs. The 1.6D-1.6U TWBs herein also exhibited the highest elongation prior to fracture (10.6%). Compared to the hardening behavior of the parent metals, the maximum strength and elongation of the transverse TWBs were similar to the UTS of the hot-stamped Ductibor® 500-AS and elongation of the hot-stamped Usibor® 1500-AS at fracture, respectively. However, contrary to the longitudinal TWBs, fracture was initiated in the Ductibor® 500-AS side in the transverse TWBs (Figure 17). Such observations indicate that deformation occurs primarily in the weaker parent metal of such transverse TWBs. Consequently, their strength is limited by the strength of the weaker sheet. The lower strength of the transverse 1.2D-1.6U TWBs relative to the two transverse mono-gauge TWBs is attributed to the lower martensite content and, as a result, the lower hardness and strength of the as-quenched Ductibor® 500-AS

sheet in the multi-gauge TWB (See Section 4.2.1). The induced bending due to the offset of the two sheets may also have contributed to the lower tensile strength and elongation of the multi-gauge TWB under transverse loading.

It should be noted that elongation to maximum load for both longitudinal and transverse TWB tensile samples was almost in the same range (~ 5.5%) and between that for the parent metals but closer to that of the hot-stamped Usibor® 1500-AS. Moreover, a comparison of the mechanical response of all tensile TWBs reveals that the longitudinal specimens have higher strength, whilst the transverse TWBs have higher ductility.

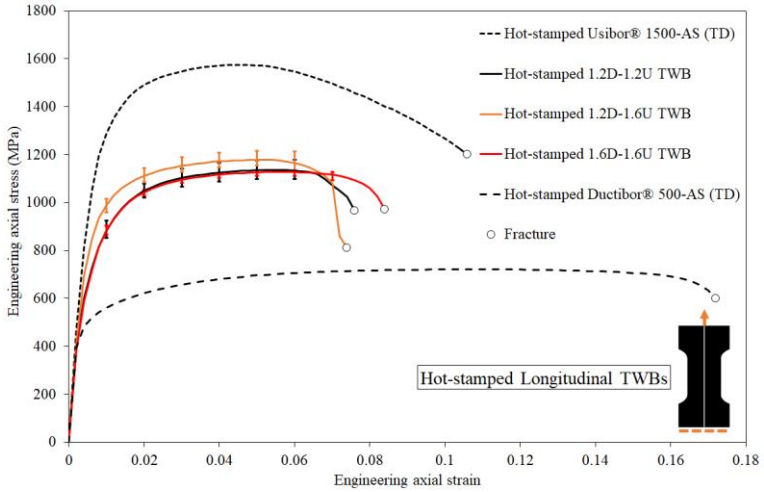

Figure 13: The engineering stress-strain curves of the tensile longitudinal TWBs and 1.2-mm-thick monolithic parent metals of Usibor® 1500-AS [201] and Ductibor® 500-AS. Note that the error bars correspond to the measured data variations.

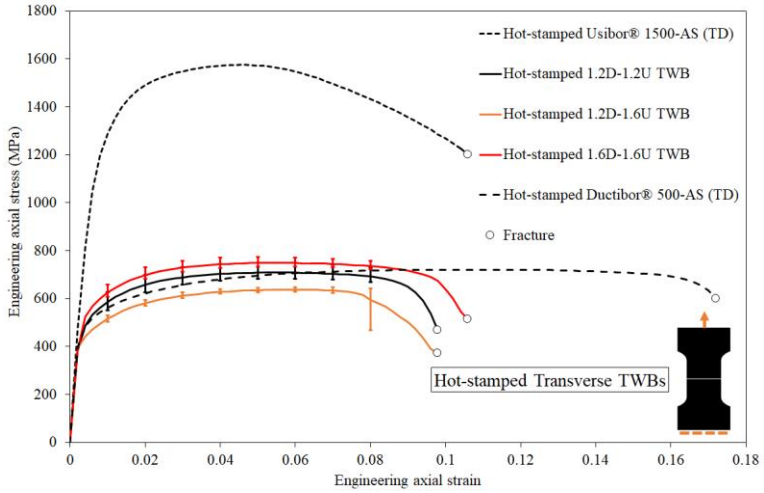

Figure 14: The engineering stress-strain curves of the tensile transverse TWBs and 1.2-mm-thick monolithic parent metals of Usibor® 1500-AS [201] and Ductibor® 500-AS. Note that the error bars correspond to the measured data variations.

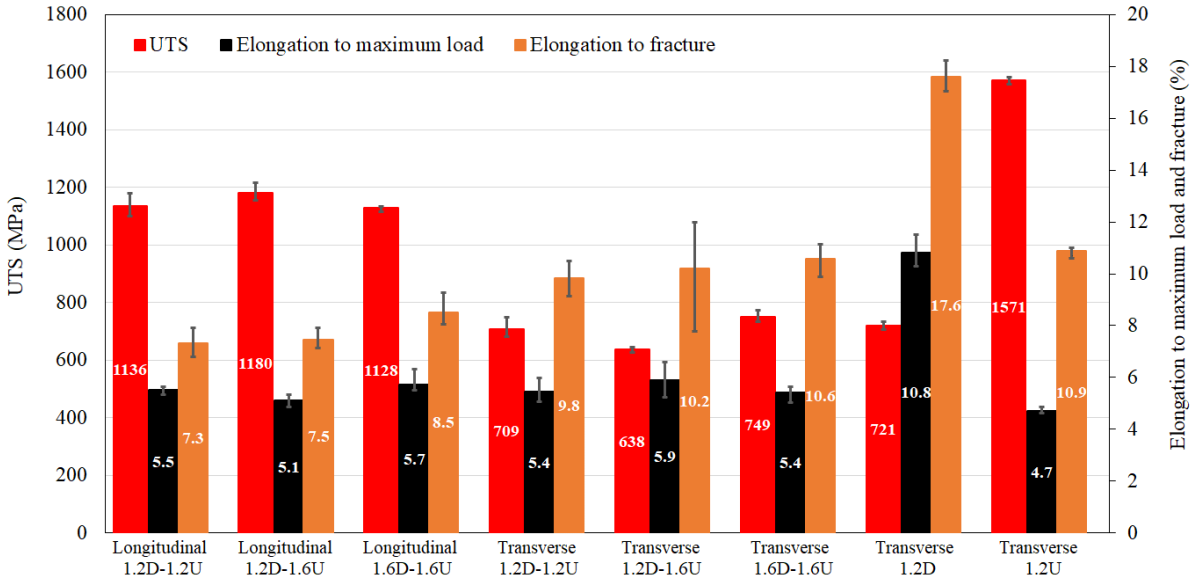

Figure 15: A comparison of the UTS, elongation to maximum load, and elongation to fracture of the various hot-stamped TWBs with those of the 1.2-mm-thick hot-stamped monolithic parent metals of Usibor® 1500-AS (U) [201] and Ductibor® 500-AS (D). Note that the error bars correspond to the measured data variations.

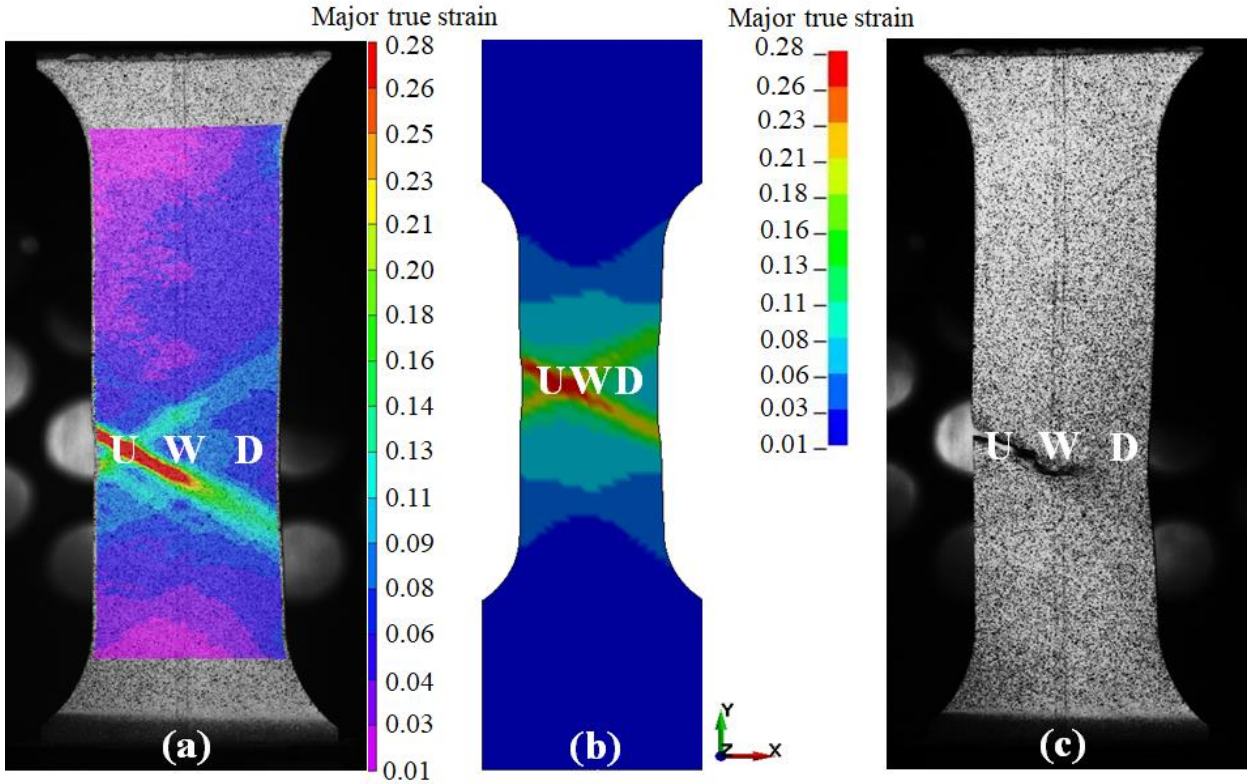

Figure 16: The a) measured and b) predicted major true strain distributions prior to fracture and c) the onset of fracture in the hot-stamped tensile longitudinal 1.2D-1.2U TWBs. Note that U, W, and D represent Usibor® 1500-AS, weld, and Ductibor® 500-AS, respectively, and the FE model prediction in (b), corresponding to the simulation with the weld region modelling, is discussed in Section 4.4.

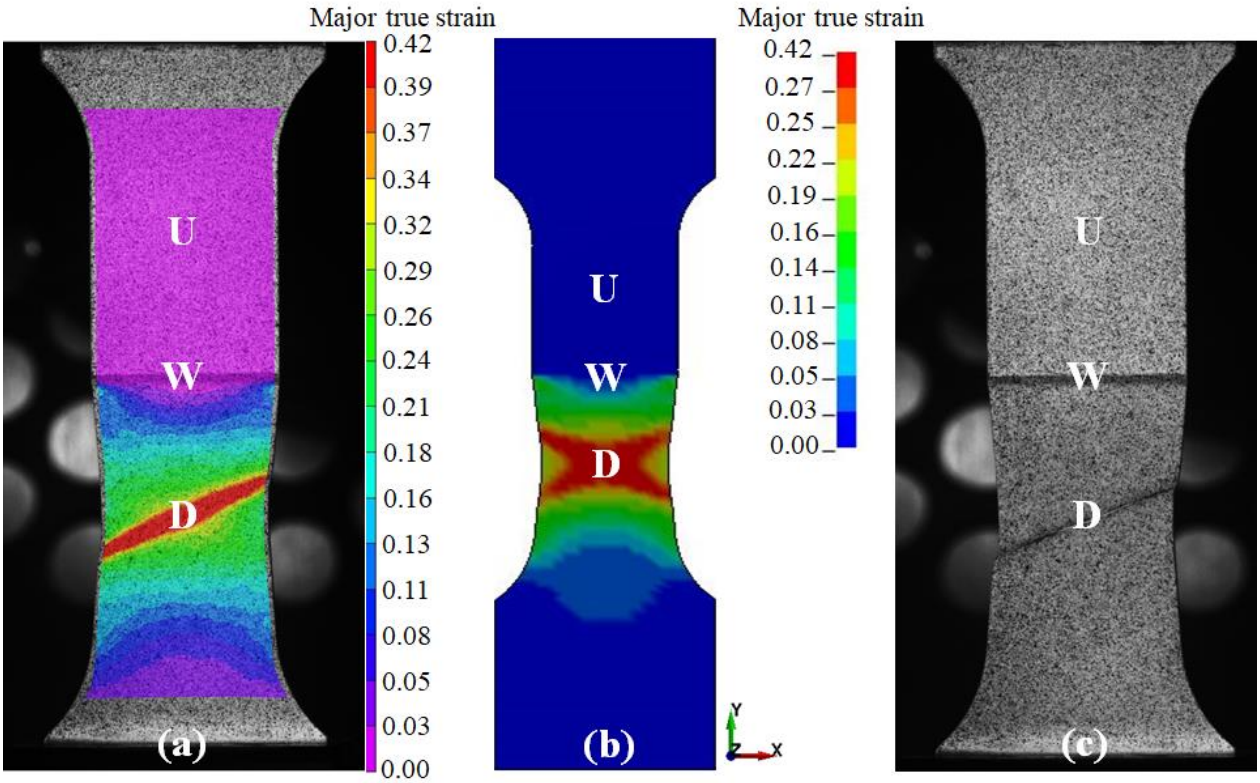

Figure 17: The a) measured and b) predicted major true strain distributions prior to fracture and c) the onset of fracture in the hot-stamped tensile transverse 1.2D-1.6U TWBs. Note that U, W, and D represent Usibor® 1500-AS, weld, and Ductibor® 500-AS, respectively, and the FE model prediction in (b), corresponding to the simulation with the weld region modelling, is discussed in Section 4.4.

Figure 18 shows the major true strain distributions of the longitudinal 1.2D-1.2U and transverse 1.2D-1.6U TWBs across the weld at several levels of total elongation (e_f), respectively. Since the other TWB specimens for each orientation exhibited similar responses, their results are not shown here for brevity. For the longitudinal TWBs, uniform distributions of major true strain were observed across the sample width until around 75% of the total elongation (e_f). This corresponds to the deformation state prior to reaching the UTS point, at which almost uniform elongation existed along the gauge length of the specimen. For higher levels of deformation, the strain was localized within the Usibor® 1500-AS side of the specimen and increased extensively until fracture initiation (Figure 16), with only mild increases in strain on the Ductibor® 500-AS side of the specimen. In fact, the deformation in the gauge sections of the longitudinally-loaded weldments was approximately uniform until maximum load (diffuse necking); thus, fracture was initiated in the more brittle Usibor® 1500-AS region.

In the transversely-loaded TWBs, plastic deformation was confined to the lower strength Ductibor® 500-AS side of the specimen, whereas the weld and Usibor® 1500-AS sheet remained largely elastic. At a deformation level corresponding to approximately 50% of the total elongation, strain localization was initiated within the Ductibor® 500-AS section, followed by final fracture (Figure 17). In the transversely-loaded TWBs, the transmitted load is constant across the parent metals and weld regions, thus localization and fracture are initiated in the weaker Ductibor® 500-AS region.

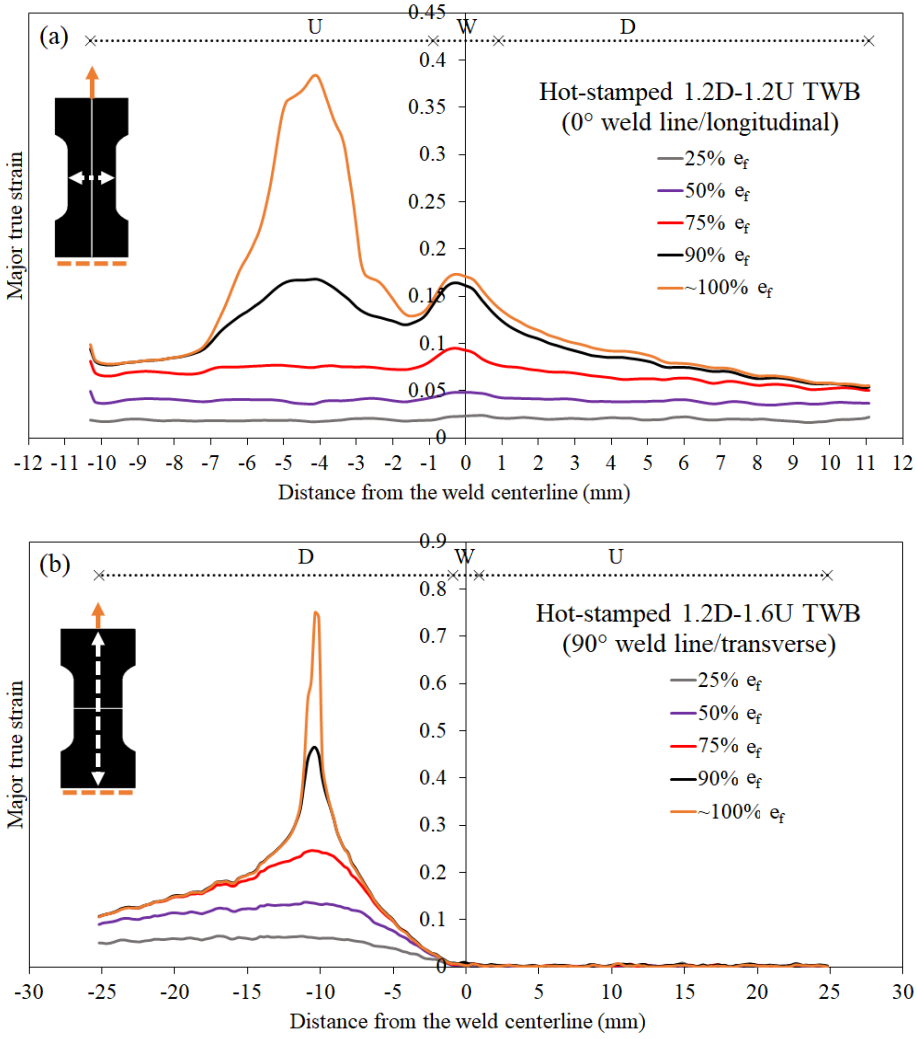

Figure 18: The major true strain distributions across the weld for the (a) 1.2-mm-thick mono-gauge longitudinal and (b) multi-gauge transverse TWB tensile samples at several levels of total elongation (e_f). Note that U, W, and D represent Usibor® 1500-AS, weld, and Ductibor® 500-AS, respectively.

4.2.2.2. Nakazima Dome Test Results

Figure 19 presents a comparison of the maximum punch displacements and equivalent fracture strains for the three TWB configurations and two parent metals in the Nakazima dome tests with the equibiaxial tension geometry. The multi-gauge TWB exhibited the highest punch displacement and fracture strain compared to the two mono-gauge TWBs. Taking into account that fracture initiation occurred in the Ductibor® 500-AS section of the TWB Nakazima dome specimens (Figure 20), the higher ductility of the multi-gauge TWB is attributed to the formation of a softer microstructure of Ductibor® 500-AS in such a TWB after hot stamping, as discussed in Section 4.2.1. The 1.6- and 1.2-mm-thick mono-gauge TWBs had similar fracture strains but different punch displacements. Compared to the 1.6-mm-thick monolithic parent metals, all TWB types fractured at lower punch depths.

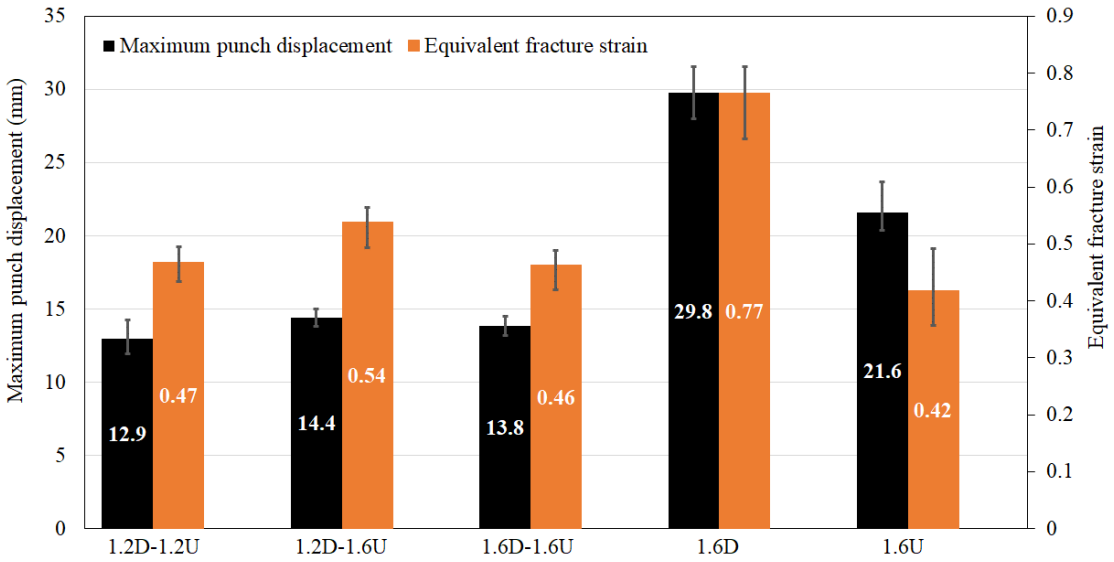

Figure 19: The average maximum punch displacements and equivalent fracture strains of the various hot-stamped TWBs in the Nakazima dome tests with the equibiaxial tension geometry in comparison with those of the 1.6-mm-thick hot-stamped monolithic parent metals of Usibor® 1500-AS (U) and Ductibor® 500-AS (D). Note that the error bars correspond to the measured data variations.

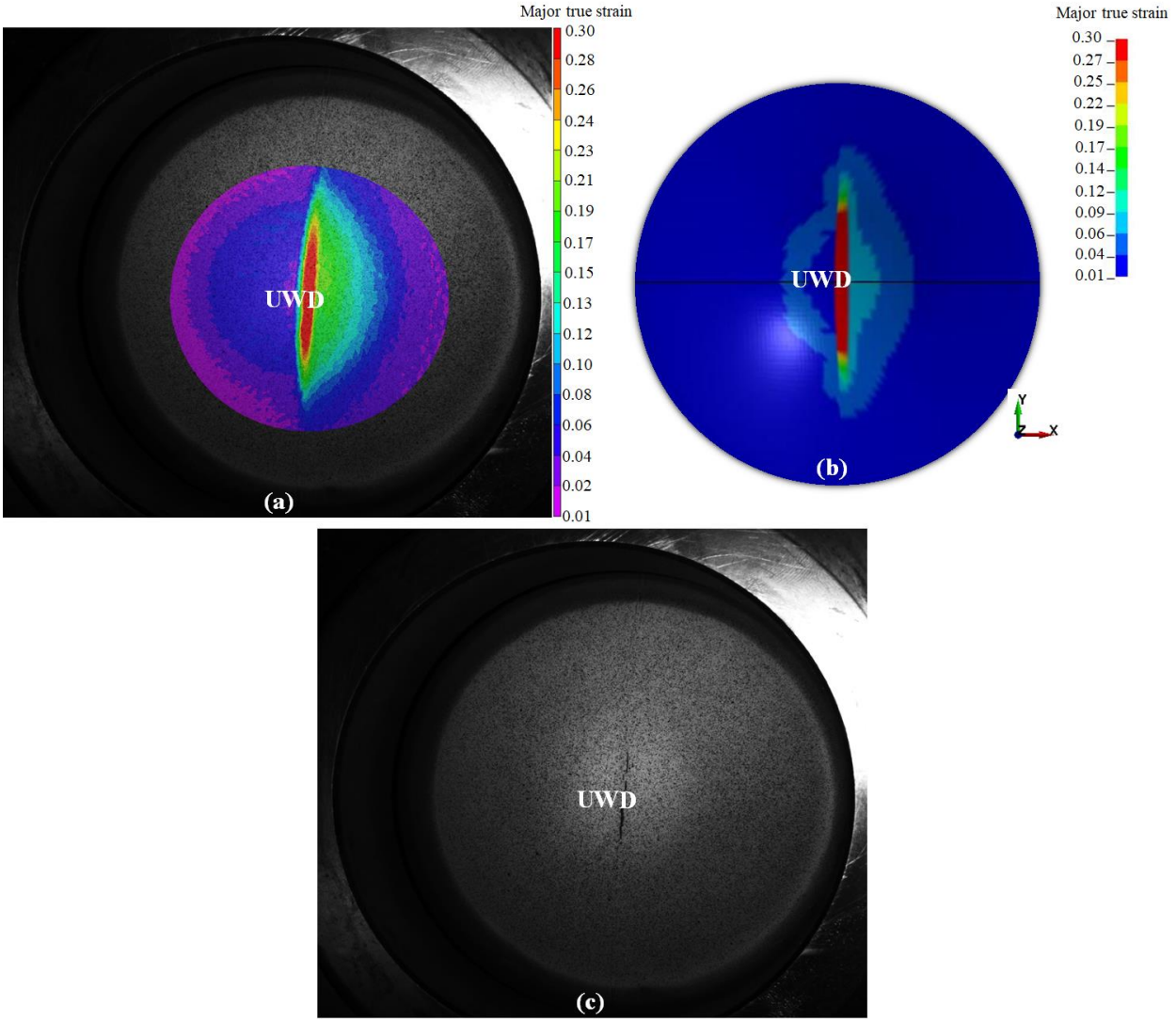

Figure 20: The a) measured and b) predicted major true strain distributions prior to fracture and c) the onset of fracture in the Nakazima dome 1.6D-1.6U TWBs with the equibiaxial tension geometry. Note that U, W, and D represent Usibor® 1500-AS, weld, and Ductibor® 500-AS, respectively, and the FE model prediction in (b), corresponding to the simulation with the weld region modelling, is discussed in Section 4.4.

The strain paths corresponding to the fracture locations of the three equibiaxial tension Nakazima dome TWB configurations are shown in Figure 21. At the onset of deformation, the minor true strain increased slightly because of the engagement of the hemispherical punch with the blanks and the consequent biaxial bending. After this point, the rate of changes in the minor true strain went to zero, and the subsequent deformation was under a plane-strain tension condition. Such a phenomenon was due to the constraint of the much stronger Usibor® 1500-AS sheet which effectively suppressed deformation along the weld line in the Ductibor® 500-AS side of the TWBs. As a result, fracture in the Ductibor® 500-AS sheet occurred under a plane-strain

tension condition, with its inherently-lower ductility. Due to the same reason, the dome heights (or maximum punch displacements) for the TWB samples were much lower than those for the monolithic sheet specimens (Figure 19), which experienced an almost equibiaxial stretching condition with the same specimen geometry. The similarity of the DIC-based equivalent fracture strains of the TWB equibiaxial tension Nakazima dome specimens (Figure 19) to those of the plane-strain tension Nakazima dome specimens of the hot-stamped monolithic Ductibor® 500-AS (Figure 9) also confirms the above discussion.

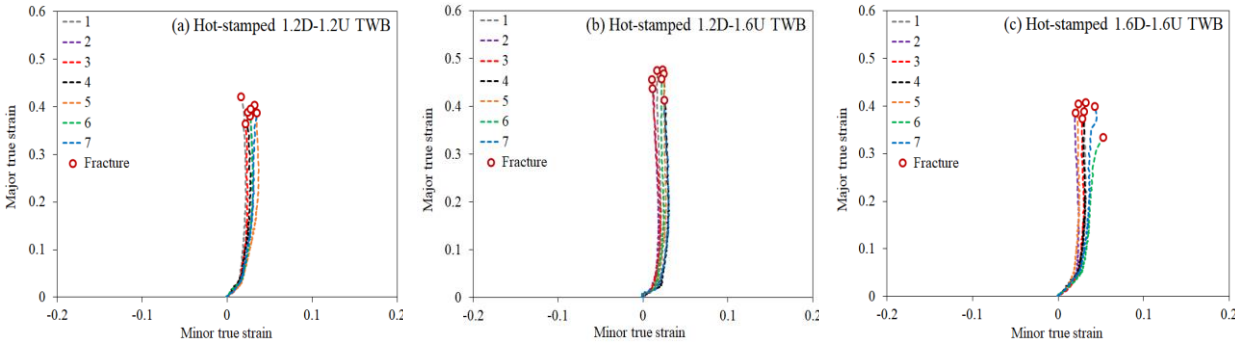

Figure 21: The strain paths corresponding to the fracture locations of the hot-stamped a) 1.2-mm-thick mono-gauge, b) multi-gauge, and c) 1.6-mm-thick mono-gauge TWBs during the equibiaxial tension Nakazima dome tests.

To further examine the development of the strain distributions within the TWB Nakazima dome samples, the major true strain distributions across the weld for the various TWBs at different levels of deformation are shown in Figure 22. It is evident that from the early stages of loading, the deformation was concentrated in the Ductibor® 500-AS side of the weldment, while the strain in the Usibor® 1500-AS parent metal and weld region remained quite low. Interestingly, the location of fracture in the 1.2D-1.6U TWBs was further from the weld, as compared to that in the mono-gauge TWB samples. This behavior is attributed to the induced bending at the weld in the thinner gauge due to the offset of the mid-planes of the parent metals.

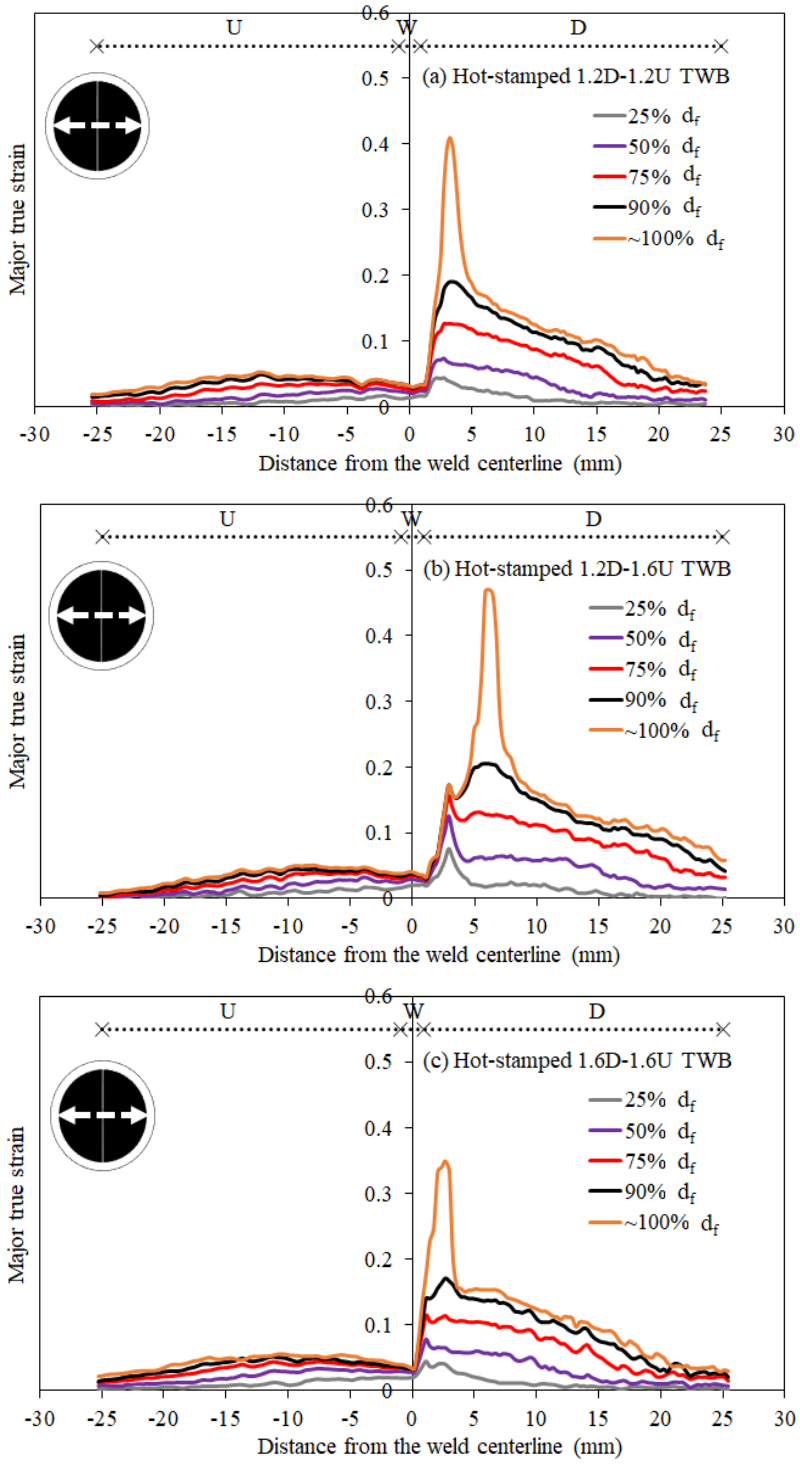

Figure 22: The distribution of major true strain across the weld in the equibiaxial tension Nakazima dome samples of the hot-stamped a) 1.2-mm-thick mono-gauge, b) multi-gauge, and c) 1.6-mm-thick mono-gauge TWBs at several levels of the total (fracture) punch depth (d_f). Note that U, W, and D represent Usibor® 1500-AS, weld, and Ductibor® 500-AS, respectively.

4.2.2.3. V-Bend Test Results

Figure 23 presents a summary of the results of the V-bend tests on the different hot-stamped TWBs as well as the 1.6-mm-thick monolithic parent metals based on the VDA 238-100 standard [200]. The V-bend testing on the samples with the 0° weld-line orientation relative to the punch bend axis resulted in fracture within the weld (Figure 24b). Among the 0° TWB samples, the multi-gauge TWB had the lowest bend angle and fracture strain. The reason is attributed to the stress concentration at the weld and, consequently, the earlier fracture. The bend angle and fracture strain increased as the thickness increased in the case of the 0° mono-gauge TWBs. However, the 45° and 90° specimens of the different TWBs fractured within the Usibor® 1500-AS parent metal (Figures 25b and 26b, respectively). As a result, the fracture strains and bend angles were very similar for all of these TWBs. The 45° and 90° 1.2-mm-thick TWBs had the highest bend angles among all of the TWBs. As can be seen in Figure 23, a comparison of the results of the TWB and parent-metal V-bend tests reveals that the bend angles and equivalent fracture strains for the TWBs that fractured within Usibor® 1500-AS were comparable to those of the monolithic Usibor® 1500-AS sheet. However, all of the TWBs exhibited the lower ductility with respect to the monolithic Ductibor® 500-AS sheet. It should be noted that for most of the samples, cracking was observed slightly after or before the VDA threshold.

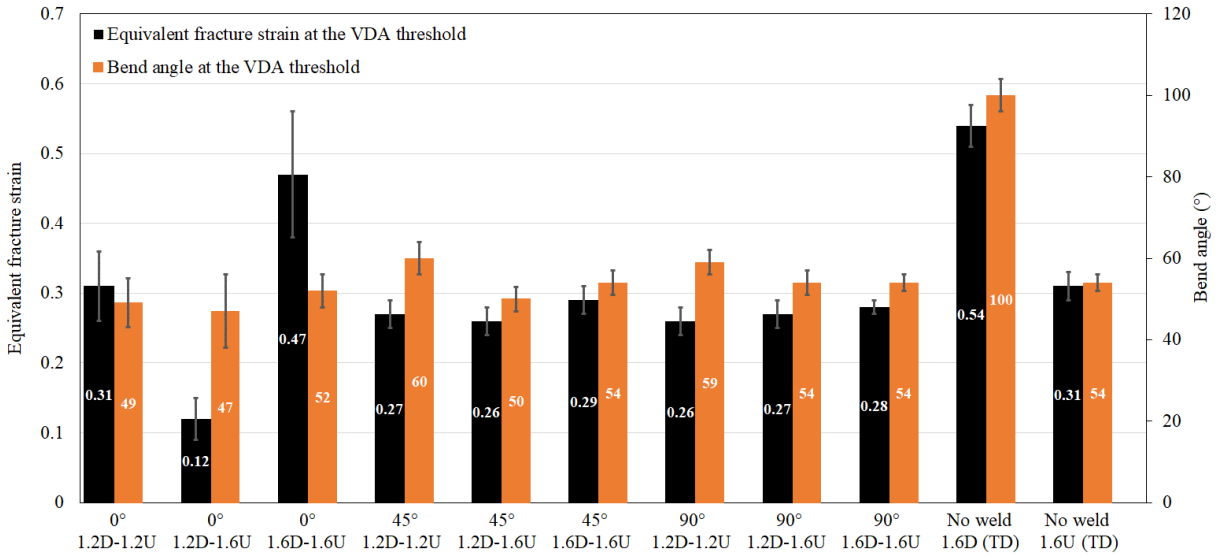

Figure 23: A summary of the results of the V-bend tests on the various hot-stamped TWBs compared to those of the hot-stamped 1.6-mm-thick monolithic parent metals of Usibor® 1500-AS (U) and Ductibor® 500-AS (D). Note that the error bars correspond to the standard deviations of the measured data.

Figures 24-26 show major true strain distributions at the VDA points in the various V-bend specimens. It is observed that the strain distribution in the 0° V-bend sample (Figure 24a) was not symmetric around the punch radius, contrary to that in either of the 45° or 90° specimens (Figures 24a and 25a, respectively). This behavior is attributed to the imbalance of the strength across the weld in the 0° specimens, which led to the slip of the specimens over the punch tip towards the higher strength region (Usibor® 1500-AS). It is interesting that the Ductibor® 500-AS region in the 0° V-bend specimens experienced the highest strains (Figure 24a), but fracture occurred in the weld (Figure 24b), which had the intermediate strains (Figure 24a).

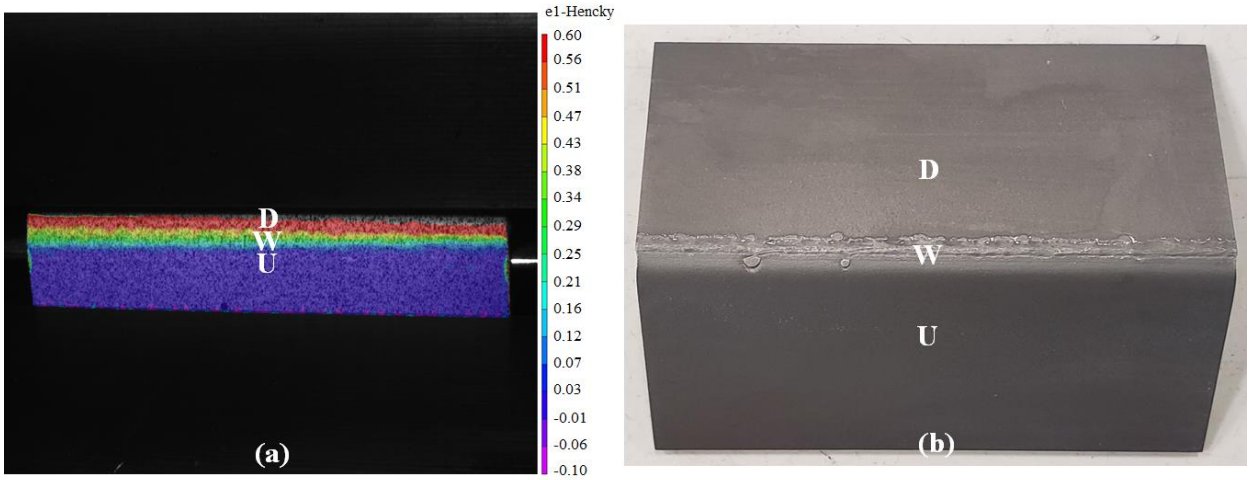

Figure 24: a) The distribution of major true strain at the VDA point and b) a fractured specimen of the 1.6D-1.6U TWBs in the 0° V-bend test. Note that U, W, and D represent Usibor® 1500-AS, weld, and Ductibor® 500-AS, respectively.

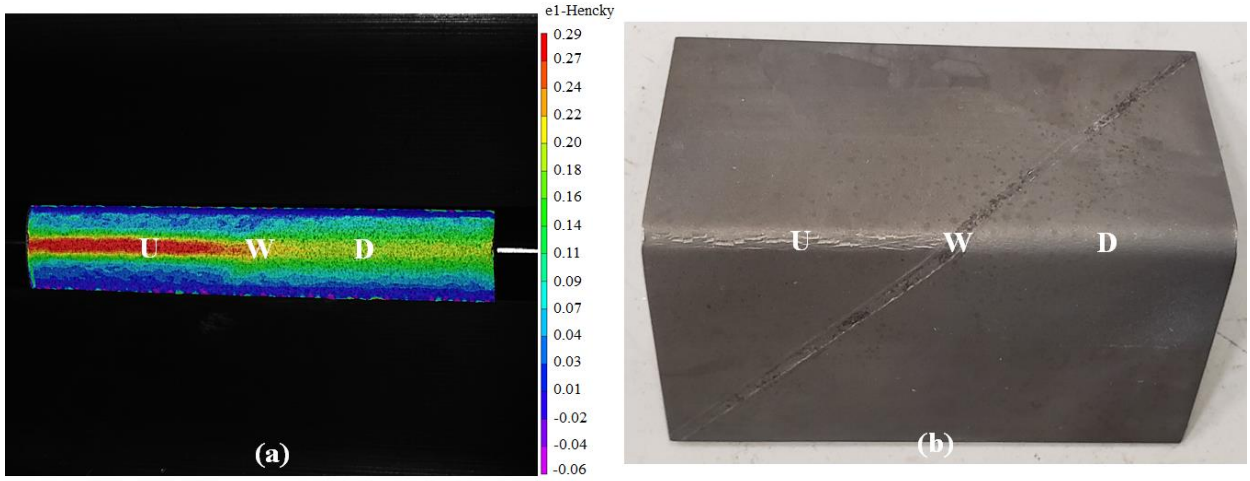

Figure 25: a) The distribution of major true strain at the VDA point and b) a fractured specimen of the 1.2D-1.2U TWBs in the 45° V-bend test. Note that U, W, and D represent Usibor® 1500-AS, weld, and Ductibor® 500-AS, respectively.

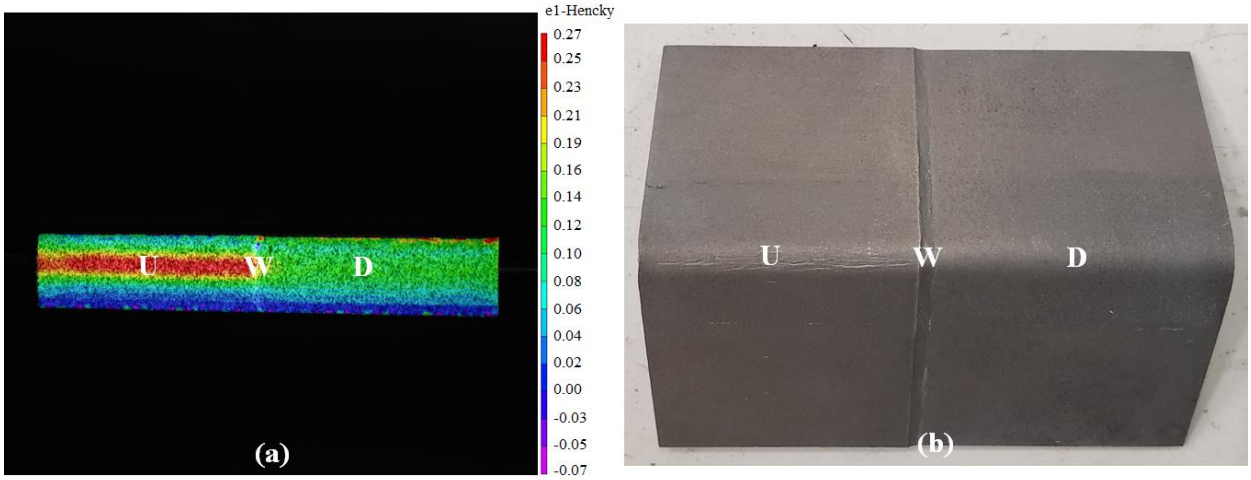

Figure 26: a) The distribution of major true strain at the VDA point and b) a fractured specimen of the 1.2D-1.6U TWBs in the 90° V-bend test. Note that U, W, and D represent Usibor® 1500-AS, weld, and Ductibor® 500-AS, respectively.

Figure 27 illustrates the strain paths experienced by the TWBs for each weld orientation during the V-bend tests. It is evident that there was an almost-completely plane-strain condition at the fracture points throughout the tests for the various weld orientations of the TWBs. The strain histories of the TWBs not shown in Figure 27 were similar to those plotted and are omitted for the sake of brevity. Compared to the strain paths of the TWB Nakazima dome specimens (Figure 21), for which an almost plane-strain condition was also dominant at fracture locations throughout the testing, the strain paths of the TWB V-bend samples are approximately linear. The early deviation from the plane-strain condition in the Nakazima dome samples is due to the initial bending during the punch engagement with the specimens.

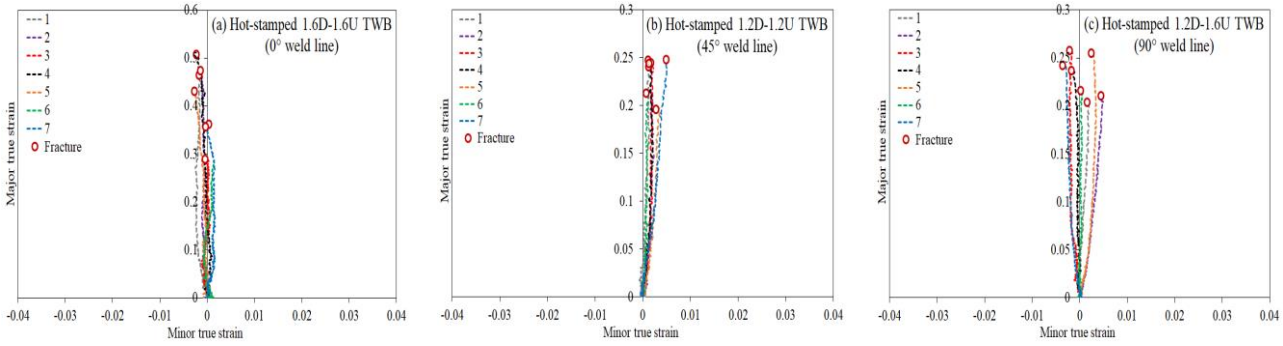

Figure 27: The strain paths of the a) 1.6-mm-thick mono-gauge, b) 1.2-mm-thick mono-gauge, and c) multi-gauge TWBs with the 0°, 45°, and 90° weld orientations during the V-bend tests, respectively.

It is noted that more details about the characterization work on the mechanical response of the TWBs and measured fracture properties, including minor strain distributions in the tensile tests and punch load at the VDA point in the V-bend tests, can be found in Appendix D.

4.3. Task 3: Microstructure-based Modelling of the Mechanical Response of Parent Metals

To model the flow and fracture behavior of Usibor® 1500-AS and Ductibor® 500-AS for a range of as-quenched microstructures and stress states, a coupled micromechanical-phenomenological strategy was developed. In this approach, the flow response of the multi-phase steels was calculated using mean-field homogenization (MFH) techniques, and their fracture response was predicted using the GISSMO damage model defined at the micro level within each micro-constituent. The following sections present the foundations and predictions of the proposed numerical strategy. It is noted that the as-quenched microstructures of Usibor® 1500-AS the mechanical response of which was modelled in this work were those developed and characterized by ten Kortenaar [89]. These include approximately fully-martensitic (100%M), 60% martensitic plus 40% bainitic (60%M+40%B), and fully-bainitic (100%B) microstructures, produced *via* quench-hardening heat treatments with cooling rates of 50 °C/s (oil-cooled), 24 °C/s (forced air-cooled), and 14 °C/s (air-cooled), respectively. The numerical work on Ductibor® 500-AS was performed on the as-quenched microstructures produced as part of the current research, corresponding to 5 °C/s (air-cooled), 365 °C/s (die-cooled), and 1890 °C/s (water-cooled) cooling rates (See Section 4.1.1 and Table 3).

4.3.1. Modelling of Constitutive Behavior

To model the constitutive (flow) behavior of the studied microstructures of Ductibor® 500-AS, the true stress-strain curves obtained by the uniaxial tension tests were first extrapolated beyond the UTS point using the shear-conversion methodology proposed by Rahmaan *et al.* [197]. Given this approach, the plastic work per unit volume in the tensile and shear tests was calculated up to the UTS point using the normal (tensile) and shear stresses (σ_n and τ) and plastic strains (ε_n^p and γ^p) for each material condition. Then the averaged shear-to-normal stress ratios were obtained for the same amounts of the plastic work per unit volume in the tensile and shear tests and assumed to remain constant beyond the UTS point. Finally, the shear stress-plastic strain data

was converted to the corresponding tensile (equivalent) stresses (σ_{eq}) and plastic strains (ε_{eq}^{p}) using the averaged shear-to-normal stress ratios and plastic work equivalency (Equation (9) [202]), respectively.

$$\varepsilon_{eq}^{p} = \int \left(\frac{\tau}{\sigma_n} \right) d\gamma^{p} = \left(\frac{\tau}{\sigma_n} \right) \gamma^{p} = 2 \left(\frac{\tau}{\sigma_n} \right) sinh\left(\varepsilon_1^{p} \right) \tag{9}$$

In Equation (9), ε_1^{p} is the major principal plastic strain measured during the shear test. It should be noted that this equation is the general form of the work-conjugate equivalent plastic strain given the rotation of the principal axes in simple shear loading [202]. The converted shear data was further fit to a modified Hockett-Sherby model (Equation (10)) [203] to extend the flow curves for even larger strains.

$$\bar{\sigma} = b - (b - a) \exp(-c(\bar{\varepsilon}^{p})^{d}) + e\sqrt{\bar{\varepsilon}^{p}} \tag{10}$$

In Equation (10), a to e are calibration parameters that were identified in a constrained least-squares minimization using the MATLAB® software.

Figure 28 illustrates the tensile, converted shear, and modified Hockett-Sherby flow curves of the different as-quenched conditions of Ductibor® 500-AS. It is apparent that for all of the material conditions, the converted shear data matches the experimental data until UTS, and the flow curves extrapolated based on the modified Hockett-Sherby model are in good agreement with both measured tensile and converted shear data.

More details about the constitutive modelling of the flow response of the studied material conditions of Ductibor® 500-AS, including calculated shear-to-normal stress ratios and calibration parameters of the modified Hockett-Sherby hardening law, can be found in Appendix B. It should be noted that for Usibor® 1500-AS, the tensile flow curves of the studied as-quenched conditions were already extrapolated by ten Kortenaar [89] using an inverse-modelling approach beyond the UTS point to large strains (See Appendix A). The modelling of these extrapolated flow curves was conducted in the present research.

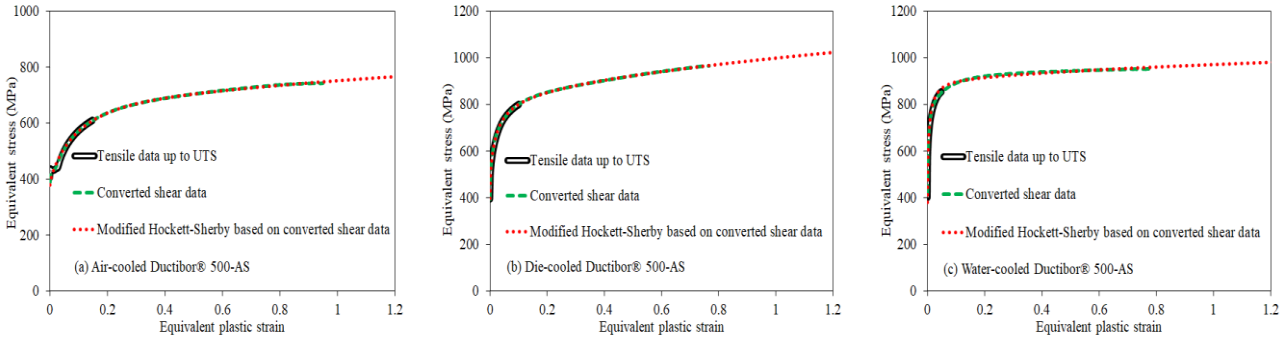

Figure 28: The tensile, converted shear, and modified Hockett-Sherby flow curves of the different as-quenched conditions of Ductibor® 500-AS; (a) air-, (b) die-, and (c) water-cooled conditions.

To predict the flow response of the as-quenched microstructures of both Usibor® 1500-AS and Ductibor® 500-AS, mean-field homogenization (MFH) modelling was applied. For this purpose, the microstructures were idealized as two-phase composites with the softer constituent phase, *i.e.* bainite in Usibor® 1500-AS and ferrite in Ductibor® 500-AS, as an isotropic matrix surrounding the harder martensitic spheroids, treated as randomly distributed inclusions in the matrix. Such representative microstructures were consistent with the adopted assumption of the isotropic mechanical behavior for both steels in this numerical study. In addition, the tempered martensite/bainite (TM/B) phases present as minor phases ($\leq \sim 12$ %v, Table 3) in the ferritic-martensitic microstructures of Ductibor® 500-AS were treated as martensite in the numerical modelling. Such an assumption was considered reasonable for the retention of a two-phase numerical treatment since the mechanical behavior of TM/B is closer to that of the martensitic phase than the ferrite phase. Therefore, the air-, die-, and water-cooled microstructures of Ductibor® 500-AS were approximated to be 96% ferritic plus 4% martensitic (~96%F+4%M), 57% ferritic plus 43% martensitic (~57%F+43M), and 10% ferritic plus 90% martensitic (~10%F+90%M), respectively. The hardening behavior of the bainitic-martensitic and ferritic-martensitic microstructures of Usibor® 1500-AS and Ductibor® 500-AS was calculated using two developed MFH schemes, referred to as the Samadian-Butcher-Worswick 1 (SBW1) and interpolative Samadian-Butcher-Worswick 1 (INSBW1) schemes, respectively. The developed MFH models are iterative models in which the mechanical properties of the equivalent homogeneous material (EHM) are updated as the volume fractions of the constituent phases vary in the microstructure. These models relate the micro strain fields of the matrix and inclusions using the self-consistent [102,204] and/or inverse self-consistent (obtained by the permutation of the matrix and inclusion properties) strain concentration tensors and account for the self-interactions

of inclusions and the influence of the volume fractions of the phases. The strain concentration tensors of inclusions ($\mathrm{A}^{(i)}$), which correlate the micro strain field in inclusions ($\langle\varepsilon\rangle^{(i)}$) with the applied macroscopic strain $\langle\varepsilon\rangle$, in these MFH schemes are expressed as below:

$$\xrightarrow{\langle\varepsilon\rangle^{(i)}=\mathrm{A}^{SBW1(i)}:\langle\varepsilon\rangle} \mathrm{A}^{SBW1(i)}=[\mathrm{I}^{(4)}+f_{(m)}\bar{\mathrm{S}}:[\bar{\mathrm{L}}]^{-1}:(\mathrm{L}^{(i)}-\bar{\mathrm{L}})]^{-1} \tag{11}$$

$$\xrightarrow{\langle\varepsilon\rangle^{(i)}=\mathrm{A}^{INSBW1(i)}:\langle\varepsilon\rangle} \mathrm{A}^{INSBW1(i)}=(1-\varphi)\mathrm{A}^{SBW1(i)}+\varphi\mathrm{A}^{ISBW1(i)} \tag{12}$$

in which:

$$\xrightarrow{\langle\varepsilon\rangle^{(i)}=\mathrm{A}^{ISBW1(i)}:\langle\varepsilon\rangle} \mathrm{A}^{ISBW1(i)}=\frac{\mathrm{I}^{(4)}-f_{(m)}[\mathrm{I}^{(4)}+f_{(i)}\bar{\mathrm{S}}:[\bar{\mathrm{L}}]^{-1}:(\mathrm{L}^{(m)}-\bar{\mathrm{L}})]^{-1}}{f_{(i)}} \tag{13}$$

In Equations (11)-(13), $\mathrm{A}^{INSBW1(i)}$, $\mathrm{A}^{SBW1(i)}$, and $\mathrm{A}^{ISBW1(i)}$ are the fourth-order strain concentration tensors of the interpolative, direct, and inverse SBW1 schemes for inclusions; φ and $\mathrm{I}^{(4)}$ are an interpolation function and the fourth-order identity tensor; $f_{(m)}$ and $f_{(i)}$ are the volume fractions of the matrix and inclusions; $\mathrm{L}^{(m)}$, $\mathrm{L}^{(i)}$, and $\bar{\mathrm{L}}$ are the fourth-order tangent moduli of the matrix, inclusions, and composite; and $\bar{\mathrm{S}}$ is Eshelby's tensor [100] in terms of the composite properties and inclusion geometry, respectively. The interpolation function (φ) used in the INSBW1 model was the one developed by Lielens *et al.* (Equation (14)) [107]:

$$\varphi=\frac{1}{2}f_{(i)}(1+f_{(i)}) \tag{14}$$

The strain concentration tensor of the matrix ($\mathrm{A}^{(m)}$), which relates the micro strain field in the matrix ($\langle\varepsilon\rangle^{(m)}$) to the applied macroscopic strain, can be obtained based on the fact that the volume average of the strain concentration tensors of the constituent phases equals unity, *i.e.* $f_{(i)}\mathrm{A}^{(i)}+f_{(m)}\mathrm{A}^{(m)}=\mathrm{I}^{(4)}$ [205]. The step-by-step development of the proposed MFH models and evaluation of their predictive performance for the elastic and elastoplastic behavior of multi-phase materials are detailed in Appendix E.

In the MFH modelling for the bainitic-martensitic microstructures of the as-quenched Usibor® 1500-AS, the flow behavior of the individual phases of bainite and martensite in the mixed microstructures was assumed to be the same as that of their single-phase microstructures, *i.e.* 100%B and 100%M, respectively. The effect of carbon partitioning on the mechanical response of bainite and martensite was neglected. This assumption was based on the fact that bainite and martensite are both considered constituent phases with high carbon concentrations and no specific limitations for carbon solubility (contrary to ferrite [129]). However, in the case of the ferritic-martensitic microstructures of the as-quenched Ductibor® 500-AS, the solubility of carbon in ferrite is very low [126,128,129]. Consequently, the strength of martensite is strongly influenced by variations in its volume fraction due to the carbon partitioning phenomenon, in which carbon is ejected from ferrite to austenite during the ferritic transformation. To capture this effect, the flow behavior of the ferritic and martensitic phases within the mixed-phase microstructures of Ductibor® 500-AS was modelled using the dislocation-based strain hardening model developed by Rodriguez and Gutierrez (Equation (15)) [132]. As noted in Section 2.6.1.2, this model considers the lattice-friction (Peierls stress) and alloying-element effects as well as dislocation generation and annihilation during the plastic deformation in addition to carbon partitioning between phases.

$$\sigma(\text{MPa}) = \sigma_0 + \Delta\sigma + \alpha M \mu \sqrt{b} \sqrt{\frac{1-\exp(-Mk\bar{\varepsilon}^p)}{kL}} \tag{15}$$

where

$$\sigma_0 = 77 + 750(\%P) + 60(\%Si) + 80(\%Cu) + 45(\%Ni) + 60(\%Cr) + 11(\%Mo) + 5000(\%N_{ss}) \tag{16}$$

$$\Delta\sigma = 5000(\%C_{ss}^{F}) \qquad \text{for ferrite} \tag{17}$$

$$\Delta\sigma = 3065(\%C_{ss}^{M}) - 161 \qquad \text{for martensite} \tag{18}$$

In Equation (15), σ_0 represents the lattice friction and alloying element effects in the solid solution. In this work, the distribution of the alloying elements in the micro-constituents was considered to be uniform and similar to that in the steel. $\Delta\sigma$ takes into account the effects of carbon in the solid solution or precipitations. Similar to the work by Pierman *et al.* [129], the

carbon content in ferrite was ignored ($\%C_{ss}^{F} \approx 0$) according to its very low solubility in this phase, and the carbon content in martensite was calculated using the weight balance of carbon in the steel in terms of the steel carbon weight percentage ($\%C_{ss}^{steel}$) and martensite volume fraction (V_M) in each microstructure (Equation (19)).

$$\%C_{ss}^{M} = \frac{\%C_{ss}^{steel} - V_F.\%C_{ss}^{F}}{V_M} \approx \frac{\%C_{ss}^{steel}}{V_M} \tag{19}$$

α is the dislocation strengthening constant that varies between 0.2 and 0.5 depending on the dislocation density [206]. In this work, a value of 0.24 was considered for α. M is the Taylor factor with a value of ~ 3 for bcc and fcc materials that relates the resolved shear stress in a single crystal to the normal flow stress in the polycrystal ($\sigma = M\tau$) [206,207]. μ, b, L, and k are the shear modulus (80,000 MPa), Burgers vector (2.5×10^{-10} m), and dislocation mean free path and recovery rate, respectively. For the ferritic phase, L equals the average ferrite grain size (d_F), which has a relationship with k through the following equation [63,131]:

$$k_F = \frac{10^{-5}}{d_F} \tag{20}$$

For the martensitic phase, similar to the work by Rodriguez *et al.* [132] and Sodjit *et al.* [130], L and k were considered as fitting parameters such that the predicted hardening curves for the air-, die-, and water-cooled conditions based on the MFH modelling have the least deviations with respect to the experimental converted shear hardening data (Figure 28). It is noted that the values of L and k for martensite in each microstructure were determined using an optimization code based on a least-squares problem written in FORTRAN 90.

The first-order secant-based linearization approach [111], which is appropriate for proportionally monotonic loading conditions, together with the algorithmic tangent moduli of the constituent phases, was applied in the plastic deformation region for the MFH modelling of the flow response of the as-quenched microstructures of both steels. In this method, the stress and strain updates in each phase are performed using the secant modulus that relates total strain to total stress within the constituent.

Therefore, given applied displacement boundary conditions, the strain in the constituent phases of the bainitic-martensitic and ferritic-martensitic microstructures of Usibor® 1500-AS and Ductibor® 500-AS, respectively, was calculated using the MFH models of SBW1 and INSBW1, respectively. Then the corresponding stress within each phase was integrated using the von Mises yield criterion and hardening response of the individual phases through the convex-cutting-plane (CCP) algorithm [208] with an imposed constraint of plane-stress loading for the steels.

Figure 29 shows a comparison between the predicted and extrapolated (experiment-based) flow curves of the multi-phase microstructures of Usibor® 1500-AS and Ductibor® 500-AS. Also plotted are the extrapolated flow curves of the single-phase microstructures of Usibor® 1500-AS (100%B and 100%M), acquired by ten Kortenaar [89]. It is observed that there is good agreement between the predictions by the MFH models and experiment-based flow curves for both steels. These predictions can be improved if the carbon-partitioning effects on the hardening response of bainite and martensite in Usibor® 1500-AS and back stresses created by GNDs within ferrite in Ductibor® 500-AS are taken into account.

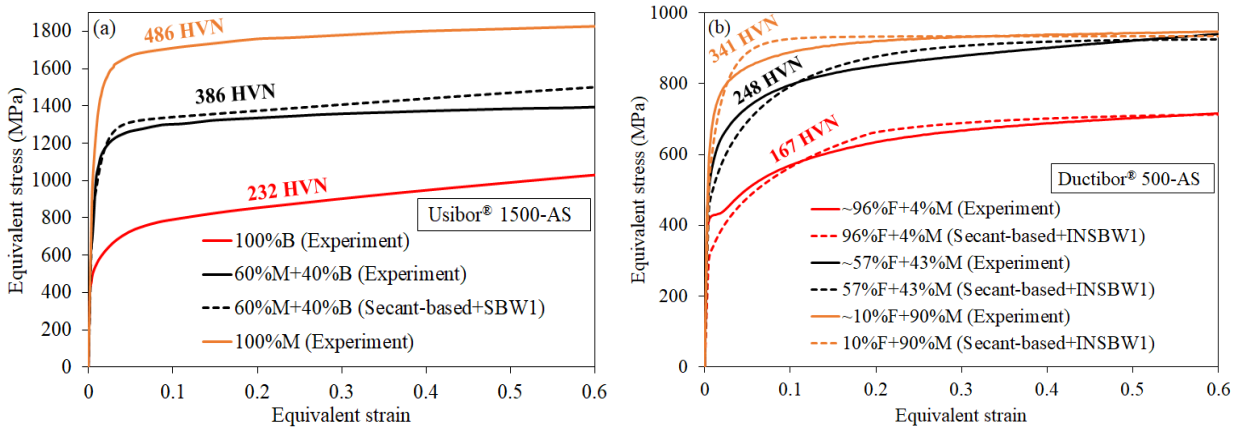

Figure 29: The predicted and extrapolated (experiment-based) flow curves of the multi-phase microstructures of (a) Usibor® 1500-AS and (b) Ductibor® 500-AS based on the MFH models of SBW1 and INSBW1, respectively, using the secant-based linearization method. Note that the extrapolated flow curves of the single-phase microstructures of Usibor® 1500-AS (100%B and 100%M), acquired by ten Kortenaar [89], are also plotted for the sake of comparison.

An important application of the MFH modelling developed in this work is to predict the changes in the flow response of hot-stamped products with the final microstructure due to intended or unintended variations in cooling rates during the hot-stamping processes. Such changes in cooling rates can be due to natural variations in the local temperature and contact pressure that occur within the tooling and transients associated with the startup and shutdown of production

lines during the hot-stamping process. This case is expected for both Usibor® 1500-AS and Ductibor® 500-AS. Moreover, the cooling-rate variations can be introduced by design in tailored hot-stamping processes, such as in-die heating, in order to impart graded mechanical properties to final components. Such a case is more applicable to Usibor® 1500-AS. In order to predict the corresponding variations in material properties, the hardening curves of the bainitic-martensitic and ferritic-martensitic microstructures of Usibor® 1500-AS and Ductibor® 500-AS, respectively, for a range of constituent-phase volume fractions were predicted based on the MFH models through the secant-based linearization method (Figure 30). As seen in Figure 30, the larger martensite content corresponded to the higher strength level for both steels. Such predictions can reduce time-consuming and expensive experiments for characterizing the hardening response of different microstructures formed in various regions of hot-stamped components and improve the predictability of the crash simulations of such products.

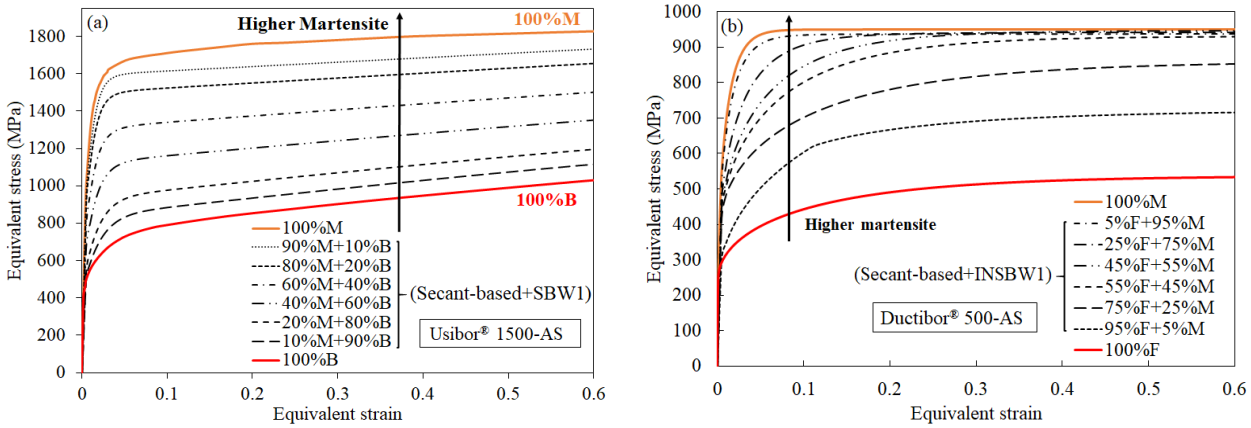

Figure 30: The predicted stress-strain curves of the (a) bainitic-martensitic and (b) ferritic-martensitic microstructures of Usibor® 1500-AS and Ductibor® 500-AS for a range of micro-constituent volume fractions based on the SBW1 and INSBW1 models through secant-based linearization method, respectively.

Figure 31 shows the calculated hardening curves of the ferritic and martensitic phases for the range of the ferritic-martensitic microstructures of Ductibor® 500-AS that was shown in Figure 30b. It is evident that as the martensite volume fraction increased, the predicted martensite strength decreased, while the predicted ferrite strength increased. Such predictions are consistent with the reported physical phenomena that occur within ferritic-martensitic microstructures. As the martensite content increases, a higher number of geometrically-necessary dislocations (GNDs) is generated within the ferritic grains [125,126,129,209,210], contributing to both isotropic and kinematic hardening (as discussed in Section 2.6.1.2). Moreover, the ferrite grain size tends to

decrease [128,129]. On the other hand, the concentration of carbon in martensite decreases [211]. Therefore, with an increased volume fraction of martensite, ferrite is strengthened, while martensite is weakened.

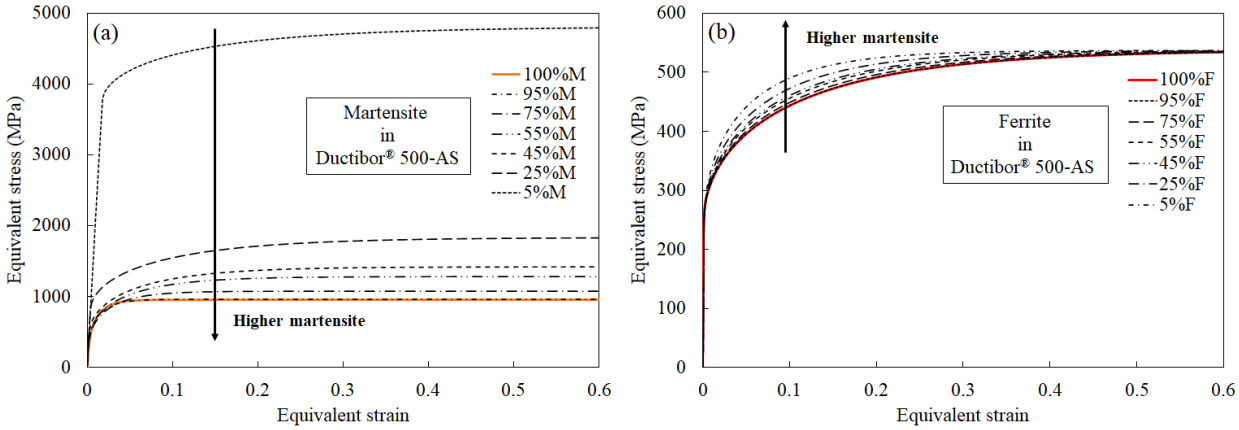

Figure 31: The calculated stress-strain curves of ferrite and martensite in the various ferritic-martensitic microstructures of Ductibor® 500-AS for different micro-constituent volume fractions based on the dislocation-based strain hardening model.

More details about the MFH modelling of the flow response of the multi-phase microstructures of Usibor® 1500-AS and Ductibor® 500-AS as well as predictions for the stress and strain partitioning between the constituent phases and the micro *versus* macro stress states under different loading conditions can be found in Appendices A and C.

4.3.2. Modelling of Fracture Response

To predict fracture in the bainitic-martensitic and ferritic-martensitic microstructures of Usibor® 1500-AS and Ductibor® 500-AS, respectively, damage accumulation was calculated individually within each phase during the MFH integration of the constitutive response. In this regard, the GISSMO damage counter ($D^{(r)}$) [177], introduced in Section 2.6.2.3, was tracked for each constituent phase (r) using Equation (21):

$$D^{(r)} = \int dD^{(r)} = \int d\left[\left(\frac{\bar{\varepsilon}_p^{(r)}}{\bar{\varepsilon}_f^{(r)}}\right)^{n^{(r)}}\right] = \int_{\bar{\varepsilon}^{p(r)}} \frac{n^{(r)}}{\bar{\varepsilon}_f^{(r)}} \left(\frac{\bar{\varepsilon}_p^{(r)}}{\bar{\varepsilon}_f^{(r)}}\right)^{n^{(r)}-1} d\bar{\varepsilon}_p^{(r)} \tag{21}$$

where $\bar{\varepsilon}_p^{(r)}$, $\bar{\varepsilon}_f^{(r)}$, and $n^{(r)}$ are the equivalent plastic strain, equivalent fracture strain corresponding to the current stress state, and damage exponent all for the constituent phase of r, respectively. The equivalent fracture strain of the r micro-constituent at each deformation step

was taken from the fracture *locus* of the steel with a microstructure completely comprised of the same constituent phase (*i.e.* 100% r). In fact, the fracture *loci* of the single-phase microstructures of Usibor® 1500-AS (*i.e.* 100%B and 100%M) and Ductibor® 500-AS (*i.e.* 100%F and 100%M) were considered to be the bounds of fracture-strain limits for the corresponding constituent phases in the mixed-phase microstructures of the steels.

For Usibor® 1500-AS, the Bai-Wierzbicki fracture *loci* [180] for the 100%B and 100%M microstructures, as fracture curves of bainite and martensite, respectively, as well as the 60%M+40%B microstructure, as a case for the validation of predictions, were obtained using the measured data published by ten Kortenaar [89]. For Ductibor® 500-AS, the fully-ferritic and fully-martensitic microstructures could not be produced experimentally. Therefore, the 100%F and 100%M fracture *loci* were determined by the extrapolation of the MMC fracture *loci* [188] of the produced microstructures in the current research (~96%F+4%M, ~57%F+43%M, and ~10%F+90%M) based on the dependency of the fracture *locus* on the martensite volume fraction (V_m). It is noted that the fracture *loci* of the mixed-phase microstructures were obtained using the measured fracture data presented in Section 4.1.3.

For Usibor® 1500-AS, the practical range of the GISSMO damage exponent for each phase ($n^{(r)}$) was obtained by linking the GISSMO damage parameter with the corresponding fracture *locus* (100%B or 100%M) and monitoring the predicted fracture strains for the corresponding single-phase microstructure such that they lay within the measured ranges in all of the loading states. The final values of $n^{(r)}$ for bainite and martensite, *i.e.* $n^{(b)} = n^{(m)} = 0.6$, from the calculated ranges were found to provide the best predictions of the fracture strains for the mixed-phase microstructure (60%M+40%B). For Ductibor® 500-AS, the effects of variations in the strength of the micro-constituents in the mixed ferritic-martensitic microstructures on the fracture response were unknown. Consequently, the GISSMO damage exponent for each phase was considered to be a fitting parameter so that the predicted fracture strains for the three developed microstructures have the least deviations with respect to the measured fracture data. To find the optimum damage exponents, *i.e.* $n^{(f)} = 1.05$ and $n^{(m)} = 0.6$, an optimization code based on the least-square problem was written in FORTRAN 90. Further details about obtaining the fracture *loci* and the calibration of the various fracture parameters can be found in Appendices A and C.

Hence, for each step of deformation during the MFH modelling, the damage parameter in each phase of the mixed-phase microstructures was updated using its predicted equivalent plastic strain increment, calibrated damage exponent, and fracture strain corresponding to its calculated instantaneous stress triaxiality (η) and Lode parameter (ξ). Finally, fracture was predicted to occur once the GISSMO damage indicator in any of the individual phases became unity. This solution scheme was implemented into a FORTRAN 90 code, and the fracture strains for the bainitic-martensitic and ferritic-martensitic microstructures of Usibor® 1500-AS and Ductibor® 500-AS, respectively, were predicted for a range of micro-constituent volume fractions under various loading conditions. Figures 32-35 show the predicted fracture strains for the studied mixed-phase microstructures of Usibor® 1500-AS and Ductibor® 500-AS, along with the measured data. Figure 36 illustrates the predicted and interpolated (experiment-based) Bai-Wierzbicki or MMC fracture *loci* for these microstructures. As can be seen, the predicted fracture strains and *loci* for the studied microstructures have very good agreement with the experiment-based results.

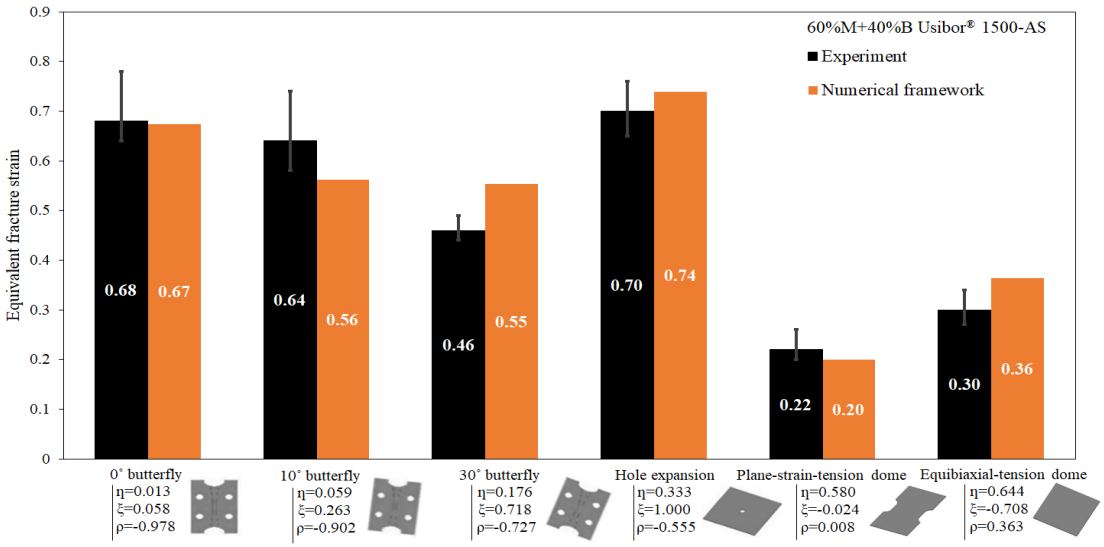

Figure 32: The predicted and measured equivalent fracture strains for the 60%M+40%B microstructure of Usibor® 1500-AS. Note that the error bars represent the measured data variations.

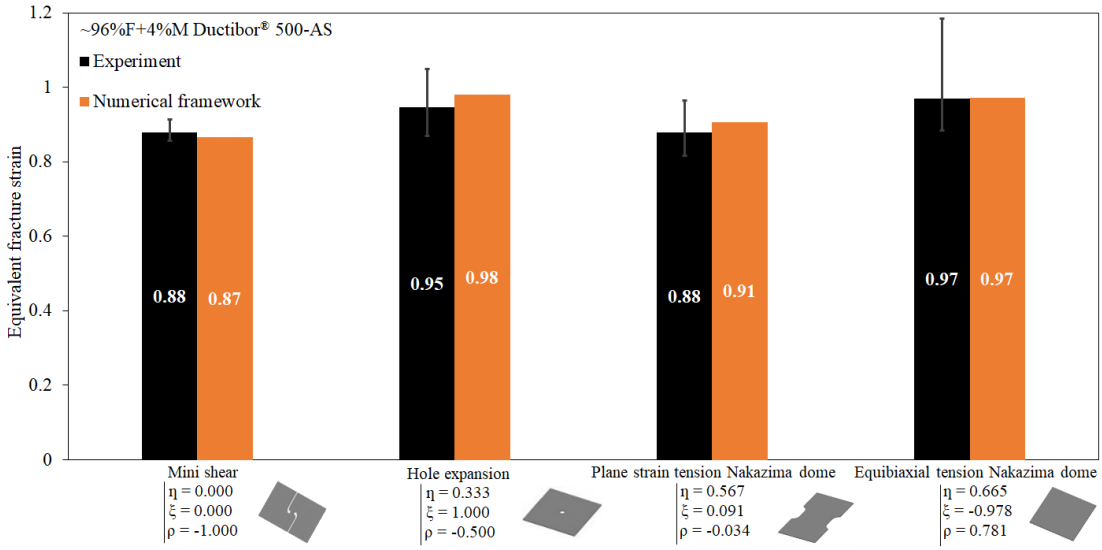

Figure 33: The predicted and measured equivalent fracture strains for the ~96%F+4%M microstructure of Ductibor® 500-AS. Note that the error bars represent the measured data variations.

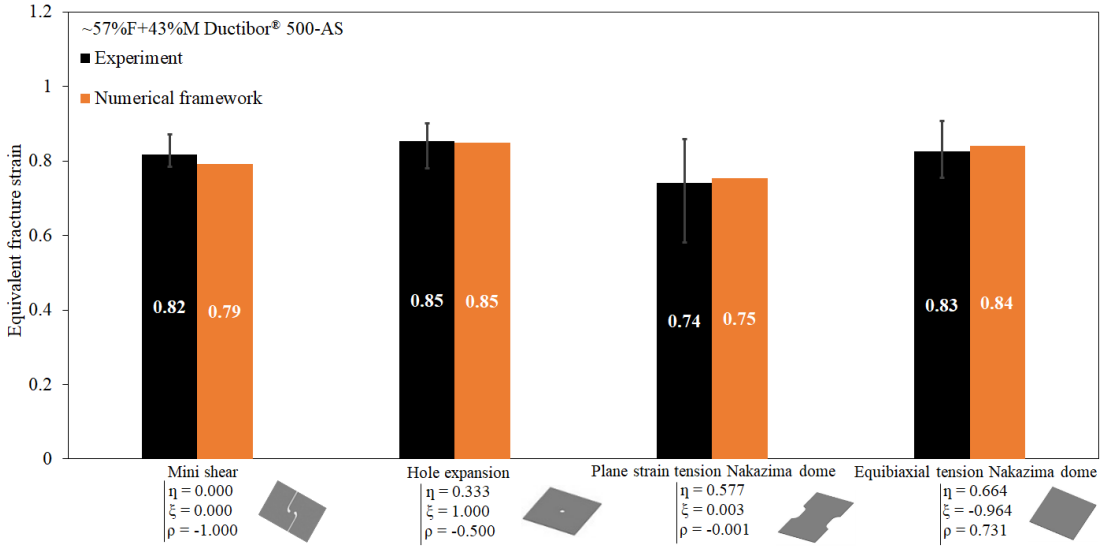

Figure 34: The predicted and measured equivalent fracture strains for the ~57%F+43%M microstructure of Ductibor® 500-AS. Note that the error bars represent the measured data variations.

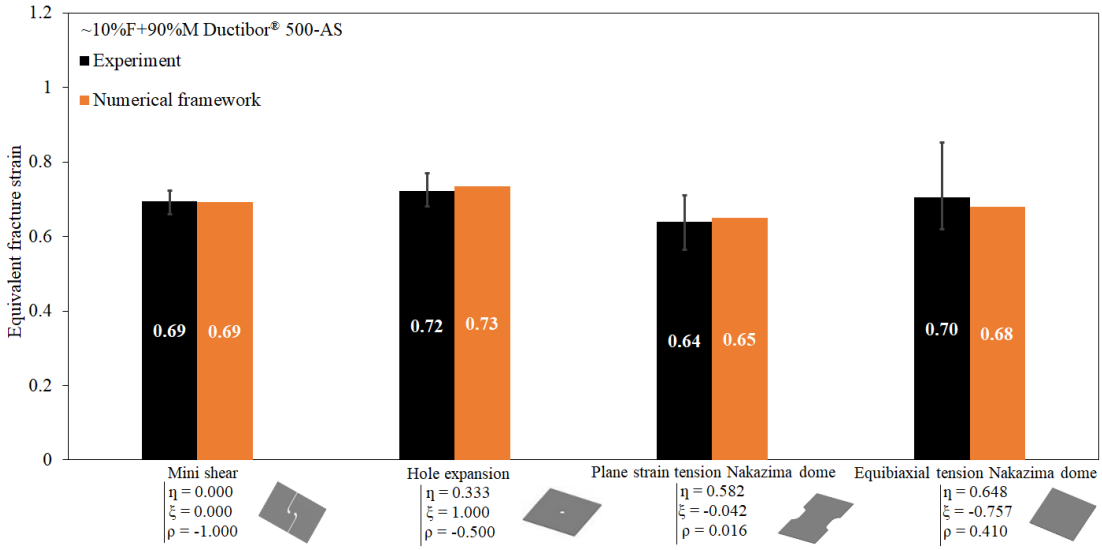

Figure 35: The predicted and measured equivalent fracture strains for the ~10%F+90%M microstructure of Ductibor® 500-AS. Note that the error bars represent the measured data variations.

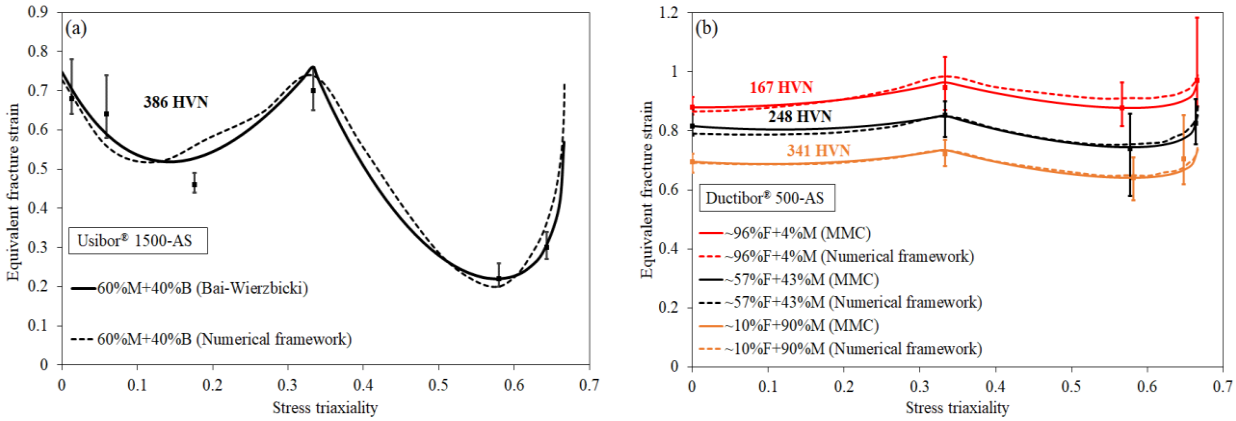

Figure 36: The predicted fracture *loci* of the studied mixed-phase microstructures of (a) Usibor® 1500-AS and (b) Ductibor® 500-AS, compared to their interpolated (experiment-based) Bai-Wierzbicki or MMC fracture *loci*. Note that the symbols and error bars represent the averaged measured data and variations in the experimental data.

Given such good predictions for the measured fracture strains and corresponding fracture *loci*, the numerical solution scheme was employed to predict the fracture *loci* for a range of the bainitic-martensitic and ferritic-martensitic microstructures of Usibor® 1500-AS and Ductibor® 500-AS, respectively. The predictions, displayed in Figures 37, demonstrate that as the martensite volume fraction increases, the overall ductility of the steel decreases. Such predictions complement the strength predictions in Figure 30 to account for the effects of variations in local cooling rates and resulting microstructures in the hot-stamping process on the fracture resistance of complex, hot-stamped products. A potential use of this data lies in the mapping of local properties within

hot-stamped component models in crash simulations based on the corresponding micro-constituent volume fractions.

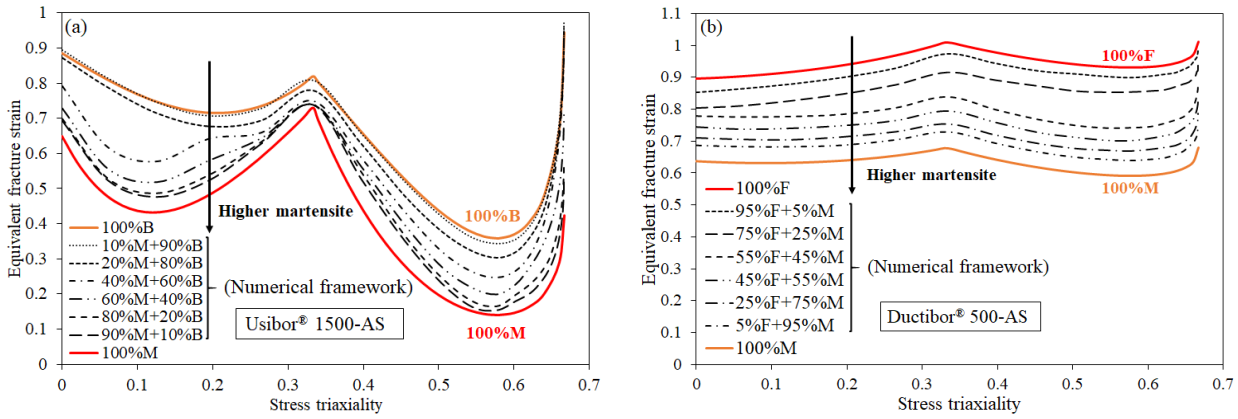

Figure 37: The predicted fracture *loci* of the several (a) bainitic-martensitic microstructures of Usibor® 1500-AS and (b) ferritic-martensitic microstructures of Ductibor® 500-AS for a range of the micro-constituent volume fractions based on the developed numerical framework. Note that for reference, the fracture *loci* of the 100%B and 100%M Usibor® 1500-AS as well as 100%F and 100%M Ductibor® 500-AS are also displayed.

More details about the modelling of fracture in the mixed-phase microstructures of Usibor® 1500-AS and Ductibor® 500-AS as well as the predictions of damage accumulation and fracture onset within the constituent phases can be found in Appendices A and C.

4.4. Task 4: Finite-Element (FE) Modelling of Constitutive and Fracture Response of Hot-Stamped TWBs

The modelling of the constitutive (flow) and fracture response of the hot-stamped laser-welded blanks of Usibor® 1500-AS and Ductibor® 500-AS was performed *via* FE simulations of TWB mechanical tests using the LS-DYNA software [212]. The longitudinal and transverse uniaxial tension as well as equibiaxial tension Nakazima dome tests on the hot-stamped mono- and multi-gauge TWBs, presented in Sections 4.2.2.1 and 4.2.2.2, were simulated using a shell element formulation so as to maintain compatibility with current automotive crash simulation practice. The V-bend tests, presented in Section 4.2.2.3, were not simulated since the severe through-thickness stress and strain gradients in that test mandate the use of fine solid elements; however, the plane-strain tension loading of the TWBs is captured within the Nakazima dome simulations.

To simulate the fracture tests, the integrated hardness-mapped models of the TWB specimens (Figure 38) were generated using a user-defined material (UMAT) subroutine, developed by O'Keeffe and Butcher [213]. In these TWB models, the hardness of each region, *i.e.* the parent metals and weld, was mapped to the corresponding elements, given the results of the hardness measurements presented in Section 4.2.1. Then the mechanical properties for each hardness were assigned to the respective elements.

The hardness of the hot-stamped Usibor® 1500-AS in all TWBs was around 495 HVN, corresponding to a 100%M microstructure. For this material condition, the flow curve was taken from the work by Omer *et al.* [12], and the Bai-Wierzbicki fracture *locus* was adopted based on the fracture data reported by ten Kortenaar *et al.* [52,201] and Cheong *et al.* [199]. In the mono-gauge TWBs, the hardness of the hot-stamped Ductibor® 500-AS was around 248 HVN, corresponding to a 57%F+31%M+12%TM/B microstructure. This as-quenched material corresponded to the 1.2-mm-thick monolithic die-cooled Ductibor® 500-AS sheet characterized in the parent-metal study (Section 4.1.1). Therefore, the corresponding flow response and fracture *locus* were used. In the multi-gauge TWB, the hot-stamped Ductibor® 500-AS exhibited a somewhat softer microstructure of 73%F+27%M, with a hardness value of 218 HVN (See Section 4.2.1). The hardening curve and fracture *locus* for this material condition were calculated using the proposed microstructure-based modelling approach described in Sections 4.3.1 and 4.3.2. Figure 39 shows the input data of mechanical properties for the parent metals of the studied TWBs.

For the weld zone, according to the trend seen in the variation of the measured hardness across the weld line of the TWBs, *i.e.* a monotonic increase over the weld width of 1.6 mm from the softer parent metal to the harder one (See Section 2.4.1), the hardness variation within the weld was assumed to be linear. Correspondingly, the mechanical response across the weld zone was approximated to vary linearly between that of the parent metals in terms of hardness. Therefore, the hardening curves and fracture limits of the elements within the weld region were obtained *via* the linear interpolation of those the parent metals based on the mapped hardness. It is noted that to better understand the importance of the modelling of the narrow weld region in the laser-welded blanks, the simulations were also conducted once without considering the weld region in the TWB models *via* interfacing Usibor® 1500-AS and Ductibor® 500-AS at the weld center, and the results were compared with those of the "with weld" simulations.

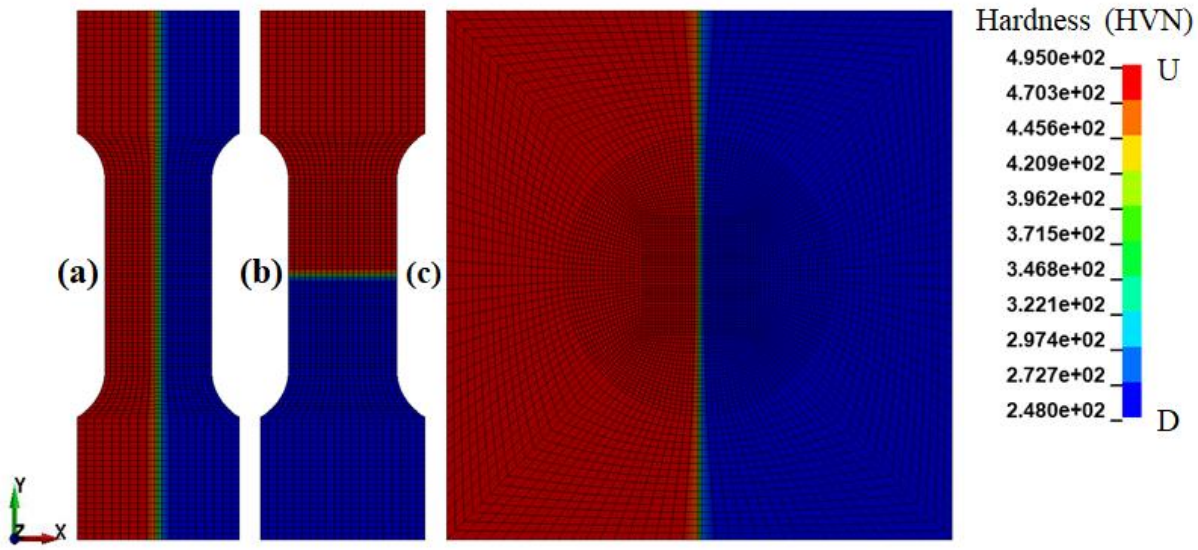

Figure 38: The integrated hardness-mapped models of the (a) tensile longitudinal, (b) tensile transverse, and (c) equibiaxial tension Nakazima dome TWBs. Note that U and D represent Usibor® 1500-AS and Ductibor® 500-AS, respectively.

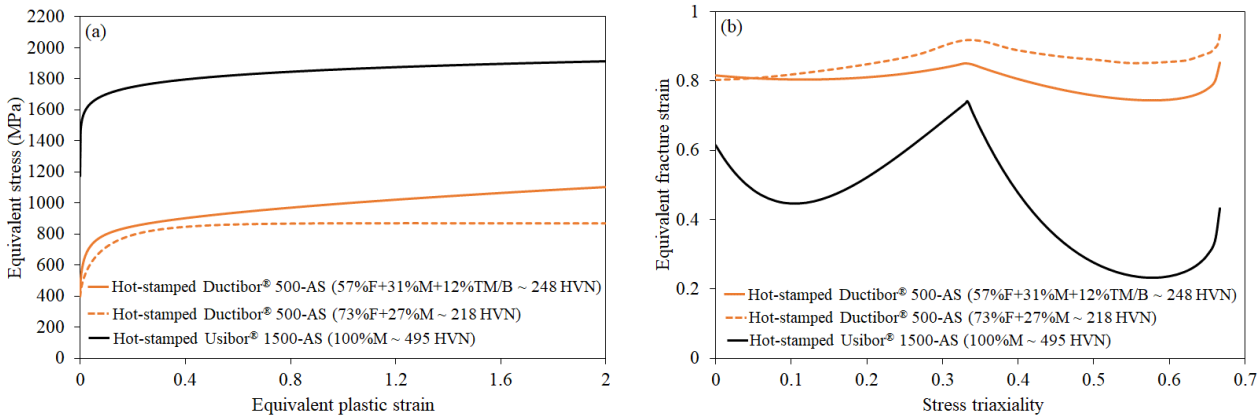

Figure 39: The (a) flow curves and (b) fracture *loci* of the hot-stamped Ductibor® 500-AS and Usibor® 1500-AS. Note that the solid lines correspond to measured data for the 248 HVN Ductibor® 500-AS and 495 HVN Usibor® 1500-AS, while the dashed lines correspond to predictions for the 218 HVN Ductibor® 500-AS using the developed microstructure-based numerical framework.

The simulations were performed within an explicit time integration scheme with the von Mises yield criterion for material yielding and the GISSMO damage model for material fracture. To reduce the dependency of damage accumulation on the element size, mesh regularization was conducted for two different stress states corresponding to stress triaxiality levels of approximately 0.57 (plane-strain tension) and 0.67 (equibiaxial tension). For this purpose, the Nakazima dome tests of the parent metals (495 HVN Usibor® 1500-AS and 248 HVN Ductibor® 500-AS) with the plane-strain and equibiaxial tension geometries [89] were simulated with element sizes of 1 mm, 1.25 mm, 2.5 mm, and 5 mm. The scale factors of the experimental fracture curves for each mesh

size and loading condition (Figure 40) were determined such that the predicted displacement at fracture matched the measured data. For the Nakazima dome test simulations of the hot-stamped TWBs of the 495 HVN Usibor® 1500-AS and 248 HVN Ductibor® 500-AS for which a plane-strain tension condition was dominant at the fracture point during the testing (Figure 21), the plane-strain tension regularization curves of the parent metals were used. However, for the other simulations, their equibiaxial tension regularization curves were utilized. It is noted that for the 218 HVN Ductibor® 500-AS, the equibiaxial tension regularization curve of the 248 HVN Ductibor® 500-AS was adopted for all of the simulations. More details about the simulation specifications can be found in Appendix D.

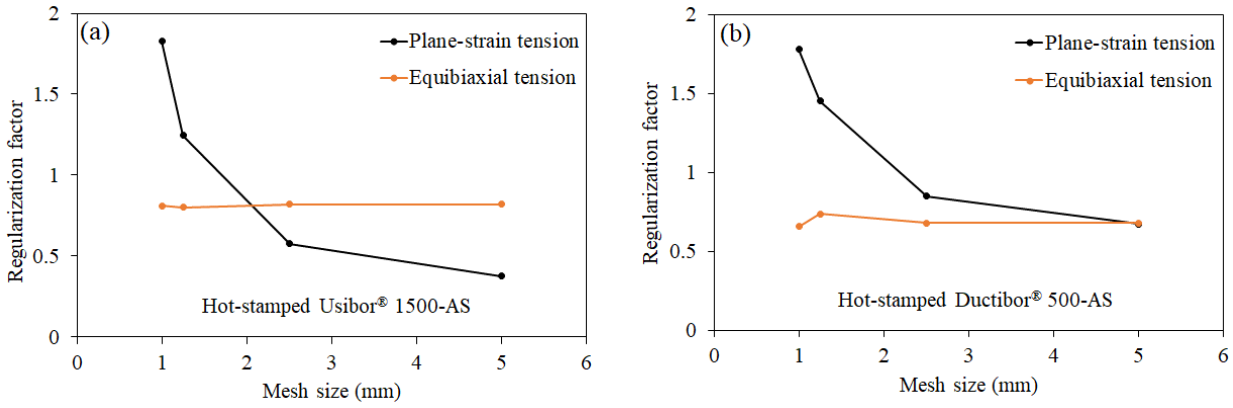

Figure 40: The mesh regularization curves for the hot-stamped (a) Usibor® 1500-AS (495 HVN) and (b) Ductibor® 500-AS (248 HVN) obtained from simulations of the plane-strain and equibiaxial tension Nakazima dome tests.

4.4.1. Tensile Test Results

Figure 41 shows the predicted and measured engineering stress-strain response of the various tensile longitudinal and transverse TWBs. Figure 42 presents the predicted UTS and elongation to fracture for different TWB tensile models (with and without the weld region), compared to the measured data. It is seen that the predicted hardening behavior of the TWBs, with and without considering the weld region, matches well with the measured data over the range of the deformation histories. The predicted UTS values for all TWB types, based on both modelling approaches, have less than 5% deviation from the measured data. The elongation to fracture for the transverse TWB tensile models was predicted relatively well, although the simulations that considered the weld region in the TWB models had slightly better predictions in this case. The total elongation of the longitudinal TWB tensile models was somewhat overestimated with and

without considering the weld region. The reason for this overprediction is attributed to the fact that the regularization factors employed in the tensile test models corresponded to the equibiaxial tension loading conditions. A comparison of the contour plots of the measured and predicted (from the "with weld" simulation) major true strain distributions before fracture in the longitudinal and transverse tensile tests in Figures 16 and 17, respectively, reveals that the predicted strain distributions agree well with the DIC data. The predicted and experimental strain-localization patterns are comparable. In the case of the transverse TWB tensile model, the simulation showed two symmetric shear bands in the necking zone (Figure 17b), in contrast to the experiment with only one shear band (Figure 17a). Such an observation is related to the fact that the properties were uniformly assigned in the entire sample in the simulation, whereas the real material locally exhibits some degree of variation. For this reason, one of the shear bands has become dominant during the experiment. It should be noted that the simulations also accurately predicted the location of strain localization (and fracture initiation) in the Usibor® 1500-AS and Ductibor® 500-AS sides in the longitudinal and transverse tensile samples, respectively. Similar predictions for the strain distributions and fractured materials and locations were obtained from the "without weld" simulations.

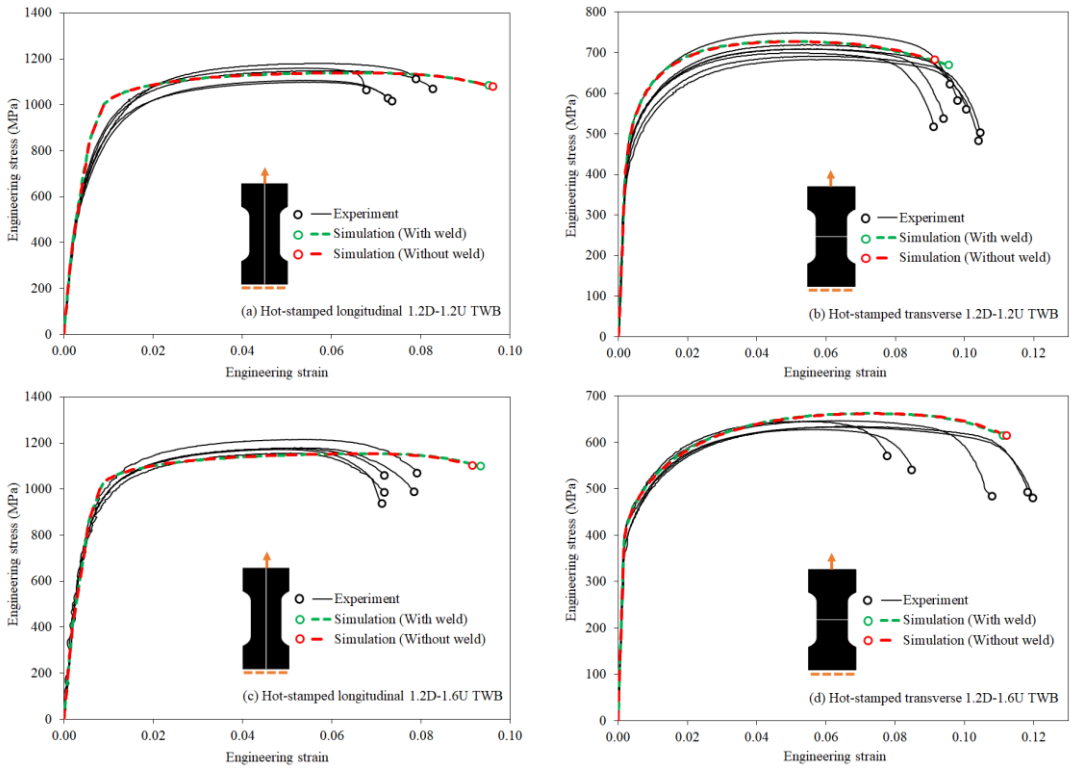

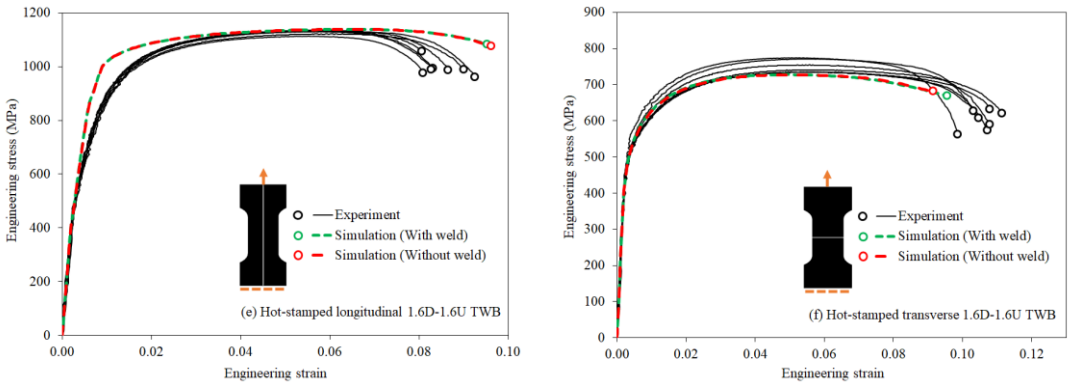

Figure 41: The predicted and measured engineering stress-strain curves of the TWB tensile samples: (a) longitudinal and (b) transverse 1.2-mm-thick mono-gauge; (c) longitudinal and (d) transverse multi-gauge; and (e) longitudinal and (f) transverse 1.6-mm-thick mono-gauge TWBs. Note that the circular markers represent the fracture points.

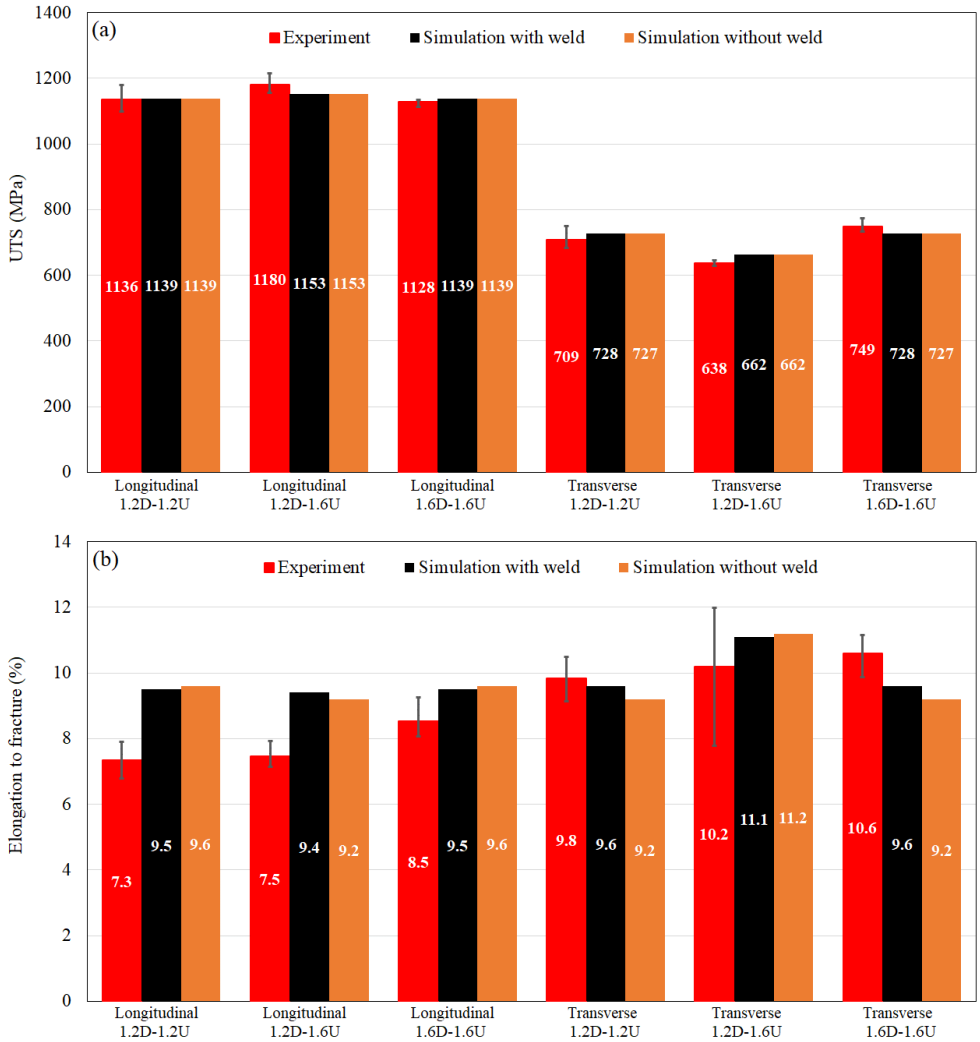

Figure 42: A comparison of the predicted and measured (a) UTS and (b) elongation to fracture in the TWB tensile tests. Note that the indicated variations are the measured data variations.

4.4.2. Nakazima Dome Test Results

Figure 43 shows the predicted and measured punch load *versus* punch displacement during the equibiaxial tension Nakazima dome tests of the various TWBs. Figure 44 presents the predicted maximum punch load and punch displacement to fracture for the different TWB models, compared to the measured data. As can be seen, the load-displacement response for the mono- and multi-gauge TWBs were predicted very well with and without the weld region modelling. No significant difference between the predicted and measured maximum load and fracture displacements can be observed for the cases of mono-gauge TWBs. However, the simulation with the weld region modelling had better predictions of the maximum load and fracture displacement in the case of the multi-gauge TWB. A comparison of the contour plots of the measured and predicted (from the "with weld" simulation) major true strain distributions prior to fracture in the Nakazima dome test in Figure 20 shows that strain localization (and fracture initiation) in the Ductibor® 500-AS side around the interface with the weld was correctly predicted. The simulations without the weld region modelling had similar predictions for the strain distributions and fractured material but predicted fracture within Ductibor® 500-AS at the interface with Usibor® 1500-AS (which is the weld spot in reality) in the case of the mono-gauge TWBs. For the multi-gauge TWB, due to the thickness difference between the interface and adjacent elements within the Ductibor® 500-AS side, the "without weld" simulation accurately predicted fracture in the thinner (interior) elements. More details about the simulation results, including the predicted strain history and stress state, can be found in Appendix D.

The predictions of the hardness-mapped TWB models with two "with weld" and "without weld" scenarios provide an insight into the need for taking account of the small-sized weld region of laser-welded blanks in crash simulations. It can be stated that the exclusion of the weld region in the TWB models still results in acceptable estimations for the mechanical behavior of the hot-stamped laser-welded blanks of Usibor® 1500-AS and Ductibor® 500-AS. The reason is related to the narrow size of the weld region in the laser-welded blanks as well as the intermediate hardness of the weld zone (no softened HAZ) in the hot-stamped TWBs of Usibor® 1500-AS and Ductibor® 500-AS so that weld fracture is not a concern. However, the modelling of the weld region with the interpolated mechanical properties of the parent metals based on the trend seen in the hardness variations across the weld can lead to more precise predictions for the load-displacement response

and fracture locations. The consideration of the weld region in the TWB models becomes more crucial when the weld region incorporates an area harder and/or softer than both of the parent metals, for example in laser-welded blanks of similar and dissimilar DP steels [214,215]. In these TWB types, dependent on the loading direction with respect to the weld line, fracture can occur within the softer HAZ or harder fusion zone, and therefore, the modelling of the weld region helps to more accurately predict the instant and location of fracture [73,214–216].

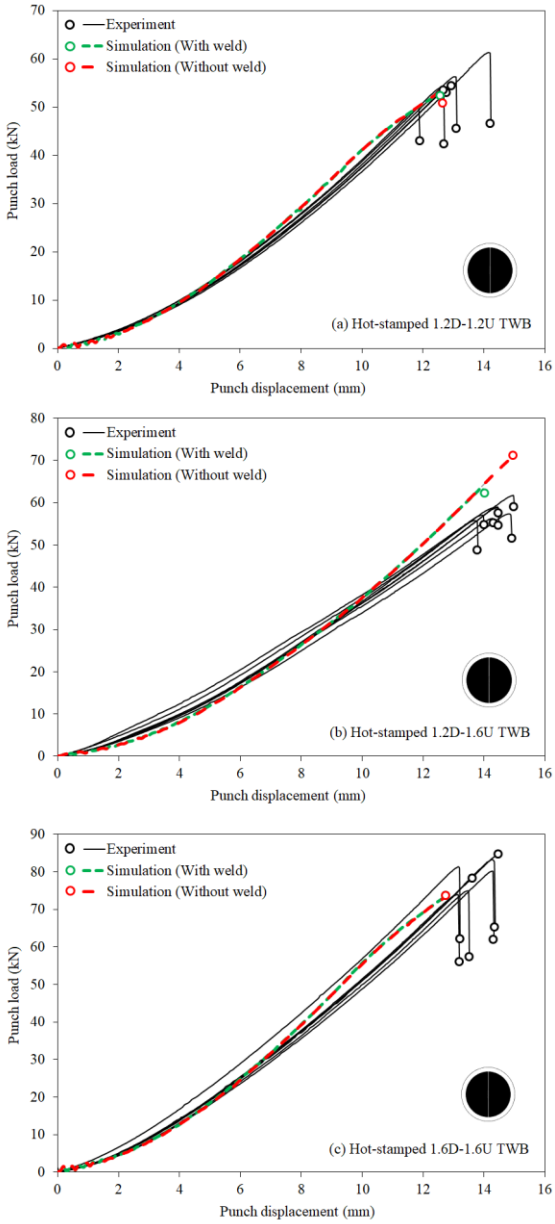

Figure 43: The predicted and measured punch load *versus* punch displacement curves of the Nakazima dome samples: a) 1.2-mm-thick mono-gauge; b) multi-gauge; and c) 1.6-mm-thick mono-gauge TWBs. Note that the circular markers represent the fracture points.

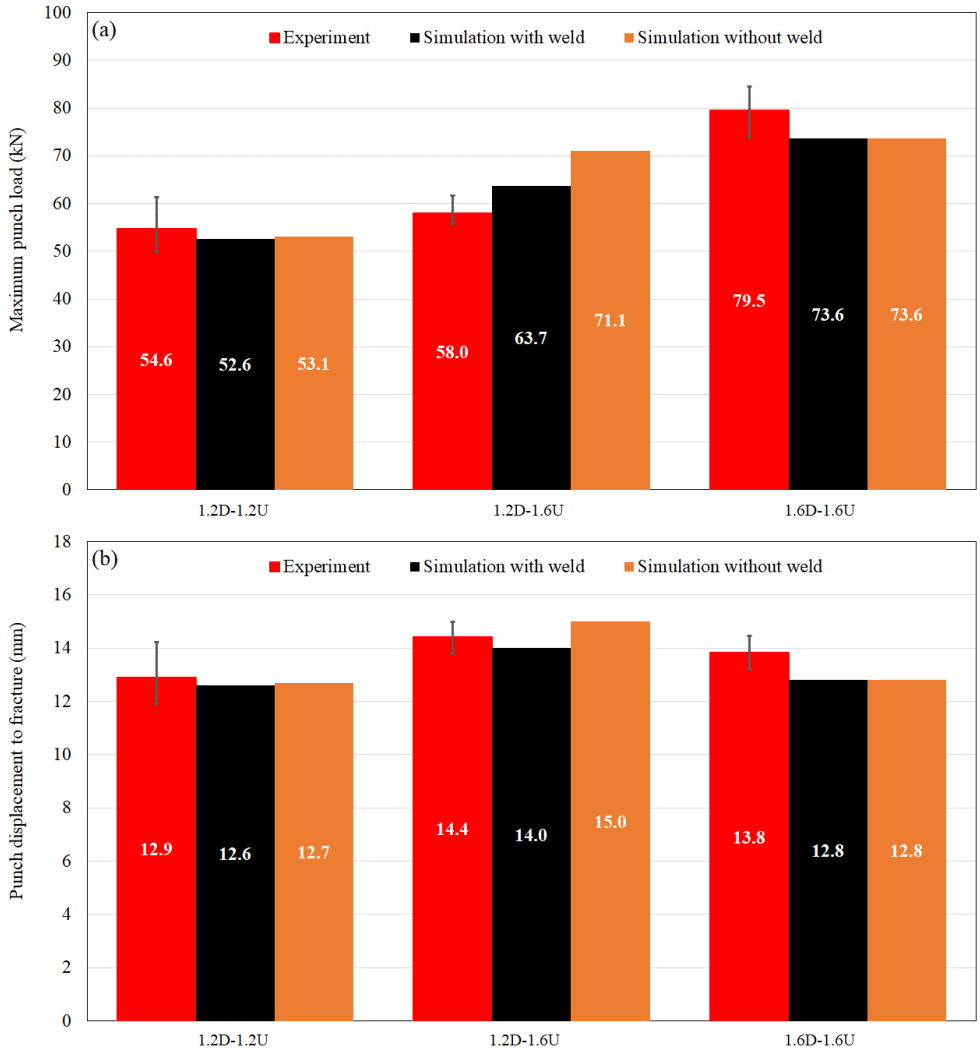

Figure 44: A comparison of the predicted and measured maximum punch load and punch displacement to fracture in the TWB equibiaxial tension Nakazima dome tests. Note that the indicated variations are the measured data variations.

Chapter 5: Conclusions and Recommendations for Future Work

5.1. Conclusion

The current research established numerical frameworks to predict the influences of the microstructure on the constitutive (flow) behavior and fracture response of two hot-stamping steels, Usibor® 1500-AS and Ductibor® 500-AS, as well as their tailor-welded blanks (TWBs). Given the fact that the as-quenched microstructures in these alloys were found to be strong functions of quench rate, the developed numerical solution schemes contribute to better understand the impacts of processing conditions on the mechanical performance of final hot-stamped products. As part of the TWB studies, due to the discovered importance of incorporating the weld region in the finite-element (FE) simulations of the hot-stamped TWBs, the proposed modelling approach for the inclusion of the weld can be also useful to accurately predict the mechanical response for the TWB components in different as-quenched conditions. In fact, the main contribution of this research to science is the development of the aforementioned predictive tools that are capable of estimating changes in the mechanical properties of the steel workpieces during conventional and tailored hot-stamping processes, associated with wanted as well as unwanted variations of quench conditions. These numerical strategies can significantly reduce the need for time-consuming and costly characterization experiments and improve predictions for the mechanical performance of hot-stamped components within crash-safety simulations.

In the following, the main conclusions that stem from the present research are presented:

- The strength and ductility of Ductibor® 500-AS are strongly dependent on quench rate. Cooling rates of 5, 365, and 1890 °C/s result in tensile strength of 525, 721, and 810 MPa and elongation to fracture of 27.1, 17.6, and 7.3%, respectively.

- The as-quenched microstructures of Ductibor® 500-AS are normally composed of ferrite and martensite, with some tempered martensite/bainite locally found dependent on quench conditions.

- The Ductibor® 500-AS steel has much lower hardenability than the Usibor® 1500-AS steel. For Ductibor® 500-AS, a cooling rate even as high as 1890 °C/s cannot produce a

fully-martensitic microstructure, while the 100% martensitic Usibor® 1500-AS can be formed with a cooling rate as low as 50 °C/s.

- The die-cooled Ductibor® 500-AS, with UTS of 721 MPa and total elongation of 17.6%, offers lower strength and higher resistance to fracture than the die-cooled Usibor® 1500-AS (1500 MPa UTS and 6% elongation [18]). Such mechanical properties support the use of Ductibor® 500-AS, joined to Usibor® 1500-AS within TWBs, in hot-stamped energy-absorption components.

- The Ductibor® 500-AS sheet in the die-quenched condition exhibits appreciable plastic anisotropy in terms of the Lankford coefficient (R-value), which varies from 0.58 to 1.39 relying on the material direction.

- In the hot-stamped laser-welded blanks of Usibor® 1500-AS and Ductibor® 500-AS, the martensite content increases across the weld from the Ductibor® 500-AS side with a predominantly ferritic-martensitic microstructure towards the Usibor® 1500-AS side with a fully-martensitic microstructure. As a result, the hardness across the weld increases almost monotonically from the Ductibor® 500-AS parent metal to the Usibor® 1500-AS parent metal. No noticeable hardness drop is observed in the HAZs.

- The intermediate hardness level of the weld zone within the hot-stamped TWBs of Usibor® 1500-AS and Ductibor® 500-AS with respect to the parent metals makes these weldments less susceptible to failure within the weld. The high resistance to weld failure in these TWBs supports their commercial application within hot-stamped structural components.

- The location of fracture in the hot-stamped TWBs of Usibor® 1500-AS and Ductibor® 500-AS is a strong function of the loading orientation with respect to the weld line. Failure in these TWBs usually occurs within the softer parent metal (Ductibor® 500-AS) under predominantly-transverse loading and within the harder parent metal (Usibor® 1500-AS) under predominantly-longitudinal loading. The observed weld fracture during the 0° V-bend tests was due to the fact that the major principal strains were concentrated within the weld region for this loading case.

- The developed multi-scale modelling approach for Usibor® 1500-AS and Ductibor® 500-AS is able to predict the flow response and fracture limits of their as-quenched conditions as functions of microstructure with less than 10% error.

- The macroscale predictions revealed that as the martensite content in the as-quenched microstructures of Usibor® 1500-AS and Ductibor® 500-AS increases, the strength of the steels increases, whereas their overall ductility decreases. The predicted trends were consistent with the experimental results.

- The microscale predictions showed that in the mixed-phase microstructures of Usibor® 1500-AS and Ductibor® 500-AS, (i) the softer phase experiences higher strains, while the harder phase sustains higher stresses; (ii) the stress triaxiality of the softer phase exceeds the macroscopic value, while that of the harder phase stays below the macroscopic value; and (iii) the Lode parameter at the micro level is similar to that at the macro level.

- The modelling of the hardening behavior of the micro-constituents of the as-quenched microstructures of Ductibor® 500-AS using a dislocation-based hardening law revealed that as the martensite volume fraction increases, the strength of martensite and ferrite decreases and increases, respectively. The variations in the martensite strength are more pronounced due its strong dependence on the carbon content and the tendency of ferrite to shed carbon because of the low solubility of carbon in ferrite, *i.e.* the carbon-partitioning effect.

- The proposed FE modelling strategy successfully predicts the load-displacement response, strain distribution, and location of fracture for the hot-stamped TWBs of Usibor® 1500-AS and Ductibor® 500-AS. This approach is more accurate than FE simulations without modelling the weld behavior and is computationally less expensive than multi-scale computational homogenization simulations.

5.2. Recommendations for Future Work

In an effort towards improving the understanding and modelling of the mechanical behavior of monolithic and tailor-welded blanks of press-hardening steels in various as-quenched conditions, the following recommendations for potential future work are presented:

- In the current work, the range of the quench rates considered for the evaluation of the quench-rate sensitivity of the mechanical response of Ductibor® 500-AS was more extreme than that expected in the industrial hot-stamping process. It is important to further assess the quench-rate sensitivity of this alloy in terms of mechanical properties under commercial hot-stamping conditions and its influence on the crash energy absorption of structural components.

- This study focused on the flow and fracture response of Ductibor® 500-AS and its TWBs with Usibor® 1500-AS under quasi-static conditions. Future work should expand these investigations to consider dynamic loading for revealing variations in the behavior of these materials due to higher strain rates and adiabatic heating.

- In the fracture characterization campaigns, the ductility of the steels under equibiaxial tension loading was evaluated using standard Nakazima dome tests. However, due to the noticeable localized necking and friction involved during these tests, significant deviations from the equibiaxial stretching strain state were observed. To reduce such errors, Nakazima dome tests with mini hemispherical punches [217] are recommended, in which through-thickness necking is considerably suppressed, and friction is reduced due to the lower contact between the sample and punch.

- In this study, the proposed damage-predictive modelling approach for press-hardening steels was evaluated only under proportional loading conditions. Future work should consider the performance of this technique under non-proportional loading states. For this purpose, there is a need for the employment of the linearization schemes for the MFH modelling that are suitable for general loading conditions, *e.g.* tangent-based and incremental secant-order linearization methods.

- In this study, the effects of carbon partitioning on the mechanical properties of the micro-constituents of the as-quenched microstructures of Usibor® 1500-AS were neglected. Future work should investigate how the consideration of this phenomenon can affect predictions.

- Future work should consider the implementation of the developed numerical modelling approach for mixed-phase press-hardening steels within a user-defined material (UMAT) subroutine for the finite-element method software. In such a case, damage accumulation in microstructure-mapped elements will be tracked based on the response of the micro-constituents of the assigned microstructures.

- The proposed damage-predictive methodology for multi-phase press-hardening steels is able to predict fracture initiation within the constituent phases. Future work should consider the evaluation of the accuracy of such predictions *via* metallurgical investigations at the microscale.

- Recently, ArcelorMittal has introduced a new grade of hot-stamping steels, namely Ductibor® 1000-AS, that potentially offers higher strength and energy absorption compared to Ductibor® 500-AS. Future work should evaluate the performance of the developed numerical solution schemes in the modelling of the flow and fracture response of the as-quenched microstructures of this steel and its hot-stamped TWBs with Usibor® 1500-AS.

References

[1] A. Bardelcik, C.P. Salisbury, S. Winkler, M.A. Wells, M.J. Worswick, Effect of cooling rate on the high strain rate properties of boron steel, Int. J. Impact Eng. 37 (2010) 694–702. doi:10.1016/j.ijimpeng.2009.05.009.

[2] A. Bardelcik, M.J. Worswick, S. Winkler, M.A. Wells, A strain rate sensitive constitutive model for quenched boron steel with tailored properties, Int. J. Impact Eng. 50 (2012) 49–62. doi:10.1016/j.ijimpeng.2012.06.007.

[3] A. Bardelcik, M.J. Worswick, M.A. Wells, The influence of martensite, bainite and ferrite on the as-quenched constitutive response of simultaneously quenched and deformed boron steel - Experiments and model, Mater. Des. 55 (2014) 509–525. doi:10.1016/j.matdes.2013.10.014.

[4] P. Du Bois, C.C. Chou, B.B. Fileta, A.I. King, H.F. Mahmood, H.J. Mertz, J. Wismans, Vehicle crashworthiness and occupant protection, American Iron and Steel Institute, Southfield, 2004.

[5] P. Åkerström, Modelling and Simulation of Hot Stamping, Ph.D. thesis, Lulea University of Technology, 2006.

[6] M. Naderi, Hot Stamping of Ultra High Strength Steels, Ph.D. thesis, RWTH Aachen University, 2007.

[7] R. George, Hot Forming of Boron Steels with Tailored Mechanical Properties Experiments and Numerical Simulations, M.Sc. thesis, University of Waterloo, 2011.

[8] A. Bardelcik, High Strain Rate Behaviour of Hot Formed Boron Steel with Tailored Properties, Ph.D. thesis, University of Waterloo, 2012.

[9] H. Karbasian, A.E. Tekkaya, A review on hot stamping, J. Mater. Process. Technol. 210 (2010) 2103–2118. doi:10.1016/j.jmatprotec.2010.07.019.

[10] P. Samadian, M. Habibi Parsa, A. Shakeri, Determination of proper austenitization

temperatures for hot stamping of AISI 4140 steel, J. Mater. Eng. Perform. 23 (2014) 1138–1145. doi:10.1007/s11665-014-0896-9.

[11] M. Naderi, M. Ketabchi, M. Abbasi, W. Bleck, Analysis of microstructure and mechanical properties of different boron and non-boron alloyed steels after being hot stamped, Procedia Eng. 10 (2011) 460–465. doi:10.1016/j.proeng.2011.04.078.

[12] K. Omer, L. ten Kortenaar, C. Butcher, M. Worswick, S. Malcolm, D. Detwiler, N. Adam, Testing of a Hot Stamped Axial Crush Member with Tailored Properties – Experiments and Models, Int. J. Impact Eng. 103 (2017) 12–28. doi:10.1016/j.ijimpeng.2017.01.003.

[13] M. Naderi, V. Uthaisangsuk, U. Prahl, W. Bleck, A numerical and experimental investigation into hot stamping of boron alloyed heat treated steels, Steel Res. (2009) 77–84. doi:10.2374/SRI07SP094-79-2008-77-84.

[14] P. Samadian, M. Habibi Parsa, H. Mirzadeh, Prediction of Proper Temperatures for the Hot Stamping Process Based on the Kinetics Models, J. Mater. Eng. Perform. 24 (2014) 572–585. doi:10.1007/s11665-014-1371-3.

[15] K. Omer, Development and Testing of a Hot Stamped Axial Crush Member with Tailored Properties, M.Sc. thesis, University of Waterloo, 2014.

[16] Y. Prajogo, Hot Stamping of a Boron Steel Side Impact Beam with Tailored Flange Properties - Experiments and Numerical Simulations, M.Sc. thesis, University of Waterloo, 2015.

[17] K. Mori, S. Maki, Y. Tanaka, Warm and Hot Stamping of Ultra High Tensile Strength Steel Sheets Using Resistance Heating, CIRP Ann. - Manuf. Technol. 54 (2005) 209–212. doi:10.1016/S0007-8506(07)60085-7.

[18] ArcelorMittal, Steels for hot stamping, Technical report, 2008.

[19] M. Maikranz-Valentin, U. Weidig, U. Schoof, H. Becker, K. Steinhoff, Components with Optimised Properties due to Advanced Thermo-mechanical Process Strategies in Hot Sheet Metal Forming, Steel Res. Int. 79 (2008) 92–97. doi:10.2374/SRI07SP115-79-2008-92-97.

[20] N. Li, Fundamentals of Materials Modelling for Hot Stamping of UHSS Panels With Graded Properties, Ph.D. thesis, Imperial College London, 2013.

[21] S.K. Panda, D.R. Kumar, H. Kumar, A.K. Nath, Characterization of tensile properties of tailor welded IF steel sheets and their formability in stretch forming, J. Mater. Process. Technol. 183 (2007) 321–332. doi:10.1016/j.jmatprotec.2006.10.035.

[22] E. Bayraktar, D. Kaplan, B.S. Yilbas, Comparative study: Mechanical and metallurgical aspects of tailored welded blanks (TWBs), J. Mater. Process. Technol. 204 (2008) 440–450. doi:10.1016/j.jmatprotec.2007.11.088.

[23] F. Xu, C. Wang, Dynamic axial crashing of tailor-welded blanks (TWBs) thin-walled structures with top-hat shaped section, Adv. Eng. Softw. 96 (2016) 70–82. doi:10.1016/j.advengsoft.2016.02.003.

[24] M. Kang, C. Kim, Laser welding for hot-stamped tailor-welded blanks with high-strength steel/high-energy absorption steel, J. Laser Appl. 26 (2014) 1–6. doi:10.2351/1.4881279.

[25] S.M. Chan, L.C. Chan, T.C. Lee, Tailor-welded blanks of different thickness ratios effects on forming limit diagrams, J. Mater. Process. Technol. 132 (2003) 95–101. doi:10.1016/S0924-0136(02)00407-7.

[26] M. Merklein, M. Johannes, M. Lechner, A. Kuppert, A review on tailored blanks - Production, applications and evaluation, J. Mater. Process. Technol. 214 (2014) 151–164. doi:10.1016/j.jmatprotec.2013.08.015.

[27] ArcelorMittal, Steels for hot stamping -Usibor® and Ductibor®, Technical report, 2017.

[28] H. Souther, American Automobile Steel, New York Times. (1909).

[29] C.M. Tamarelli, AHSS 101: the evolving use of advance high-strength steel for automotive applications, 2011.

[30] D.K. Matlock, J.G. Speer, E. De Moor, Recent AHSS Developments for Automotive Applications : Processing , Microstructures , and Properties, Colorado, 2012.

[31] Ducker Worldwide LLC., Light Vehicle Steel Content - Executive Summary, (2011).

[32] E. Billur, T. Altan, Three Generations of Advanced High-Strength Steels for Automotive Applications, Part I, The First Generation, Stamp. J. (2013) 16–17.

[33] N. Baluch, Advanced High Strength Steel in Auto Industry : an Overview, Eng. Technol. Appl. Sci. Res. 4 (2014) 686–689.

[34] R. Östlund, Microstructure Based Modelling of Ductile Fracture in Quench-Hardenable Boron Steel, Ph.D. thesis, Luleå University of Technology, 2015.

[35] A. Naganathan, L. Penter, Sheet Metal Forming—Processes and Applications: Hot Stamping, ASM International®, 2012.

[36] T. Taylor, A. Clough, Critical review of automotive hot-stamped sheet steel from an industrial perspective, Mater. Sci. Technol. 34 (2018) 809–861. doi:10.1080/02670836.2018.1425239.

[37] P. Belanger, Steel innovations in hot stamping, in: Gt. Des. Steel, Michigan, 2016.

[38] M. Naderi, M. Ketabchi, M. Abbasi, W. Bleak, Semi-hot Stamping as an Improved Process of Hot Stamping, J. Mater. Sci. Technol. 27 (2011) 369–376. doi:10.1016/S1005-0302(11)60076-5.

[39] Y. Dahan, Y. Chastel, P. Duroux, P. Hein, E. Massoni, J. Wilsius, Formability Investigations for the Hot Stamping Process, in: Int. Deep Draw. Res. Gr., Porto, Portugal, 2006.

[40] J. Wilsius, B. Tavernier, D. Abou-Khalil, Experimental and Numerical Investigation of Various Hot Stamped B-Pillar Concepts Based on Usibor® 1500P, in: 3rd Int. Conf. Hot Sheet Met. Form. High-Performance Steel, Kassel, Germany, 2010.

[41] T. Labudde, W. Bleck, Formability characterisation of press hardened steels, in: 2nd Int. Conf. Hot Sheet Met. Form. High-Performance Steel, Lulea, Sweden, 2009.

[42] K. Omer, R. George, A. Bardelcik, M. Worswick, S. Malcolm, D. Detwiler, Development

of a hot stamped channel section with axially tailored properties – experiments and models, Int. J. Mater. Form. 11 (2018) 149–164. doi:10.1007/s12289-017-1338-7.

[43] R. George, A. Bardelcik, M.J. Worswick, Hot forming of boron steels using heated and cooled tooling for tailored properties, J. Mater. Process. Technol. 212 (2012) 2386–2399. doi:10.1016/j.jmatprotec.2012.06.028.

[44] K. Mori, Y. Okuda, Tailor die quenching in hot stamping for producing ultra-high strength steel formed parts having strength distribution, CIRP Ann. - Manuf. Technol. 59 (2010) 291–294. doi:10.1016/j.cirp.2010.03.107.

[45] H. Bodin, A method of hot stamping and hardening an object from a metal sheet, and a B-pillar for a vehicle, 9505443, 2016.

[46] M. Merklein, J. Lechler, T. Stoehr, Investigations on the thermal behavior of ultra high strength boron manganese steels within hot stamping, Int. J. Mater. Form. 2 (2009) 259–262. doi:10.1007/s12289-009-0505-x.

[47] M. Merklein, T. Svec, Hot stamping: Manufacturing functional optimized components, Prod. Eng. 7 (2013) 141–151. doi:10.1007/s11740-012-0429-z.

[48] R. Perez-santiago, E. Billur, A. Ademaj, C. Sarmiento, R. Berlanga, T. Altan, Hot Stamping a B-Pillar with Tailored Properties : Experiments and Preliminary Simulation Results, in: 4th Int. Conf. Hot Sheet Met. Form. High-Performance Steel, Luleå, Sweden, 2013: pp. 83–90.

[49] ArcelorMittal, Steels for hot stamping -Usibor® and -Ductibor®, Technical report, 2018.

[50] H. Hagenah, M. Merklein, M. Lechner, A. Schaub, S. Lutz, Determination of the Mechanical Properties of Hot Stamped Parts from Numerical Simulations, Procedia CIRP. 33 (2015) 167–172. doi:10.1016/j.procir.2015.06.031.

[51] T.K. Eller, L. Greve, M.T. Andres, M. Medricky, A. Hatscher, V.T. Meinders, A.H. Van Den Boogaard, Plasticity and fracture modeling of quench-hardenable boron steel with tailored properties, J. Mater. Process. Technol. 214 (2014) 1211–1227.

doi:10.1016/j.jmatprotec.2013.12.015.

[52] L. ten Kortenaar, K. Omer, A. Bardelcik, M. Worswick, D. Detwiler, S. Malcolm, Implementation of a Failure Criterion for Axial Crush of Fully Hardened Boron Steel, in: Hot Sheet Met. Form. High-Performance Steel CHS2, 2015: pp. 157–166.

[53] S. Golling, R. Östlund, M. Oldenburg, Characterization of ductile fracture properties of quench-hardenable boron steel: Influence of microstructure and processing conditions, Mater. Sci. Eng. A. 658 (2016) 472–483. doi:10.1016/j.msea.2016.01.091.

[54] S. Golling, R. Östlund, M. Oldenburg, A stress-based fracture criteria validated on mixed microstructures of ferrite and bainite over a range of stress triaxialities, Mater. Sci. Eng. A. 674 (2016) 232–241. doi:10.1016/j.msea.2016.07.126.

[55] K. Mishra, Effects of Microstructure and Strain Rate on Deformation Behavior in Advanced High Strength Steels, M.Sc. thesis, Georgia Institute of technology, 2017.

[56] D.D. Múnera, A. Pic, D. Abou-khalil, F. Shmit, Innovative Press Hardened Steel Based Laser Welded Blanks Solutions for Weight Savings and Crash Safety Improvements, SAE Int. J. Mater. Manf. 1 (2008) 472–479. doi:10.4271/2008-01-1076.

[57] C.W. Peister, C. O'Keeffe, J. Imbert, C. Butcher, M.J. Worswick, Crash Testing and Modelling of Hot Stamped Multi-Gauge Tailor-Welded Automotive Axial Crush Structures, in: 2nd Int. Conf. Impact Load. Struct. Mater., Xi'an, China, 2018.

[58] C. Peister, C. O'Keeffe, M. Nemcko, J. Imbert, C. Butcher, M. Worswick, R. Soldaat, W. Bernert, C. Yau, E. DeNijs, S. Malcolm, J. Dykeman, Tailor Welded Hot Stamped Automotive Axial Crush Structures: Crash Experiments and Modelling, in: Int. Auto Body Congr., Dearborn, Michigan, USA, 2017.

[59] A.A.Zadpoor, J.Sinke, R.Benedictus, Mechanics of Tailor Welded Blanks: An Overview, Key Eng. Mater. 344 (2007) 373–382. doi:10.4028/www.scientific.net/KEM.344.373.

[60] P.W. Leech, Laser ablation of multilayered hot stamping foil, J. Mater. Process. Technol. 209 (2009) 4281–4285. doi:10.1016/j.jmatprotec.2008.11.022.

[61] C.H. Cheng, M. Jie, L.C. Chan, C.L. Chow, True stress-strain analysis on weldment of heterogeneous tailor-welded blanks-a novel approach for forming simulation, Int. J. Mech. Sci. 49 (2007) 217–229. doi:10.1016/j.ijmecsci.2006.08.012.

[62] A. Reis, P. Teixeira, J.F. Duarte, A. Santos, A. Barata Da Rocha, A.A. Fernandes, Tailored welded blanks - An experimental and numerical study in sheet metal forming on the effect of welding, Comput. Struct. 82 (2004) 1435–1442. doi:10.1016/j.compstruc.2004.03.039.

[63] A. Ramazani, K. Mukherjee, A. Abdurakhmanov, U. Prahl, M. Schleser, U. Reisgen, W. Bleck, Micro–macro-characterisation and modelling of mechanical properties of gas metal arc welded (GMAW) DP600 steel, Mater. Sci. Eng. A. 589 (2013) 1–14. doi:10.1016/j.msea.2013.09.056.

[64] L.C. Chan, S.M. Chan, C.H. Cheng, T.C. Lee, Formability and Weld Zone Analysis of Tailor-Welded Blanks for Various Thickness Ratios, J. Eng. Mater. Technol. 127 (2005) 179. doi:10.1115/1.1857936.

[65] M.P. Miles, B.J. Decker, T.W. Nelson, Formability and strength of friction-stir-welded aluminum sheets, Metall. Mater. Trans. A. 35 A (2004) 3461–3468. doi:10.1007/s11661-004-0183-8.

[66] C.H. Cheng, L.C. Chan, C.L. Chow, T.C. Lee, Experimental investigation on the weldability and forming behavior of aluminum alloy tailor-welded blanks, J. Laser Appl. 17 (2005) 81–88. doi:10.2351/1.1848521.

[67] P. Friedman, G. Kridli, Microstructural and mechanical investigation of aluminum tailor-welded blanks, J. Mater. Eng. Perform. 9 (2000) 541–551. doi:10.1361/105994900770345674.

[68] H. Kim, Y. Heo, N. Kim, H.Y. Kim, D. Seo, Forming and drawing characteristics of tailor welded sheets in a circular drawbead, J. Mater. Process. Technol. 105 (2000) 294–301. doi:10.1016/S0924-0136(00)00647-6.

[69] A. Buste, X. Lalbin, M.J. Worswick, J.A. Clarke, B. Altshuller, M. Finn, M. Jain, Prediction of Strain Distribution in Aluminum Tailor Welded Blanks for Different Welding

Techniques, Can. Metall. Q. 39 (2000) 1–10.

[70] H.R. Shakeri, A. Buste, M.J. Worswick, J.A. Clarke, F. Feng, M. Jain, M. Finn, Study of damage initiation and fracture in aluminum tailor welded blanks made via different welding techniques, J. Light Met. 2 (2002) 95–110. doi:10.1016/S1471-5317(02)00028-7.

[71] T. Meinders, A. Van Den Berg, J. Huétink, Deep drawing simulations of Tailored Blanks and experimental verification, J. Mater. Process. Technol. 103 (2000) 65–73. doi:10.1016/S0924-0136(00)00420-9.

[72] M. Abbasi, M. Ketabchi, H.R. Shakeri, M.H. Hasannia, Formability enhancement of galvanized IF-steel TWB by modification of forming parameters, J. Mater. Eng. Perform. 21 (2012) 564–571. doi:10.1007/s11665-011-9946-8.

[73] M.H. Razmpoosh, A. Macwan, E. Biro, Y. Zhou, A Microstructure and dynamic tensile characteristics of dissimilar fiber laser welded advanced high strength steels, Mater. Sci. Eng. A. 773 (2020) 138729. doi:10.1016/j.msea.2019.138729.

[74] M.H. Razmpoosh, A. Macwan, E. Biro, Y. Zhou, Effect of coating weight on fiber laser welding of Galvanneal-coated 22MnB5 press hardening steel, Surf. Coatings Technol. 337 (2018) 536–543. doi:10.1016/j.surfcoat.2018.01.053.

[75] N. Iwata, M. Matsui, N. Nakagawa, S. Ikura, Improvements in finite-element simulation for stamping and application to the forming of laser-welded blanks, J. Mater. Process. Tech. 50 (1995) 335–347. doi:10.1016/0924-0136(94)01396-I.

[76] A.A. Zadpoor, J. Sinke, R. Benedictus, Finite element modeling and failure prediction of friction stir welded blanks, Mater. Des. 30 (2009) 1423–1434. doi:10.1016/j.matdes.2008.08.018.

[77] W. Lee, K.H. Chung, D. Kim, J. Kim, C. Kim, K. Okamoto, R.H. Wagoner, K. Chung, Experimental and numerical study on formability of friction stir welded TWB sheets based on hemispherical dome stretch tests, Int. J. Plast. 25 (2009) 1626–1654. doi:10.1016/j.ijplas.2008.08.005.

[78] D. Banabic, Sheet Metal Forming Processes: Constitutive Modelling and Numerical Simulation, Springer, 2010. doi:10.1007/978-3-540-88113-1.

[79] L.C. Chan, C.H. Cheng, M. Jie, C.L. Chow, Damage-based Formability Analysis for TWBs, Int. J. Damage Mech. 14 (2005) 83–96. doi:10.1177/1056789505045929.

[80] S. Gaied, J.M. Roelandt, F. Pinard, F. Schmit, M. Balabane, Experimental and numerical assessment of Tailor-Welded Blanks formability, J. Mater. Process. Technol. 209 (2009) 387–395. doi:10.1016/j.jmatprotec.2008.02.031.

[81] B.S. Naik, P.J. Ramulu, R.G. Narayanan, Application of a few necking criteria in predicting the forming limit of unwelded and tailor-welded blanks, J. Strain Anal. Eng. Des. 45 (2009) 79–96. doi:10.1243/03093247JSA562.

[82] R.G. Narayanan, B.S. Naik, Assessing the validity of original and modified failure criteria to predict the forming limit of unwelded and tailor welded blanks with longitudinal weld, Mater. Manuf. Process. 25 (2010) 1351–1358. doi:10.1080/10426914.2010.529588.

[83] R.G. Narayanan, K. Narasimhan, Predicting the forming limit strains of tailor-welded blanks, J. Strain Anal. Eng. Des. 43 (2008) 551–563. doi:10.1243/03093247JSA445.

[84] C. Peister, C. O'Keeffe, J. Imbert, C. Butcher, M. Worswick, S. Malcolm, J. Dykeman, C. Yau, R. Soldaat, W. Bernert, Dynamic and Quasi-Static Testing and Modeling of Hot Stamped Tailor-Welded Axial Crush Rails, in: 18th Int. Conf. Exp. Mech., 2018. doi:10.3390/ICEM18-05401.

[85] C. Peister, Axial Crush Performance of Hot Stamped Tailor Welded Blanks, M.Sc. thesis, University of Waterloo, 2019.

[86] M. Tummers, Development of a Tailor-Welded Hot Stamped Side Frame Member, M.Sc. thesis, University of Waterloo, 2019.

[87] M. Basaran, Stress State Dependent Damage Modeling with a Focus on the Lode Angel Influence, Ph.D. thesis, RWTH Aachen University, 2011.

[88] K. Omer, A. Bardelcik, R. George, D. Detwiler, N. Adam, M. Worswick, Development and Testing of a Hot Stamped Axial Crush Member with Tailored Properties, in: Int. Deep Draw. Res. Gr., 2014: pp. 321–326.

[89] L. ten Kortenaar, Failure Characterization of Hot Formed Boron Steels with Tailored Mechanical Properties, M.Sc. thesis, University of Waterloo, 2016.

[90] A.S. Khan, S. Huang, Continuum Theory of Plasticity, John Wiley & Sons, Inc., 1995.

[91] R. von Mises, Mechanik der festen Körper im plastisch- deformablen Zustand, Göttin. Nachr. Math. Phys. 1 (1913) 582–592.

[92] F. Barlat, J.C. Brem, J.W. Yoon, K. Chung, R.E. Dick, D.J. Lege, F. Pourboghrat, S.-H. Choi, E. Chu, Plane stress yield function for aluminum alloy sheets — part 1 : theory, Int. J. Plast. 19 (2003) 1297–1319. doi:10.1016/S0749-6419(02)00019-0.

[93] H.J. Bohm, A short introduction to basic aspects of continuum micromechanics, Vienna, 2016.

[94] C. Yan, On Homogenization and De-Homogenization of Composite Materials, Ph.D. thesis, Drexel University, 2003.

[95] S. Li, G. Wang, Introduction to Micromechanics and Nanomechanics, © World Scientific Publishing Co. Pte. Ltd., 2008. doi:https://doi.org/10.1142/6834.

[96] H. Moussaddy, A New Definition of the Representative Volumen Element in Numerical Homogenization Problems and its Application to the Performance Evaluation of Analytical Homogenization Models, Ph.D. thesis, Université de Montréal, 2013. http://publications.polymtl.ca/1091/1/2013_HadiMoussaddy.pdf.

[97] A. Zaoui, Continuum micromechanics: Survey, J. Eng. Mech. 128 (2002) 808–816. doi:10.1061/(ASCE)0733-9399(2002)128:8(808).

[98] W. Voigt, Über die Beziehung zwischen den beiden Elastizitätskonstanten isotroper Körper, Wied. Ann. Phys. 38 (1889) 573–587. doi:https://doi.org/10.1002/andp.18892741206.

[99] A. Reuss, Berechnung der Fliessgrenze von Mischkristallen auf Grund der Plastizitätsbedingung fürEinkristalle, Math. Mech. 9 (1929) 49–58. doi:https://doi.org/10.1002/zamm.19290090104.

[100] J.D. Eshelby, The Determination of the Elastic Field of an Ellipsoidal Inclusion and related Problems, Proc. Roy. Soc. A 241 (1957) 376–396. doi:https://doi.org/10.1098/rspa.1957.0133.

[101] P. Samadian, C. Butcher, M.J. Worswick, New Mean-Field Homogenization Schemes for the Constitutive Modelling of the Elastic and Elastoplastic Deformation Behavior of Multi-Phase Materials, Mater. Today Commun. 24 (2020) 1–13. doi:10.1016/j.mtcomm.2019.100707.

[102] E. Kröner, Berechnung der elastischen Konstanten des Vielkristalls aus den Konstanten des Einkristalls, Z. Phys. 151 (1958) 504–518. doi:https://doi.org/10.1007/BF01337948.

[103] A. V. Hershey, The elasticity of an isotropic aggregate of anisotropic cubic crystals, J. Appl. Mech. 21 (1954) 236–241.

[104] T. Mori, K. Tanaka, Average Stress in Matrix and Average Elastic Energy of Materials with Misfitting Inclusions, Acta Met. 21 (1973) 571–574. doi:https://doi.org/10.1016/0001-6160(73)90064-3.

[105] M. Hori, S. Nemat-Nasser, Double-inclusion model and overall moduli of multi-phase composites, Mech. Mater. 14 (3) (1993) 189–206.

[106] P.P. Castañeda, J.R. Willis, The effect of spatial distribution on the effective behavior of composite materials and cracked media, J. Mech. Phys. Solids. 43 (1995) 1919–1951. doi:10.1016/0022-5096(95)00058-Q.

[107] G. Lielens, P. Pirotte, A. Couniot, F. Dupret, R. Keunings, Prediction of thermo-mechanical properties for compression moulded composites, Compos. Part A Appl. Sci. Manuf. 29 (1998) 63–70. doi:10.1016/S1359-835X(97)00039-0.

[108] E.S. Perdahcıoğlu, H.J.M. Geijselaers, Constitutive modeling of two phase materials using

the mean field method for homogenization, Int. J. Mater. Form. 4 (2011) 93–102. doi:10.1007/s12289-010-1007-6.

[109] L. Wua, I. Doghri, L. Noels, An incremental-secant mean-field homogenisation method with second statistical moments for elasto-plastic composite materials, Philos. Mag. (2015) 1–36. doi:10.1080/14786435.20xx.xxxxxx.

[110] A. Abedini, Z.T. Chen, A micromechanical model of particle-reinforced metal matrix composites considering particle size and damage, Comput. Mater. Sci. 85 (2014) 200–205. doi:10.1016/j.commatsci.2014.01.012.

[111] G.J. Weng, The overall elastoplastic stress-strain relations of dual-phase metals, J. Mech. Phys. Solids. 38 (1990) 419–441. doi:10.1016/0022-5096(90)90007-Q.

[112] R. Hill, A self-consistent mechanics of composite materials, J. Mech. Phys. Solids. 13 (1965) 213–222. doi:10.1016/0022-5096(65)90010-4.

[113] O. Pierard, Micromechanics of inclusion-reinforced composite in elasto-plasticity and elasto-viscoplasticity: modeling and computation, Universit´e Catholique de Louvain, 2006.

[114] R. Hill, Continuum Micro-Mechanics of Elastoplastic Polycrystals, J. Mech. Phys. Solids. 13 (1965) 89–101.

[115] O. Pierard, I. Doghri, Study of Various Estimates of the Macroscopic Tangent Operator in the Incremental Homogenization of Elastoplastic Composites, Int. J. Multiscale Comput. Eng. 4 (2006) 521–543. doi:10.1615/IntJMultCompEng.v4.i4.80.

[116] L. Wu, L. Noels, L. Adam, I. Doghri, A combined incremental-secant mean-field homogenization scheme with per-phase residual strains for elasto-plastic composites, Int. J. Plast. 51 (2013) 80–102. doi:10.1016/j.ijplas.2013.06.006.

[117] P. Ponte Castaneda, Exact second-order estimates for the effective mechanical properties of nonlinear composite materials, J. Mech. Phys. Solids. 44 (6) (1996) 827–862.

[118] M. Bornert, T. Bretheau, P. Gilormini, Homogénéisation en mécanique des matériaux, Tome 1: Matériaux aléatoires élastiques et milieux périodiques, Hermès Science Publications, Paris, 2000.

[119] I. Doghri, A. Ouaar, Homogenization of two-phase elasto-plastic composite materials and structures study of tangent operators, cyclic plasticity and numerical algorithms, Int. J. Solids Struct. 40 (2003) 1681–1712. doi:10.1016/S0020-7683(03)00013-1.

[120] P. Suquet, Overall Properties of Nonlinear Composites, in: A. Pineau, A. Zaoui (Eds.), Proc. IUTAM Symp., Kluwer Academic Publishers, Paris. France, 1995.

[121] I. Doghri, L. Brassart, L. Adam, J.S. Gérard, A second-moment incremental formulation for the mean-field homogenization of elasto-plastic composites, Int. J. Plast. 27 (2011) 352–371. doi:10.1016/j.ijplas.2010.06.004.

[122] B. Klusemann, B. Svendsen, Homogenization methods for multi-phase elastic composites: Comparisons and benchmarks, Tech. Mech. 30 (2010) 374–386.

[123] P.A. Hessman, K. Hornberger, A comparison of mean field homogenization schemes for short fiber reinforced thermoplastics, Proc. Appl. Math. Mech. 17 (2017) 595–596. doi:10.1002/pamm.201710267.

[124] I. Doghri, L. Brassart, L. Adam, J.S. Gérard, A second-moment incremental formulation for the mean-field homogenization of elasto-plastic composites, Int. J. Plast. 27 (2011) 352–371. doi:10.1016/j.ijplas.2010.06.004.

[125] Q. Lai, L. Brassart, O. Bouaziz, M. Goun, M. Verdier, G. Parry, A. Perlade, Y. Br, T. Pardoen, Influence of martensite volume fraction and hardness on the plastic behavior of dual-phase steels : Experiments and micromechanical modeling, (2015) 1–17. doi:10.1016/j.ijplas.2015.09.006.

[126] A. Ebrahimian, S.S.G. Banadkouki, Mutual mechanical effects of ferrite and martensite in a low alloy ferrite- martensite dual phase steel Mutual mechanical effects of ferrite and martensite in a low alloy ferrite-martensite dual phase steel, J. Alloys Compd. 708 (2017) 43–54. doi:10.1016/j.jallcom.2017.02.287.

[127] G.E. Dieter, Mechanical Metallurgy, McGraw-Hill book company, 1961.

[128] A. Ramazani, K. Mukherjee, H. Quade, U. Prahl, W. Bleck, Correlation between 2D and 3D flow curve modelling of DP steels using a microstructure-based RVE approach, Mater. Sci. Eng. A. 560 (2013) 129–139. doi:10.1016/j.msea.2012.09.046.

[129] A.P. Pierman, O. Bouaziz, T. Pardoen, P.J. Jacques, L. Brassart, The influence of microstructure and composition on the plastic behaviour of dual-phase steels, Acta Mater. 73 (2014) 298–311. doi:10.1016/j.actamat.2014.04.015.

[130] S. Sodjit, V. Uthaisangsuk, A Micromechanical Flow Curve Model for Dual Phase Steels, J. Met. Mater. Miner. 22 (2012) 87–97.

[131] S. Sodjit, V. Uthaisangsuk, Microstructure based prediction of strain hardening behavior of dual phase steels, Mater. Des. 41 (2012) 370–379. doi:10.1016/j.matdes.2012.05.010.

[132] R. Rodriguez, I. Gutierrez, Unified Formulation to Predict the Tensile Curves of Steels with Different Microstructures, Mater. Sci. Forum. 426–432 (2003) 4525–4530. doi:10.4028/www.scientific.net/MSF.426-432.4525.

[133] A. Ramazani, P.T. Pinard, S. Richter, A. Schwedt, U. Prahl, Characterisation of microstructure and modelling of flow behaviour of bainite-aided dual-phase steel, Comput. Mater. Sci. 80 (2013) 134–141. doi:10.1016/j.commatsci.2013.05.017.

[134] A. Ramazani, Y. Chang, U. Prahl, Characterization and modeling of failure initiation in bainite-aided DP steel, Adv. Eng. Mater. 16 (2014) 1370–1380. doi:10.1002/adem.201300556.

[135] P. Srithananan, P. Kaewtatip, V. Uthaisangsuk, Micromechanics-based modeling of stress-strain and fracture behavior of heat-treated boron steels for hot stamping process, Mater. Sci. Eng. A. 667 (2016) 61–76. doi:10.1016/j.msea.2016.04.065.

[136] M. Delincé, Y. Bréchet, J.D. Embury, M.G.D. Geers, P.J. Jacques, T. Pardoen, Structure-property optimization of ultrafine-grained dual-phase steels using a microstructure-based strain hardening model, Acta Mater. 55 (2007) 2337–2350.

doi:10.1016/j.actamat.2006.11.029.

[137] A. Pineau, A.A. Benzerga, T. Pardoen, Failure of metals I: Brittle and ductile fracture, Acta Mater. 107 (2016) 424–483. doi:10.1016/j.actamat.2015.12.034.

[138] Z. Chen, C. Butcher, Micromechanics Modelling of Ductile Fracture, Springer, 2013. doi:10.1007/978-94-007-6098-1.

[139] J. Gurland and J. Plateau, The Mechanism of Ductile Rupture of Metals Containing Inclusions, Trans. ASME. 56 (1963) 442–454.

[140] A.S. Argon, J. IM, R. Safoglu, Cavity Formation from Inclusions in Ductile Fracture, Metall. Trans. A. 6A (1975) 825–837.

[141] A.L. Gurson, Continuum Theory of Ductile Rupture by Void Nucleation and Growth: Part I—Yield Criteria and Flow Rules for Porous Ductile Media, J. Eng. Mater. Technol. 99 (1977) 2. doi:10.1115/1.3443401.

[142] C. C. Chu and A. Needleman, Void Nucleation Effects in Biaxially Stretched Sheets, J. Eng. Mater. Technol. 102 (1980) 249–256.

[143] A.S. Argon, J. Im, Separation of Second Phase Particles in Spheroidized 1045 Steel, Cu-0.6pct Cr Alloy, and Maraging Steel in Plastic Straining, Metall. Trans. A. 6A (1975) 839–851.

[144] A.S. Argon, J. Im, A. Needleman, Distribution of plastic strain and negative pressure in necked steel and copper bars, Metall. Trans. A. 6 (1975) 815–824. doi:10.1007/BF02672305.

[145] L. M. Brown and W. M. Stobbs, Work-Hardening of Copper-Silica-5. Equilibrium Plastic Relaxation by Secondary Dislocations, Philos. Mag. 34 (1976) 351–372.

[146] F.M. Beremin, Cavity formation from inclusions in ductile fracture of A508 Steel, Metall. Trans. A. 12A (1981) 723–731. doi:10.1007/BF02672306.

[147] A. Needleman, A continuum model for void nucleation by inclusion debonding, J. Appl.

Mech. 54 (3) (1987) 525–531.

[148] F. McClintock, A Criterion for Ductile Fracture by the Growth of Holes, J. Appl. Mech. 35 (1968) 363–371. doi:10.1115/1.3601204.

[149] A.R. Ragab, A model for ductile fracture based on internal necking of spheroidal voids, Acta Mater. 52 (2004) 3997–4009. doi:10.1016/j.actamat.2004.05.015.

[150] J. R. Rice and D. M. Tracey, On the Ductile Enlargement of Voids in Triaxial Stress Fields, J. Mech. Phys. Solids. 17 (1969) 201–217. doi:https://doi.org/10.1016/0022-5096(69)90033-7.

[151] Y. Huang, Accurate Dilatation Rates for Spherical Voids in Triaxial Stress Fields, 58 (1991) 1084–1086.

[152] B. Liu, X. Qiu, Y. Huang, K.C. Hwang, M. Li, C. Liu, The size effect on void growth in ductile materials, J. Mech. Phys. Solids. 51 (2003) 1171–1187. doi:10.1016/S0022-5096(03)00037-1.

[153] V. Tvergaard and A. Needleman, Analysis of the Cup-Cone Fracture in a Round Tensile Test Bar, Acta Metall. 32 (1984) 157–169.

[154] P. Thomason, Three-Dimensional Models for the Plastic Limit-Loads at Incipient Failure of the Intervoid Matrix in Ductile Porous Solids, Acta Metall. 33 (1985) 1079–1085.

[155] Z.L. Zhang, C. Thaulow, J. Ødegård, Complete Gurson model approach for ductile fracture, Eng. Fract. Mech. 67 (2000) 155–168. doi:10.1016/S0013-7944(00)00055-2.

[156] V. Tvergaard, Influence of voids on shear band instabilities under plane strain conditions, Int. J. Fract. 17 (1981) 389–407.

[157] J.D. M. Gologanu, J. Leblond, Approximate Models for Ductile Metals Containing Non-Spherical Voids – Case of Axisymmetric Prolate Ellipsoidal Cavities, J. Mech. Phys. Solids. (1993) 1723-1754.

[158] M. Brünig, S. Gerke, V. Hagenbrock, Micro-mechanical studies on the effect of the stress

triaxiality and the Lode parameter on ductile damage, Int. J. Plast. 50 (2013) 49–65. doi:10.1016/j.ijplas.2013.03.012.

[159] T.S. Cao, E. Maire, C. Verdu, C. Bobadilla, P. Lasne, P. Montmitonnet, P.O. Bouchard, Characterization of ductile damage for a high carbon steel using 3D X-ray micro-tomography and mechanical tests - Application to the identification of a shear modified GTN model, Comput. Mater. Sci. 84 (2014) 175–187. doi:10.1016/j.commatsci.2013.12.006.

[160] Y. Bao, Prediction of Ductile Crack Formation in Uncracked Bodies, Ph.D. thesis, Massachusetts Institute of Technology, 2003.

[161] L. Kachanov, Rupture Time Under Creep Conditions, Int. J. Fract. 97 (1999) 11–18. doi:10.1023/A:1018671022008.

[162] T.S. Cao, C. Bobadilla, P. Montmitonnet, P.-O. Bouchard, On the development of phenomenological damage models – Application to wire drawing and rolling processes, Key Eng. Mater. Vols. 554–557 (2013) 213–226. doi:10.4028/www.scientific.net/KEM.554-557.213.

[163] N. Allahverdizadeh, A. Manes, M. Giglio, Identification of damage parameters for Ti-6Al-4V titanium alloy using continuum damage mechanics, Materwiss. Werksttech. 43 (2012) 435–440. doi:10.1002/mawe.201200978.

[164] J. Lemaitre, A Continuous Damage Mechanics Model for Ductile Fracture, J. Eng. Mater. Technol. 107 (1985) 83–89. doi:10.1115/1.3225775.

[165] W. Tie-jun, Unified CDM Model and Local Criterion for Ductile fracture-I. Unified CDM Model for Ductile Fracture, Eng. Fract. Mech. 42 (1992) 185–193.

[166] N. Bonora, A Nonlinear CDM Model for Ductile Failure, Eng. Fract. Mech. 58 (1997) 11–28.

[167] S. Dhar, P.M. Dixit, R. Sethuraman, A continuum damage mechanics model for ductile fracture, Int. J. Press. Vessel. Pip. 77 (2000) 335–344. doi:10.1016/S0308-0161(00)00019-

3.

[168] M.G. Cockcroft, D.J. Latham, Ductility and the workability of Metals, J. Inst. Met. 96 (1968) 33–39.

[169] S.I. Oh, C.C. Chen, S. Kobayashi, Ductile Fracture in Axisymmetric Extrusion and Drawing-Part2: Workability in Extrusoin and Drawing, J. Eng. Ind. 101 (1979) 36–44. doi:10.1115/1.3439471.

[170] S.E. Clift, P. Hartley, C.E.N. Sturgess, G.W. Rowe, Fracture prediction in plastic deformation processes, Int. J. Mech. Sci. 32 (1990) 1–17. doi:10.1016/0020-7403(90)90148-C.

[171] D.M. Norris, J.E. Reaugh, B. Moran, D.F. Quinones, A Plastic-Strain, Mean-Stress Criterion for Ductile Fracture, J. Eng. Mater. Technol. 100 (1978) 279–286. doi:10.1115/1.3443491.

[172] M. Oyane, T. Sato, K. Okimoto, S. Shima, Criteria for ductile fracture and their applications, J. Mech. Work. Technol. 4 (1980) 65–81. doi:10.1016/0378-3804(80)90006-6.

[173] L. Xue, Damage accumulation and fracture initiation in uncracked ductile solids subject to triaxial loading, Int. J. Solids Struct. 44 (2007) 5163–5181. doi:10.1016/j.ijsolstr.2006.12.026.

[174] G.R. Johnson, W.H. Cook, Fracture characteristics of three metals subjected to various strains, strain rates, temperatures and pressures, Eng. Fract. Mech. 21 (1985) 31–48. doi:10.1016/0013-7944(85)90052-9.

[175] S.S. Manson, Behavior Of Materials Under Conditions Of Thermal Stress, Cleveland, Ohio, 1954.

[176] L. F. Jr. Coffin, A study of the effects of cyclic thermal stresses on a ductile metal, 1954.

[177] F. Neukamm, M. Feucht, A. Haufe, D. Ag, Considering damage history in crashworthiness simulations, in: 7th Eur. LS-DYNA Conf., Salzburg, Austria, 2009.

[178] M.L. Wilkins, R.D. Streit, J.E. Reaugh, Cumulative-Strain-Damage model of ductile fracture: Simulation and prediction of engineering fracture tests, Lawrence Livermore Natl. Lab. (1980) 1–68. doi:https://doi.org/10.2172/6628920.

[179] T. Wierzbicki, L. Xue, On the effect of the third invariant of the stress deviator on ductile fracture, Cambridge, MA, 2005.

[180] Y. Bai, T. Wierzbicki, A new model of metal plasticity and fracture with pressure and Lode dependence, Int. J. Plast. 24 (2008) 1071–1096. doi:10.1016/j.ijplas.2007.09.004.

[181] H. Tresca, Memoire sur l'ecoulement des corps solids soumis a de fortes pressions, Comptes Rendus l Acad. Des Sci. 59 (1864) 754–758.

[182] C. Coulomb, Essai sur une application des regles des maximis et minimis a quelues problemes de statique relatifs al'architecture, Mem Acad Roy Des Sci. (1776).

[183] O. Mohr, Welche umst¨ ande bedingen elastizit¨ atsgrenze und den bruch eines materials?, Zietschrift Des Vereines Dtsch. Ingenieure. 44 (1900) 1524–1530/1572–1577.

[184] Y. Bai, T. Wierzbicki, A comparative study of three groups of ductile fracture loci in the 3D space, Eng. Fract. Mech. 135 (2015) 147–167. doi:10.1016/j.engfracmech.2014.12.023.

[185] D. Mohr, S.J. Marcadet, Micromechanically-motivated phenomenological Hosford-Coulomb model for predicting ductile fracture initiation at low stress triaxialities, Int. J. Solids Struct. 67–68 (2015) 40–55. doi:10.1016/j.ijsolstr.2015.02.024.

[186] A.S. Khan, H. Liu, A new approach for ductile fracture prediction on Al 2024-T351 alloy, Int. J. Plast. 35 (2012) 1–12. doi:10.1016/j.ijplas.2012.01.003.

[187] T.B. Stoughton, J.W. Yoon, A new approach for failure criterion for sheet metals, Int. J. Plast. 27 (2011) 440–459. doi:10.1016/j.ijplas.2010.07.004.

[188] Y. Bai, T. Wierzbicki, Application of extended Mohr-Coulomb criterion to ductile fracture, Int. J. Fract. 161 (2010) 1–20. doi:10.1007/s10704-009-9422-8.

[189] E. Voce, The relationship between stress and strain for homogeneous deformation, J. Inst.

Met. 74 (1948) 537–562.

[190] H.W. Swift, Plastic instability under plane stress, J. Mech. Phys. Solids. 1 (1952) 1–18. doi:10.1016/0022-5096(52)90002-1.

[191] Y. Jia, Y. Bai, Ductile fracture prediction for metal sheets using all-strain-based anisotropic eMMC model, Int. J. Mech. Sci. 115–116 (2016) 516–531. doi:10.1016/j.ijmecsci.2016.07.022.

[192] R. Östlund, S. Golling, M. Oldenburg, Microstructure based modeling of ductile fracture initiation in press-hardened sheet metal structures, Comput. Methods Appl. Mech. Eng. 302 (2016) 90–108. doi:10.1016/j.cma.2015.11.035.

[193] T.S. Cao, C. Bobadilla, P. Montmitonnet, P.O. Bouchard, A comparative study of three ductile damage approaches for fracture prediction in cold forming processes, J. Mater. Process. Technol. 216 (2015) 385–404. doi:10.1016/j.jmatprotec.2014.10.009.

[194] K. Omer, V-Bend Fracture Strains of 1.2-mm-Thick As-Quenched Usibor® 1500-AS Sheet, Personal Communication, (2019).

[195] ASTM E562 - 11: Standard Test Method for Determining Volume Fraction by Systematic Manual Point Count, ASTM Int. (2011) 1–7. doi:10.1520/E0562-11.

[196] R.D. Sulamet-ariobimo, J. Wahyuadi, T. Sukarnoto, A. Rustandi, Y. Mujalis, D. Prayitno, Tensile properties analysis of AA1100 aluminium and SS400 steel using different JIS tensile standard specimen, Rev. Mex. Trastor. Aliment. 14 (2016) 148–153. doi:10.1016/j.jart.2016.03.006.

[197] T. Rahmaan, A. Abedini, C. Butcher, N. Pathak, M.J. Worswick, Investigation into the shear stress, localization and fracture behaviour of DP600 and AA5182-O sheet metal alloys under elevated strain rates, Int. J. Impact Eng. 108 (2017) 303–321. doi:10.1016/j.ijimpeng.2017.04.006.

[198] M. Gorji, B. Berisha, P. Hora, F. Barlat, Modeling of localization and fracture phenomena in strain and stress space for sheet metal forming, Int. J. Mater. Form. 9 (2016) 573–584.

doi:10.1007/s12289-015-1242-y.

[199] K. Cheong, K. Omer, C. Butcher, R. George, J. Dykeman, Evaluation of the VDA 238-100 Tight Radius Bending Test using Digital Image Correlation Strain Measurement, in: IOP Conf. Ser. J. Phys., 2017. doi:10.1088/1742-6596/896/1/012075.

[200] VDA 238-100: Plate Bending Test for Metallic Materials, (2010) 1–13.

[201] L. ten Kortenaar, A. Bardelcik, M. Worswick, D. Detwiler, The Effect of Stress Triaxiality on the Failure Response of Boron Steel Quenched to a Martensitic and Bainitic Material Condition, in: 4th Int. Conf. Hot Sheet Met. Form. High-Performance Steel, Luleå, Sweden, 2013.

[202] C. Butcher, A. Abedini, Shear confusion: Identification of the appropriate equivalent strain in simple shear using the logarithmic strain measure, Int. J. Mech. Sci. 134 (2017) 273–283. doi:10.1016/j.ijmecsci.2017.10.005.

[203] J. Noder, C. Butcher, A comparative investigation into the influence of the constitutive model on the prediction of in-plane formability for Nakazima and Marciniak tests, Int. J. Mech. Sci. 163 (2019). doi:10.1016/j.ijmecsci.2019.105138.

[204] B. Budiansky, T.T. Wu, Theoretical prediction of plastic strains of polycrystals, in: Proc. 4th V.S. Nat. Congr. Appl. Mech., 1962: pp. 1175–1185.

[205] O. Pierard, C. Friebel, I. Doghri, Mean-field homogenization of multi-phase thermo-elastic composites: A general framework and its validation, Compos. Sci. Technol. 64 (2004) 1587–1603. doi:10.1016/j.compscitech.2003.11.009.

[206] L.P. Kubin, Dislocations, Mesoscale Simulations and Plastic Flow, Oxford University Press, 2013. doi:10.1093/acprof:oso/9780198525011.001.0001.

[207] K.M. Davoudi, J.J. Vlassak, Dislocation evolution during plastic deformation : Equations vs. discrete dislocation dynamics study, J. Appl. Phys. 123 (2018). doi:10.1063/1.5013213.

[208] J.C. Simo, T.J.R. Hughes, Computational Inelasticity, Springer, 1998. doi:10.1007/b98904.

[209] G. Krauss, Deformation and Fracture in Martensitic Carbon Steels Tempered at Low Temperatures, Metall. Mater. Trans. A. 32A (2001) 861–877.

[210] L. Morsdorf, C.C. Tasan, D. Ponge, D. Raabe, 3D structural and atomic-scale analysis of lath martensite: Effect of the transformation sequence, Acta Mater. 95 (2015) 366–377. doi:10.1016/j.actamat.2015.05.023.

[211] G. Krauss, Martensite in steel : strength and structure, Mater. Sci. Eng. A. 273–275 (1999) 40–57.

[212] J.O. Hallquist, LS-DYNA Theory Manual, Livermore Software Technology Corporation, (2006).

[213] C. O'Keeffe, C. Butcher, A Hardness-Mapping User-Defined Material Subroutine for Modelling of Flow and Fracture Behavior of Advanced High-Strength Steels, Personal Communication, (2018).

[214] N. Farabi, D.L. Chen, Y. Zhou, Tensile properties and work hardening behavior of laser-welded dual-phase steel joints, J. Mater. Eng. Perform. 21 (2012) 222–230. doi:10.1007/s11665-011-9865-8.

[215] N. Farabi, D.L. Chen, Y. Zhou, Microstructure and mechanical properties of laser welded dissimilar DP600/DP980 dual-phase steel joints, J. Alloys Compd. 509 (2011) 982–989. doi:10.1016/j.jallcom.2010.08.158.

[216] E. Bayraktar, N. Isac, G. Arnold, An experimental study on the forming parameters of deep-drawable steel sheets in automotive industry, J. Mater. Process. Technol. 162–163 (2005) 471–476. doi:10.1016/j.jmatprotec.2005.02.059.

[217] K. Cheong, C. Butcher, J. Dykeman, The Influence of the Through-Thickness Strain Gradients on the Fracture Characterization of Advanced High-Strength Steels, SAE Int. J. Mater. Manuf. 11 (2018) 541–552. doi:10.4271/2018-01-0627.

Appendix A

P. Samadian, L. ten Kortenaar, K. Omer, C. Butcher, M. J. Worswick, Fracture Characterization of Tailored Usibor® 1500-AS and Damage Modelling Based on a Coupled-Micromechanical-Phenomenological Strategy, *Engineering Fracture Mechanics*, vol. 223, p. 1-20, 2020.

"Accessible through the link below as well as the University of Waterloo's Institutional Repository (UW Space)"

https://www.sciencedirect.com/science/article/pii/S0013794419309646

Appendix B

P. Samadian, C. Butcher, M. J. Worswick, Microstructures and Flow Behavior of Ductibor® 500-AS Steel for a Range of As-Quenched Conditions, *Journal of Materials Engineering and Performance*, vol. 29 (11), p. 7153–7169, 2020.

"Accessible through the link below as well as the University of Waterloo's Institutional Repository (UW Space)"

https://link.springer.com/article/10.1007/s11665-020-05205-x

Appendix C

P. Samadian, C. Butcher, M. J. Worswick**,** A Mean-Field Homogenization Approach to Predict Fracture in As-Quenched Microstructures of Ductibor® 500-AS Steel: Characterization and Modelling, under review for publication in *International Journal of Solids and Structures*, 2020.

Appendix D

P. Samadian, C. O'Keeffe, C. Butcher, M. J. Worswick, Fracture Response in Hot-Stamped Tailor-Welded Blanks of Ductibor® 500-AS and Usibor® 1500-AS: Experiments and Modelling, under review for publication in *Engineering Fracture Mechanics*, 2020.

"Accessible through the University of Waterloo's Institutional Repository (UW Space)"

Appendix E

P. Samadian, C. Butcher, M. J. Worswick, New Mean-Field Homogenization Schemes for the Constitutive Modelling of the Elastic and Elastoplastic Deformation Behavior of Multi-Phase Materials, *Materials Today Communications*, vol. 24, p. 1-13, 2020.

"Accessible through the link below as well as the University of Waterloo's Institutional Repository (UW Space)"

https://www.sciencedirect.com/science/article/pii/S2352492819307111